

Centre for Geo-Information

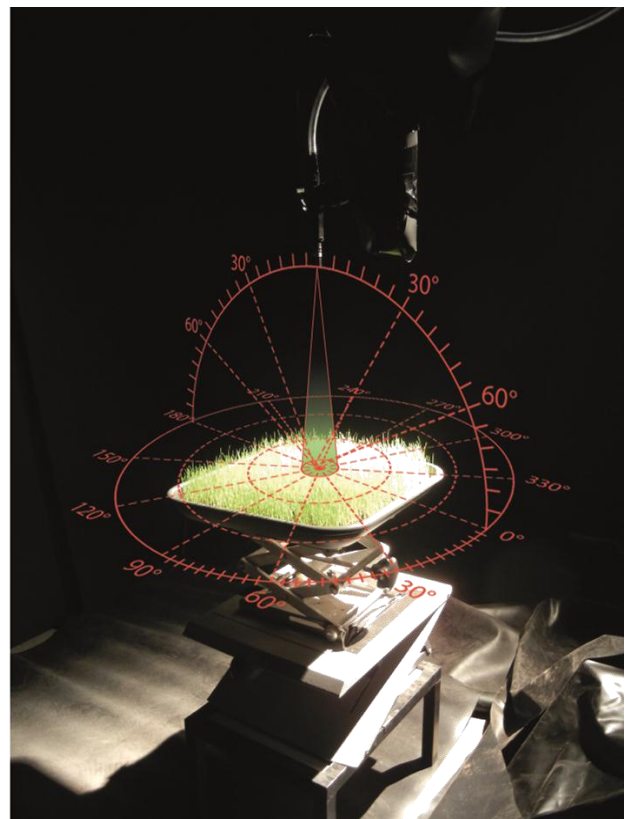
Thesis GIRS-2012-28

---

**Measuring and simulating effects of leaf angle distribution, canopy cover and illumination geometry on the reflectance anisotropy of vegetated surfaces**

Peter Roosjen

December 2012



WAGENINGEN UNIVERSITY  
WAGENINGEN UR





**Measuring and simulating effects of leaf angle distribution, canopy cover and illumination geometry on the reflectance anisotropy of vegetated surfaces**

Peter Roosjen

Registration number 860123 – 707 - 040

Supervisors:

Dr. ir. J.G.P.W. Clevers  
Dr. H.M. Bartholomeus

A thesis submitted in partial fulfilment of the degree of Master of Science  
at Wageningen University and Research Centre,  
The Netherlands

December 2012  
Wageningen, The Netherlands

Thesis code number: GRS-80436  
Thesis Report: GIRS-2012-28  
Wageningen University and Research Centre  
Laboratory of Geo-Information Science and Remote Sensing



# Abstract

Anisotropic reflectance behaviour of natural surfaces affects all remotely sensed imagery and should therefore be included in the interpretation of remote sensing data. Reflectance anisotropy is a wavelength dependent effect and is caused by the illumination and viewing geometry and the characteristics of the observed surface. In this thesis, anisotropic reflectance behaviour of lawn grass and watercress was investigated by comparing multi-angular reflectance measurements, obtained by a laboratory goniometer, to simulations of the soil-leaf-canopy radiative transfer model. The influence of leaf angle distribution, vegetation cover and illumination geometry on the reflectance anisotropy of lawn grass and watercress targets was assessed. Comparable results between the measurements and simulations would indicate the usefulness of the combination of the goniometer facility and the SLC-model for the research of biophysical and biochemical parameters on reflectance anisotropy. Most of the results of the goniometer measurements are in agreement with the physical mechanisms that cause reflectance anisotropy and previously published research on reflectance anisotropy. However, some unexpected results were obtained due to the inhomogeneity and sparse coverage of the vegetation targets. The soil-leaf-canopy model was able to simulate some of the measured anisotropic reflectance effects after normalization of the data; however, the model was not able to accurately reproduce the measured spectral signatures of the lawn grass and watercress targets, as measured in the laboratory. Therefore, the SLC-model cannot be used in combination with the set-up of the laboratory goniometer, as applied for the measurements performed for this thesis, to investigate the influence of biophysical and biochemical parameters on reflectance anisotropy.

**Keywords:** reflectance anisotropy; bidirectional reflectance distribution function; biconical reflectance factor; bidirectional reflectance factor; multi-angular measurements; laboratory goniometer; radiative transfer modelling



# Table of contents

<b>Abstract .....</b>	<b>v</b>
<b>Table of contents .....</b>	<b>vii</b>
<b>List of figures.....</b>	<b>x</b>
<b>List of tables.....</b>	<b>xii</b>
<b>List of abbreviations .....</b>	<b>xiii</b>
<b>1 INTRODUCTION.....</b>	<b>1</b>
1.1 Background.....	2
1.2 Problem definition.....	3
1.3 Goals and research questions .....	6
1.3.1 Research question 1 .....	6
1.3.2 Research question 2 .....	6
1.3.3 Research question 3 .....	7
<b>2 METHODOLOGY.....</b>	<b>9</b>
2.1 The goniometer facility .....	10
2.1.1 ASD FieldSpec 3 Spectroradiometer.....	10
2.1.2 Kawasaki FS10E .....	12
2.1.3 Quartz Tungsten Halogen lamp.....	12
2.1.4 Spectralon.....	12
2.1.5 Laboratory .....	13
2.2 Measurement positions .....	14
2.3 Protocol .....	15
2.3.1 Dark current.....	15
2.3.2 White reference .....	15
2.3.3 Measurements .....	15
2.4 Terminology.....	16
2.4.1 Bidirectional reflectance distribution function .....	16
2.4.2 Bidirectional reflectance factor .....	16
2.4.3 Biconical reflectance factor .....	16
2.5 Targets.....	18
2.5.1 Plot size.....	18
2.5.2 Sowing density.....	19

2.5.3	Soil .....	19
2.5.4	Growing conditions .....	20
2.5.5	Vegetation cover .....	20
2.5.6	Leaf orientation value .....	21
2.5.7	Leaf and canopy dimensions .....	21
2.6	Soil-leaf-canopy model.....	22
2.6.1	SOIL.....	23
2.6.1.1	Hapke b and c .....	23
2.6.1.2	Hapke $B_0$ .....	23
2.6.1.3	Hapke h.....	23
2.6.1.4	SM%.....	23
2.6.1.5	Input spectral signature soil .....	23
2.6.2	LEAF .....	25
2.6.2.1	Chlorophyll content.....	25
2.6.2.2	Water content and Dry matter content .....	26
2.6.2.3	Brown pigment content .....	27
2.6.2.4	Mesophyll structure parameter .....	27
2.6.3	CANOPY .....	28
2.6.3.1	Leaf area index .....	28
2.6.3.2	Leaf inclination distribution function .....	28
2.6.3.3	Hot-spot size parameter.....	28
2.6.3.4	Fraction brown leaf area .....	29
2.6.3.5	Dissociation factor .....	29
2.6.3.6	Vertical crown cover fraction .....	29
2.6.3.7	Tree shape factor.....	29
2.6.4	SLC-model input parameters.....	30
2.7	Pre-processing.....	31
<b>3</b>	<b>RESULTS AND DISCUSSION .....</b>	<b>35</b>
3.1	Laboratory measurements .....	36
3.1.1	Bare soil .....	38
3.1.2	Lawn grass .....	41
3.1.3	Watercress.....	46
3.2	SLC simulations.....	50
3.2.1	Bare soil .....	51

3.2.2	7 Days old lawn grass .....	53
3.2.3	18 Days old lawn grass .....	55
3.2.4	7 Days old watercress.....	57
3.2.5	18 Days old watercress.....	59
3.3	Laboratory Measurements vs. SLC simulations.....	61
3.4	Illumination angle.....	64
3.5	Anisotropy index .....	70
<b>4</b>	<b>DISCUSSION .....</b>	<b>73</b>
4.1	Parameters SLC-model .....	73
4.1.1	Leaf Area Index.....	73
4.1.2	LIDFa and LIDFb .....	76
4.1.3	Water content .....	78
4.2	SLC simulations.....	80
4.3	Laboratory measurements .....	81
<b>5</b>	<b>CONCLUSIONS AND RECOMMENDATIONS .....</b>	<b>83</b>
5.1	Answering the research questions .....	84
5.2	Summary and conclusions .....	86
5.3	Recommendations.....	87
	<b>REFERENCES.....</b>	<b>89</b>

## List of figures

<i>Figure 1. Gap effect on an erectophile canopy.....</i>	<i>2</i>
<i>Figure 2. Shadow effects on bare soil as a result of illumination angle .....</i>	<i>3</i>
<i>Figure 3. Schematic overview of the components of the goniometer facility .....</i>	<i>10</i>
<i>Figure 4. Definition of the sampling interval and the spectral resolution of the spectrometer.....</i>	<i>11</i>
<i>Figure 5. Spectrometers of the ASD.....</i>	<i>11</i>
<i>Figure 6. Kawasaki FS10E robot arm.....</i>	<i>12</i>
<i>Figure 7. The illumination source used in the laboratory set-up .....</i>	<i>12</i>
<i>Figure 8. Darkening the laboratory .....</i>	<i>13</i>
<i>Figure 9. Schematic cross section of the measurement set-up .....</i>	<i>14</i>
<i>Figure 10. Measurement positions from a top-view perspective .....</i>	<i>14</i>
<i>Figure 11. Photographs taken at approximately nadir position.....</i>	<i>18</i>
<i>Figure 12. Relation between the VZA and the observed surface area .....</i>	<i>19</i>
<i>Figure 13. 18 days old watercress .....</i>	<i>20</i>
<i>Figure 14. Relation between single scattering albedo and the soil reflectance .....</i>	<i>24</i>
<i>Figure 15. Positions that were influenced by shadows caused by the robot arm .....</i>	<i>31</i>
<i>Figure 16. Repetitive BCRF measurements taken at nadir position .....</i>	<i>36</i>
<i>Figure 17. BCRFs of bare soil .....</i>	<i>38</i>
<i>Figure 18. BCRFs of bare soil in the principal plane.....</i>	<i>39</i>
<i>Figure 19. Interpolated polar plots of the observed ANIFs of bare soil .....</i>	<i>40</i>
<i>Figure 20. BCRFs of watercress observed in the principal plane .....</i>	<i>41</i>
<i>Figure 21. BCRFs of lawn grass observed over the principal plane .....</i>	<i>42</i>
<i>Figure 22. ANIFs of lawn grass observed over the principal plane .....</i>	<i>42</i>
<i>Figure 23. Interpolated polar plots of the observed ANIFs of 7 days old lawn grass .....</i>	<i>43</i>
<i>Figure 24. Interpolated polar plots of the observed ANIFs of 18 days old lawn grass .....</i>	<i>45</i>
<i>Figure 25. BCRFs of watercress observed in the principal plane .....</i>	<i>46</i>
<i>Figure 26. BCRFs of watercress observed in the principal plane .....</i>	<i>47</i>
<i>Figure 27. ANIFs of watercress observed in the principal plane.....</i>	<i>47</i>
<i>Figure 28. Interpolated polar plots of the observed ANIFs of 7 days old watercress .....</i>	<i>48</i>
<i>Figure 29. Interpolated polar plots of the observed ANIFs of 18 days old watercress .....</i>	<i>49</i>
<i>Figure 30. Simulated (black) and measured (red) reflectance of bare soil.....</i>	<i>51</i>
<i>Figure 31. Simulated BRFs and ANIFs of bare soil over the principal plane .....</i>	<i>51</i>
<i>Figure 32. Interpolated polar plots of the ANIFs of bare soil.....</i>	<i>52</i>
<i>Figure 33. Simulated (black) and measured (red) reflectance of 7 days old lawn grass .....</i>	<i>53</i>
<i>Figure 34. Simulated BRFs and ANIFs of 7 days old lawn grass over the principal plane .....</i>	<i>53</i>
<i>Figure 35. Interpolated polar plots of the ANIFs of 7 days old lawn grass.....</i>	<i>54</i>
<i>Figure 36. Simulated (black) and measured (red) reflectance of 18 days old lawn grass.....</i>	<i>55</i>

<i>Figure 37. Simulated BRFs and ANIFs of 18 days old lawn grass over the principal plane .....</i>	<i>55</i>
<i>Figure 38. Interpolated polar plots of the ANIFs of 18 days old lawn grass.....</i>	<i>56</i>
<i>Figure 39. Simulated (black) and measured (red) reflectance of 7 days old watercress.....</i>	<i>57</i>
<i>Figure 40. Simulated BRFs and ANIFs of 7 days old watercress over the principal plane .....</i>	<i>57</i>
<i>Figure 41. Interpolated polar plots of the ANIFs of 7 days old watercress .....</i>	<i>58</i>
<i>Figure 42. Simulated (black) and measured (red) reflectance of 18 days old watercress.....</i>	<i>59</i>
<i>Figure 43. Simulated BRFs and ANIFs of 18 days old watercress over the principal plane .....</i>	<i>59</i>
<i>Figure 44. Interpolated polar plots of the ANIFs of 18 days old watercress .....</i>	<i>60</i>
<i>Figure 45. RMSE (%) between the measured and simulated reflectance.....</i>	<i>61</i>
<i>Figure 46. Measured and simulated ANIFs over the principal plane of bare soil.....</i>	<i>62</i>
<i>Figure 47. Measured and simulated ANIFs over the principal plane of lawn grass .....</i>	<i>62</i>
<i>Figure 48. Measured and simulated ANIFs over the principal plane of watercress .....</i>	<i>63</i>
<i>Figure 49. Interpolated polar plots of the ANIFs of bare soil as measured in the laboratory and simulated by the SLC-model .....</i>	<i>65</i>
<i>Figure 50. Interpolated polar plots of the ANIFs of 7 days old lawn grass as measured in the laboratory and simulated by the SLC-model .....</i>	<i>66</i>
<i>Figure 51. Interpolated polar plots of the ANIFs of 18 days old lawn grass as measured in the laboratory and simulated by the SLC-model .....</i>	<i>67</i>
<i>Figure 52. Interpolated polar plots of the ANIFs of 7 days old watercress as measured in the laboratory and simulated by the SLC-model .....</i>	<i>68</i>
<i>Figure 53. Interpolated polar plots of the ANIFs of 18 days old watercress as measured in the laboratory and simulated by the SLC-model .....</i>	<i>69</i>
<i>Figure 54. Anisotropy indices (ANIX) of the measured and simulated bare soil .....</i>	<i>70</i>
<i>Figure 55. Anisotropy indices (ANIX) of the measured and simulated lawn grass and watercress .....</i>	<i>71</i>
<i>Figure 56. SLC simulations with different LAI values for lawn grass .....</i>	<i>74</i>
<i>Figure 57. SLC simulations with different LAI values for watercress .....</i>	<i>74</i>
<i>Figure 58. Changes in RMSE of lawn grass and watercress between measured and simulated reflectance after increasing the LAI parameter.....</i>	<i>75</i>
<i>Figure 59. SLC simulations with different LIDFa and LIDFb values for lawn grass .....</i>	<i>76</i>
<i>Figure 60. SLC simulations with different LIDFa and LIDFb values for watercress .....</i>	<i>77</i>
<i>Figure 61. Changes in RMSE of lawn grass and watercress between measured and simulated reflectance after changing the LIDFa and LIDFb parameters.....</i>	<i>77</i>
<i>Figure 62. SLC simulations with different Cw and Cdm values for lawn grass .....</i>	<i>78</i>
<i>Figure 63. SLC simulations with different Cw and Cdm values for watercress.....</i>	<i>79</i>
<i>Figure 64. Changes in RMSE of lawn grass and watercress between measured and simulated reflectance after changing the dry matter to water content ratio .....</i>	<i>79</i>

## List of tables

<i>Table 1. The Sampling interval and spectral resolution of the spectrometer .....</i>	<i>10</i>
<i>Table 2. Overview of the properties of the lawn grass and old watercress targets .....</i>	<i>21</i>
<i>Table 3. Overview of the input parameters of the SLC-model and their units .....</i>	<i>22</i>
<i>Table 4. Chlorophyll content.....</i>	<i>26</i>
<i>Table 5. Water content and dry matter content .....</i>	<i>27</i>
<i>Table 6. Leaf area index.....</i>	<i>28</i>
<i>Table 7. Hot-spot size parameter .....</i>	<i>29</i>
<i>Table 8. Tree shape factor .....</i>	<i>30</i>
<i>Table 9. An overview of the input parameters for the SLC-model as used during the simulations.....</i>	<i>30</i>
<i>Table 10. Structure of the dataset for the creation of polar contour plots. ....</i>	<i>33</i>
<i>Table 11. RMS differences between the repetitive measurements at nadir position .....</i>	<i>37</i>
<i>Table 12. LAI parameter settings for the repeated SLC simulations. ....</i>	<i>73</i>
<i>Table 13. The water content in g/cm<sup>2</sup> for increasing Cw – Cdm ratios. ....</i>	<i>78</i>

## List of abbreviations

ANIF	Anisotropy factor
ANIX	Anisotropy index
ASD	Analytical Spectral Devices INC.
ASG	Automated Spectro-Goniometer
BCRF	Biconical reflectance factor
BRDF	Bidirectional reflectance distribution function
BRF	Bidirectional reflectance factor
CCRF	Conical-conical reflectance factor
CHRIS	Compact High Resolution Imaging Spectrometer
EGO	European Goniometric Facility
FIGOS	Field Goniometer System
GCP	Ground control point
GIFOV	Ground instantaneous field of view
FOV	Field of view
IFOV	Instantaneous field of view
LAI	Leaf area index
LOV	Leaf orientation value
MISR	Multiangle Imaging Spectro Radiometer
MODIS	Moderate Resolution Imaging Spectroradiometer
NBAR	Nadir BRDF adjusted reflectance
NIR	Near infrared
QTH	Quartz Tungsten Halogen
PROBA	Project for On-Board Autonomy
RMS	Root mean squared
RMSE	Root mean squared error
SLC	Soil-Leaf-Canopy
SWIR	Short wave infrared
VNIR	Visible and near infrared
VZA	View zenith angle



# 1 INTRODUCTION

Natural surfaces exhibit anisotropic reflectance behaviour, which means that the distribution and the intensity of the radiance that is reflected by a surface varies with different illumination and viewing geometries. The mathematical description of reflectance anisotropy is called the bidirectional reflectance distribution function (BRDF), as defined by Nicodemus et al. (1977). Reflectance anisotropy affects all remotely sensed images and therefore, anisotropic reflectance effects need to be included in the interpretation of remote sensing data. The anisotropic reflectance behaviour of surfaces is wavelength dependent and is caused by optical and structural properties of the observed target.

There are two ways of looking at reflectance anisotropy: On the one hand, anisotropic reflectance behaviour can be considered as a source of error, which needs to be corrected for. Reflectance anisotropy can cause brightness gradients in remote sensing data, which influences, for example, land cover classification (Brown De Colstoun and Walthall 2006) or the accuracy of vegetation indices (Verrelst et al. 2008). It is therefore important to normalize remote sensing data, acquired under specific view and illumination geometries, to standard reflectance values. An example of a widely accepted product, transformed to a standard reflectance, is the Moderate resolution Imaging Spectroradiometer (MODIS) nadir BRDF adjusted reflectance (NBAR) product. On the other hand, anisotropic reflectance data contains information about the biophysical and biochemical composition of surface targets that cannot be derived from spectral properties alone (Barnsley et al. 1994). Several studies demonstrated the improved estimation of biophysical and biochemical vegetation parameters with the use of multi-angular reflectance data, like leaf area index (LAI) (Vuolo et al. 2008), foliar water and dry matter content (Schaeppman et al. 2005) and foliar nitrogen concentration (Kneubühler et al. 2008). Heiskanen (2006) demonstrated that using multi-angular multispectral data instead of multispectral nadir or single band multi-angular data alone, reduced the errors in tree cover and tree height estimation. Whether reflectance anisotropy is considered as a source of error or as an additional source of information, accurate knowledge about its magnitude and variability is important either way (Schopfer et al. 2007).

The main goal of this thesis is to investigate the effect of different parameters on the anisotropic reflectance behaviour of several soil and vegetation targets as observed in multi-angular reflectance measurements, performed by the laboratory goniometer facility of Wageningen University (Roosjen et al. 2012) and to compare the results of the measurements to simulations performed by the physically based Soil-Leaf-Canopy (SLC) radiative transfer model (Verhoef and Bach 2007). The combination of the goniometer and the SLC-model could be valuable for the investigation of vegetation parameters on the anisotropic reflectance behaviour of vegetated surfaces.

The structure of the paper is as follows: in the methodology section, the goniometer facility, the SLC-model, the collection of the model parameters and the pre-processing of the data is described. In the results and discussion section, first results and measurements obtained under an illumination angle of 45° will be shown and discussed, followed by a comparison to the measurements under a 30° illumination angle. After this, a section is devoted to a general discussion on the measurements and simulations, followed by a section with conclusions on this thesis and recommendations for future research.

## 1.1 Background

There are three key scattering types that influence reflectance anisotropy: isotropic scattering, volumetric scattering and geometric scattering. Isotropic scattering is assumed to be a constant and has no angular dependence. Volumetric scattering is scattering which takes place inside a medium. Volumetric scattering is angular dependent and is caused by small interleaf gaps inside a canopy. Geometric scattering is caused by shadows and is also angular dependent. Geometric scattering can be explained by two effects (Kimes 1983). These effects are referred to as the gap effect and the backshadow effect, adopting the terminology of Sandmeier et al. (1998a). For dense erectophile canopies (canopies that consist of mainly vertical leaves), the well-illuminated parts of the canopy are located in the upper layer of the canopy, while the less-illuminated parts of the canopy are located in the lower parts of the canopy. The highest probability of a gap and thus the highest probability for the observation of the lower parts of the canopy is at nadir position. As the off-nadir viewing angle increases, the probability of a gap decreases. When only the gap effect is present, increasing the off-nadir viewing angle would result in an increase in the observed proportion of the well-illuminated upper part of the canopy, which in turn results in an increase in reflectance, independent of the azimuth direction. This effect is most pronounced at greater illumination angles, which causes a stronger gradient between the well illuminated upper part of the canopy and the less-illuminated lower part (see *Figure 1*).

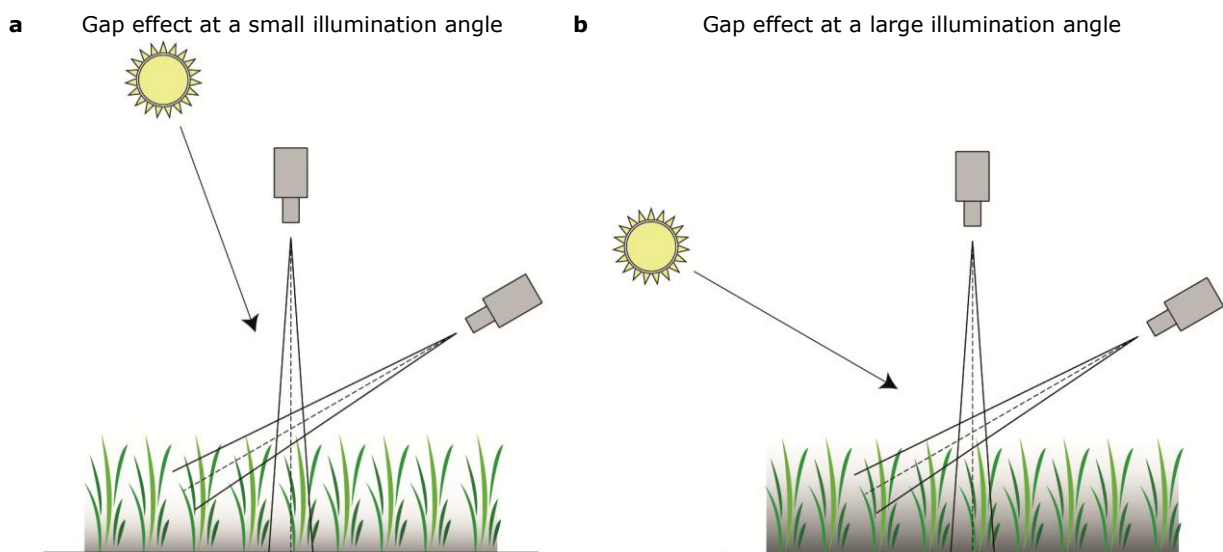


*Figure 1. Gap effect on an erectophile canopy. a) For a small illumination angle; b) For a large illumination angle. The gradient indicates the intensity of the shading. Images based on Kimes (1983). Viewing a canopy in the direction towards the source of illumination allows for the observation of the shadowed parts of a canopy. This is called the backshadow effect. Increasing the off-nadir viewing angle in the forward scatter direction would thereby result in a greater proportion of observed shadowed elements and thus result in a lower observed reflectance. Because leaves are not completely non-transparent, a proportion of the incoming radiance is transmitted, resulting in a reduction of the impact of the backshadow effect. Therefore, at extreme viewing angles, the gap effect dominates the backshadow effect (Sandmeier et al. 1998a). The combination of the lowest reflectance around the nadir position due to the gap effect, and the lowest reflectance in the forward scatter direction due to the backshadow effect, results in a minimum reflectance for dense vegetated canopies close to nadir slightly in the forward direction (Sandmeier et al. 1998a). The maximum*

reflectance is typically found in the backward scatter direction where the observation and illumination angle precisely coincide and is called the hot-spot effect. The gap effect and backshadow effect are less likely to occur at planophile canopies (canopies that consist of mainly horizontal leaves). The top layer of a planophile canopy covers the shadowed, underlying layers, which are therefore not observed. As a result, planophile canopies exhibit stronger isotropic reflectance behaviour and have a less-pronounced hot-spot. In general leaves display specular reflectance behaviour (Grant 1987). Therefore, planophile canopies have a forward scattering component, due to the horizontal orientation of the leaves. The scattering properties of the underlying soil have a strong influence on the reflectance anisotropy of sparsely vegetated surfaces. The anisotropic reflectance behaviour of soils is related to physical properties like soil roughness and soil moisture content, and biochemical properties like organic matter content and mineral content, of which soil roughness has the strongest effect on the reflectance anisotropy (Wang et al. 2012). In general, soils show a strong amount of backscattering and a weaker amount of forward scattering. This is due to the low transmittance of soil particles, which causes a strong contrast in illuminated and shaded parts of the soil in the forward and backward scattering direction, respectively (Jackson et al. 1990; Kimes 1983). Increasing illumination angles results in an increased contrast between illuminated and shadowed parts of the soil and thus in stronger reflectance anisotropic effects (*Figure 2*). Due to the contribution of the underlying soil, sparsely vegetated surfaces display strong backscattering behaviour. This backscattering diminishes as the surface becomes more densely vegetated. At large off-nadir viewing angles, the proportion of observed soil decreases and the observation will therefore look similar to a densely vegetated surface (Kimes 1983).

**a** Soil shadowing at a small illumination angle      **b** Soil shadowing at a large illumination angle

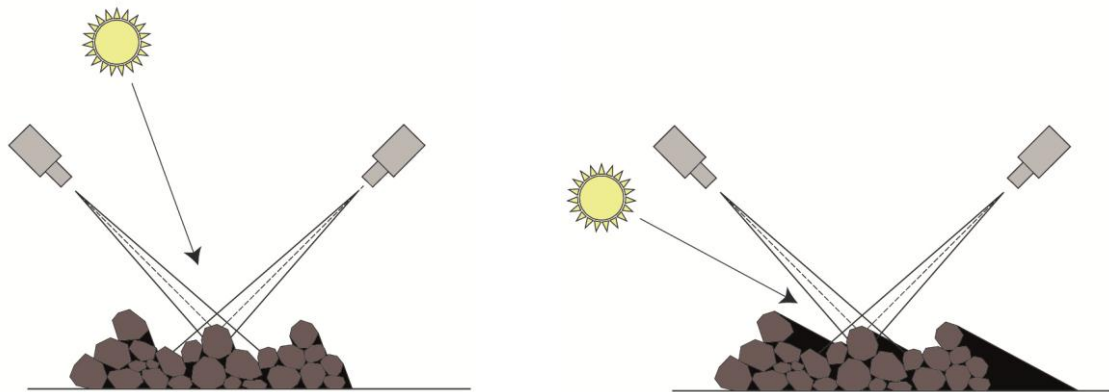


*Figure 2. Shadow effects on bare soil as a result of illumination angle. a) For a small illumination angle; b) For a large illumination angle. Images based on Kimes (1983).*

The proportion of transmittance, absorbance and reflectance is wavelength dependent (Lillesand et al. 2008). In the visible part of the spectrum, especially in the blue and the red part, a relatively large proportion of the incoming radiance is absorbed, and a smaller proportion is transmitted and/or reflected. This results in a strong contrast between shadowed and illuminated parts of a canopy. In the near infrared (NIR), absorbance by leaves is relatively small, which results in multiple scattering inside a canopy. Multiple scattering in the NIR can be considered as volumetric scattering and reduces the contrast between shadowed and illuminated parts of the canopy, resulting in a reduction of anisotropic effects.

## 1.2 Problem definition

All remote sensing data, but especially data acquired at off-nadir viewing angles, or by sensors with a large field of view (FOV) (Beisl 2001), are influenced by reflectance anisotropy. Understanding of the magnitude and variation of reflectance anisotropy effects is essential for the interpretation of remote sensing data. Multi-angular reflectance measurements provide an insight in the anisotropic reflectance behaviour of surface targets. Several satellites are capable of performing multi-angular reflectance measurements, like for example the space-borne Compact High Resolution Imaging Spectrometer (CHRIS) mounted on board the PROject for On-Board Autonomy (PROBA), and the Multi-angle Imaging Spectrometer (MISR) (Diner et al. 1998). The problem that these sensors face is that they are only able to sample a limited number of directions, making it difficult to investigate anisotropic reflectance effects in detail. Goniometers enable the retrieval of a large amount of sampling directions. Field goniometers, like the Field Goniometer System (FIGOS) (Sandmeier and Itten 1999) or the Automated Spectro-Goniometer (ASG) (Painter et al. 2003) are able to observe the anisotropic reflectance behaviour of a specific target from a large number of positions. However, reflectance measurements in the field are influenced by changing illumination conditions due to the movement of the sun (Dangel et al. 2003) or changing atmospheric conditions (Schopfer et al. 2008). Besides this, reflectance measurements performed outside are influenced by diffuse illumination, which complicates investigation of reflectance anisotropy. Multi-angular reflectance measurements performed in a laboratory enable the observation of anisotropic reflectance behaviour under controlled conditions. Advantages of laboratory conditions are the stable illumination conditions, the control over the illumination position and the absence of atmospheric conditions and diffuse irradiance (Sandmeier and Strahler 2000). Wageningen University has built its own laboratory goniometer system for performing multi-angular measurements in order to investigate reflectance anisotropy. The core of the goniometer facility is formed by an industrial robot arm, on which a spectroradiometer is mounted. The robot arm enables fast retrieval of multi-angular reflectance factors with a high repeatability at a theoretically unlimited number of positions in the hemisphere. The results of the goniometer have not been formally assessed and because it has other settings, like the sensor – target distance and field of view. It is important that the results of the measurements will be compared to published results of other goniometer systems, like for example, the results obtained with the European Goniometer Facility (EGO), by Sandmeier et al. (1998a).

Multi-angular measurements can be used for both the exploration of reflectance anisotropy and for the validation of BRDF models (Sandmeier and Strahler 2000). Modelling the BRDF of targets can be done using multi-angular reflectance measurements with empirical or physically based models or through a combination of both (semi-empirical models). Relating multi-angular measurements to BRDF models is interesting for the investigation of the effects of specific parameters on reflectance anisotropy. The problem of (semi) empirical models, like the well-known kernel driven BRDF model proposed by Roujean et al. (1992), is that they do not have a physical basis and therefore do not directly relate to physical parameters (Roberts 2001). Physical radiative transfer models describe the interaction of solar radiation with a target based on physical principals. The parameters of these type of models relate to biophysical and biochemical parameters and can therefore be used for the research of specific parameters on reflectance anisotropy. The SLC-model (Verhoef and Bach 2007) is a physically based radiative transfer model, which is able to simulate directional reflectance spectra of soil and vegetation targets. The SLC-model combines a modified Hapke soil BRDF model (Hapke 1981), a robust version of the PROSPECT leaf model (Jacquemoud and Baret 1990) and a modernized version of the 4SAIL2 canopy radiative transfer model (Verhoef 1984). The SLC-model allows for the

simulation of reflectance anisotropy based on biophysical and biochemical parameters. Laurent et al. (2011a) demonstrated the ability of the SLC-model to simulate near-nadir CHRIS data and they were able to estimate four biophysical and biochemical parameters. Increasing the number of observation directions, results in an increased number of retrievable parameters (Laurent et al. 2011b) and thereby demonstrates the potential of the combination of multi-angular measurements and the SLC-model for the estimation of biophysical and biochemical parameters. It is, however, unknown if the SLC-model can be used in combination with multi-angular reflectance measurements, performed in a laboratory. Ground based measurements, as performed under controlled laboratory conditions allow for the accurate (non-spectral) determination of biophysical and biochemical parameters of the measured targets. These parameters can be used as input parameters for the SLC-model. If simulations by the SLC-model based on these parameters would approximate the multi-angular laboratory measurements, the combination of the SLC-model and the goniometer facility could be valuable for the investigation of effects of vegetation parameters on reflectance anisotropy. The SLC-model could be used for validation of the goniometer measurements and vice versa. This would also indicate that based upon inversion of the SLC-model, meaningful soil and vegetation parameters could be retrieved. Besides this, the SLC-model could be used to simulate measurements close to, or at the hot-spot position, or other positions that cannot be reached by the goniometer.

### **1.3 Goals and research questions**

The main goal of this thesis is to determine if the SLC-model is capable of simulating reflectance anisotropy, as is measured under controlled conditions by the laboratory goniometer facility of Wageningen University. Because it is the first time that measurements will be performed by the goniometer facility, the measurements need to be related to physical mechanisms and compared to published results obtained by other laboratory goniometers. A good comparison between the physical mechanisms, the measured and modelled reflectance would indicate that the goniometer facility and the SLC-model form a solid base for the investigation of anisotropic reflectance effects. Therefore, the influence of several parameters on the reflectance factors, which are measured by the goniometer facility and are simulated by the SLC-model, will be assessed. This results in the following research questions:

#### **1.3.1 Research question 1**

Structural vegetation parameters, like the orientation of leaves inside a canopy, affect reflectance anisotropy. The first goal is to determine what the effect of leaf angle distribution (LAD) is on reflectance anisotropy as measured by the goniometer facility and as simulated by the SLC-model. The first research question is therefore formulated as:

*What is the effect of LAD on the anisotropic reflectance behaviour of vegetation targets as measured under controlled laboratory conditions and is the SLC-model able to simulate these effects?*

The effect of the leaf orientation on the reflectance anisotropy will be measured by performing multi-angular reflectance measurements with the laboratory goniometer facility of lawn grass and watercress targets with different leaf orientations and the results of these measurements will be compared to the results of simulations performed by the SLC-model.

#### **1.3.2 Research question 2**

For sparse canopies, the underlying soil has a strong influence on the anisotropic reflectance behaviour of vegetated surfaces. The second goal is to determine what the effect of the soil background is on the reflectance anisotropy of vegetated surfaces as measured by the goniometer facility and simulated by the SLC-model. The second research question is therefore:

*What is the effect of the soil background on the anisotropic reflectance behaviour of vegetated surfaces as measured under controlled laboratory conditions and is the SLC-model able to simulate these effects?*

This will be assessed by performing multi-angular reflectance measurements with the laboratory goniometer facility of vegetation targets with different proportions of vegetation cover, and comparing the results of these measurements to simulations performed by the SLC-model.

### **1.3.3 Research question 3**

Apart from structural parameters and soil background, the illumination geometry also affects reflectance anisotropy. The third goal is to determine what the influence is of different illumination angles on the reflectance anisotropy of vegetated surfaces as measured by the laboratory goniometer facility and simulated by the SLC-model. Therefore, the third research question is:

*What is the effect of changing the illumination angle on the anisotropic reflectance behaviour of vegetated surfaces as measured under controlled laboratory conditions and is the SLC-model able to simulate these effects?*

This will be determined by comparing the results of the measurements of the laboratory goniometer facility of several vegetation targets, performed at different illumination angles, to simulations of the SLC-model.



## 2 METHODOLOGY

In this section, the laboratory facility to perform the multi-angular reflectance measurements is described, followed by the targets that were measured for this thesis. After this, the collection and the determination of the parameters that were used to simulate reflectance measurements are described. Some of these parameter settings can be considered as results. However, since the emphasis of this thesis is on the measurement and simulation of reflectance anisotropy, they are considered part of the methodology. Finally a section is devoted to the pre-processing of the collected data.

## 2.1 The goniometer facility

In order to perform anisotropic reflectance measurements, Wageningen University has built a laboratory goniometer facility (Roosjen et al. 2012). The core of the goniometer facility is formed by an industrial robot arm, on which a spectroradiometer, and optionally a thermal camera, can be mounted. The set-up is controlled by a Control PC with custom built software. The robot is connected through Ethernet and the spectrometer through Wi-Fi, see *Figure 3*. Information about the measurements, configuration settings, calibration parameters and the measurement results are stored in a directory on the Control PC.

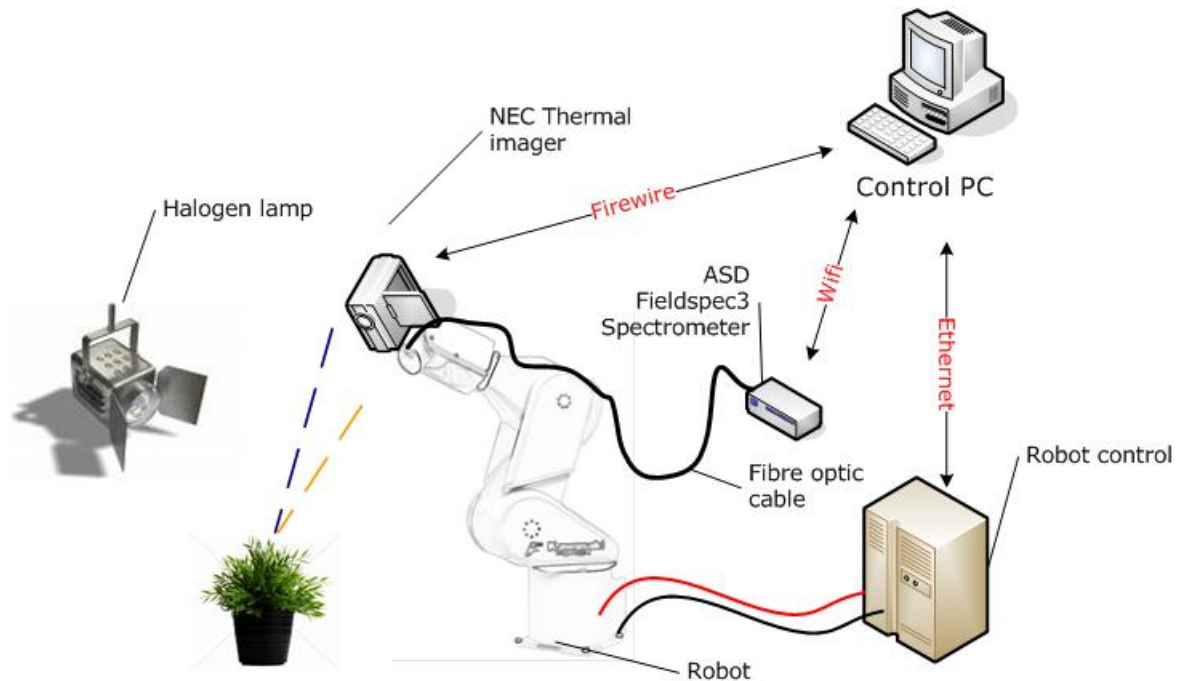


*Figure 3. Schematic overview of the components of the goniometer facility and their connection to the Control PC. Source image: Roosjen et al. (2012).*

### 2.1.1 ASD FieldSpec 3 Spectroradiometer

The following section is based upon the ASD technical guide by Hatchell (1999). The spectral reflectance measurements are performed using an ASD FieldSpec 3 Spectroradiometer (Analytical Spectral Devices, Boulder, CO, USA). From here on, the ASD spectroradiometer will be referred to as spectrometer. The spectrometer has a spectral range of 350 – 2500 nm. During the measurements, a lens was attached to the spectrometer with an instantaneous field of view (IFOV) of 8°. The duration of one measurement for the whole spectral region takes 0.1 second. *Table 1* gives an overview of the sampling interval and spectral resolution of the spectrometer and *Figure 4* shows how they are defined.

*Table 1. The Sampling interval and spectral resolution of the spectrometer for the region 350 - 1000 nm and 1000 – 2500 nm.*

	350 – 1000 nm	1000 – 2500 nm
Sampling Interval	1.4 nm	2 nm
Spectral Resolution	3 nm	10 nm

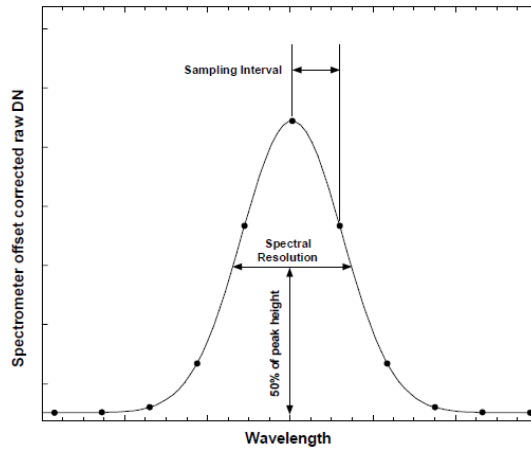


Figure 4. Definition of the sampling interval and the spectral resolution of the spectrometer. The spectral resolution is defined as the full-width-half-maximum (FWHM) of the instrument response to a monochromatic source. Source image: Hatchell (1999).

The spectrometer consists of three separate spectrometers: a visible and near infrared (VNIR) spectrometer and two short wave infrared (SWIR) spectrometers, called SWIR 1 and SWIR 2. The VNIR spectrometer uses a fixed grating, which disperses light onto a fixed array of 512 individual detection elements (Figure 5a). The SWIR 1 and 2 use an up-and-down rotating grating, which disperses the light onto a fixed detector (Figure 5b). The detectors record a signal for each of the 1060 unique positions that the grating can take. The difference between the SWIR 1 and the SWIR 2 is that the SWIR 2 is manufactured for measurements in the longer wavelength region.

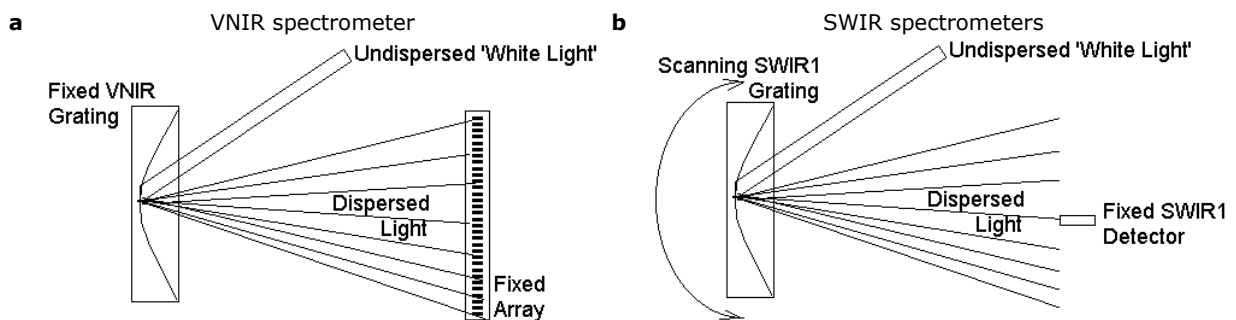


Figure 5. Spectrometers of the ASD: **a)** The VNIR spectrometer of the ASD. A fixed grating Disperses incoming radiance over a fixed array of detectors; **b)** The SWIR 1 and SWIR 2 spectrometers of the ASD. A rotating grating disperses incoming radiance at a fixed detector. Source images: Hatchell (1999).

Once the element and encoder positions are assigned, the positions where the transitions should occur between the VNIR, SWIR 1 and SWIR 2 spectrometers, called splices, are determined. The splice positions between the VNIR and SWIR 1 occurs around 1000 nm and the splice positions between SWIR 1 and SWIR 2 around 1800 nm. The spectrometer chooses several references of reflectance standards with centre-peaks at known wavelengths that are distributed over the 350 – 2500 nm region. Each of these reference points is paired with the known detector (VNIR) or position of the grating (SWIR 1 and SWIR 2). A cubic spline interpolation is applied to pair up the remaining detectors or grating positions and an output is created every 1 nm in the region 350 – 2499 nm.

### 2.1.2 Kawasaki FS10E

The core of the goniometer facility is formed by a Kawasaki FS10E industrial robot arm (*Figure 6*). The robot arm has six degrees of freedom and is able to set the spectrometer at an infinite number of positions around a small target. The robot is very fast (8.8 m/s linear speed) and has a high position repeatability ( $\pm 0.1$  mm). As another advantage, the robot arm is fully programmable.



*Figure 6. Kawasaki FS10E robot arm Source image: Kawasaki Robotics Inc. Product Specification.*

### 2.1.3 Quartz Tungsten Halogen lamp

As a light source, a 1000 watt Quartz Tungsten Halogen (QTH) lamp is used (*Figure 7a*). The QTH lamps are popular due to its smooth spectral curve in the visible and near-infrared part of the spectrum and its stable output (*Figure 7b*).

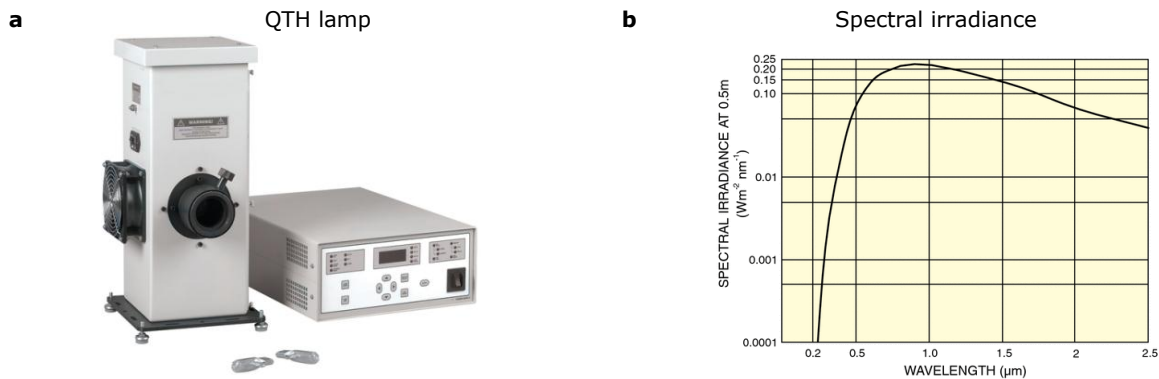


*Figure 7. The illumination source used in the laboratory set-up a) The QTH lamp; b) the spectral irradiance of the QTH lamp. Source images: Newport Corporation. www.newport.com.*

To ensure a constant power of the lamp it was connected to a radiometer power supply (*Figure 7*), which supplied a constant 1000 watt. The light was focussed at the target; however, the light beam was not collimated.

### 2.1.4 Spectralon

Spectralon, a sintered polytetrafluoroethylene material, is commonly used reference material for optical sensors of remote sensing systems (Bruegge et al. 2001). Spectralon panels are valued because they approach Lambertian reflectance at measurements near nadir position in both the visible and near-infrared part of the spectrum and because they are thermally stable (Labsphere

2012). For the laboratory measurements, which are performed in this thesis, a Spectralon panel is used as a reference material.

### 2.1.5 Laboratory

To be able to neglect the contribution of diffuse irradiance on the measurements and in order to avoid scattering, it is important that the laboratory in which the measurements are performed allows for complete darkness (Sandmeier and Strahler 2000). Therefore, the laboratory (the walls, floors and ceiling), as well as the equipment (the sensor, the goniometer, the control units and other instruments), were covered by highly absorbing black material: the walls were covered with panels that were painted with black latex (Sigmatex mat RAL 9450) and the floors and ceiling were covered with black PVC foil. Both the painted wall panels and the PVC foil have a reflectance of less than 4% in both the visible, the near-infrared and the shortwave-infrared, see *Figure 8a*. *Figure 8b* and *Figure 8c* show the laboratory before and after covering the walls, ceiling, floor and other equipment with black materials, respectively.

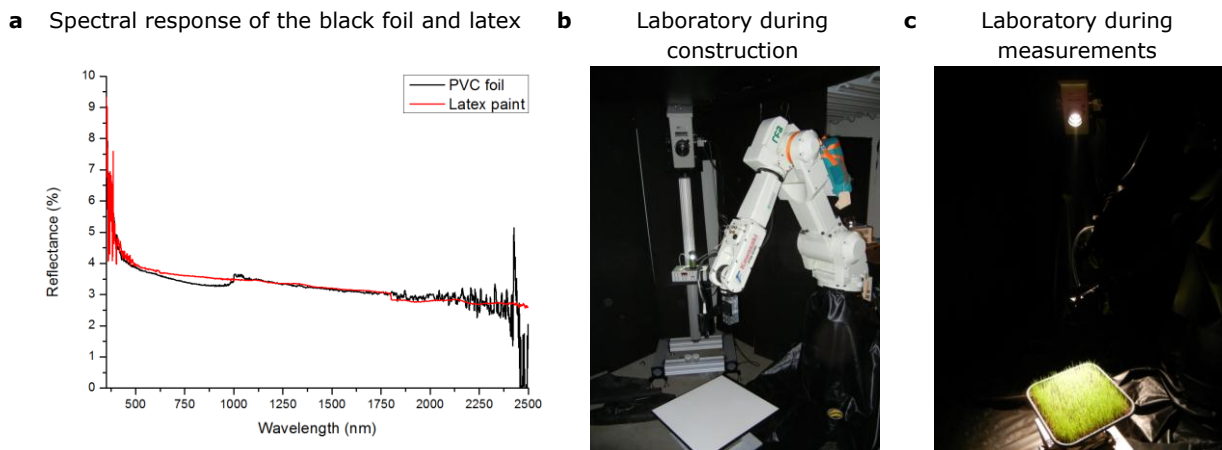


*Figure 8. Darkening the laboratory. a) The spectral response of the PVC foil and the latex paint between 350 and 2500 nm; b) the laboratory before covering the instruments with black materials; c) the laboratory during measurements: the walls, ceiling, floor, robot and other equipment are covered by black panels and PVC foil. The difference in noise level at higher wavelengths is due to the fact that the latex paint was measured with a contact probe, while the foil was measured using the goniometer set-up, as described in this section. Source photographs: Roosjen et al. (2012).*

## 2.2 Measurement positions

Measurements of the soil and vegetation targets were performed at illumination angles of 30° and 45°. The light source was mounted on a pole and therefore, the distance between the light source and the targets varied with an illumination angle of 30° and 45°. The measurements were performed covering a hemisphere up to a view zenith angle (VZA) of 60° off-nadir at a sensor – target distance of 40 cm (Figure 9).

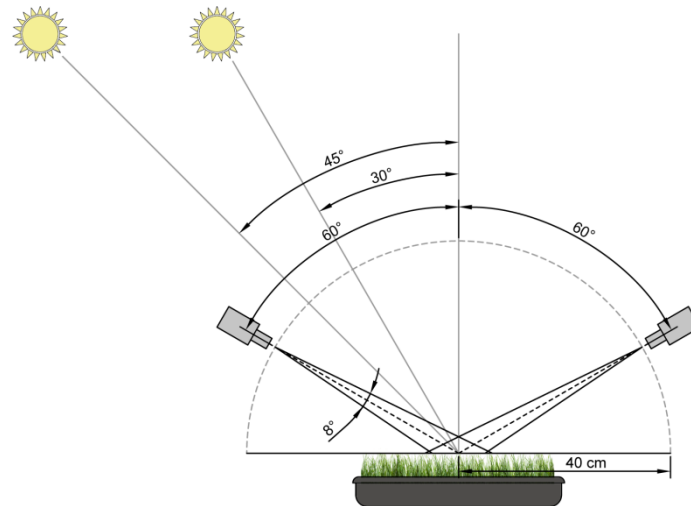


Figure 9. Schematic cross section of the measurement set-up at an illumination angle of 30° and 45°. The measurements were performed covering the hemisphere up to a VZA of 60° off-nadir.

Figure 10 shows the measurement positions from a top-view perspective. Measurements covering the hemisphere were taken at a low resolution (Sandmeier et al. 1998b): a measurement every 30° azimuth and every 15° zenith. Over the principal plane measurements were taken every 5° zenith. Around the hot-spot some additional measurements were taken. During the programming of the measurement positions, the position at  $\theta = 40^\circ$  and  $\varphi = 0^\circ$  was forgotten and not measured.

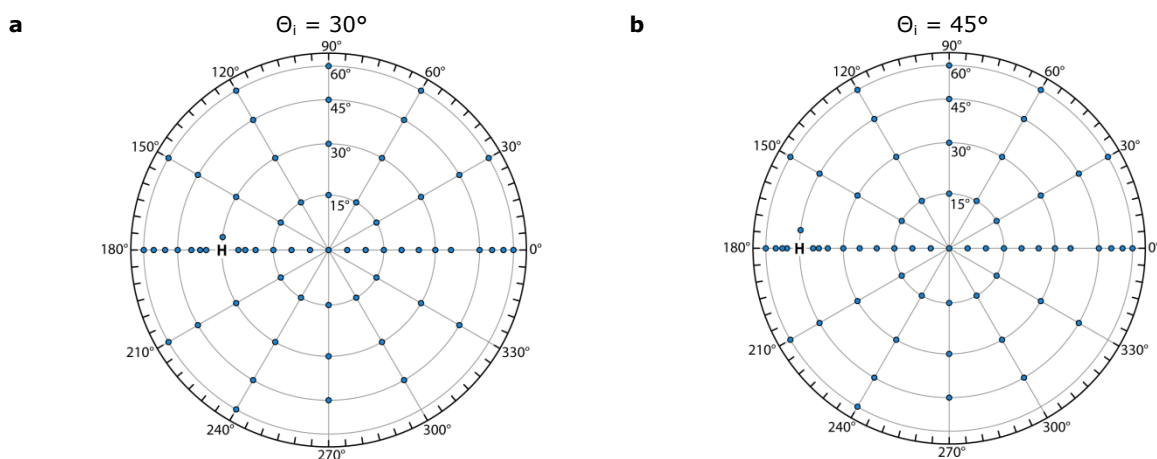


Figure 10. Measurement positions from a top-view perspective at: **a)** an illumination angle of 30°; **b)** an illumination angle of 45°. ‘H’ denotes the position of the hot-spot.

The ‘route’ along the measurement positions is programmed to minimize the chance of twisting and shifting of the fibre optic cables of the spectrometer, because shifting and twisting can cause alteration of the transmission capacity of the fibre optic cables (Combes et al. 2007). The nadir

position was measured several times during a measurement sequence, to determine if the reflected signal had changed due to vegetation stress caused by the strong irradiance of the light source.

## **2.3 Protocol**

This section describes the protocol which was applied during the experiments.

### **2.3.1 Dark current**

Dark-current, or dark-drift, is systematic noise caused by the electronics and detectors of the spectrometer. The dark-current can be determined by viewing a black, near zero reflectance target, or by closing a shutter of the spectrometer. In this way, no illumination energy is able to hit the detectors and thereby, the magnitude of the dark-current can be measured (Hatchell 1999). For the measurements in this thesis the shutter was closed in order to determine the dark-current. Because the dark-current is only stable within a short period of time, a dark-current measurement was taken before each measurements sequence of a target. The dark-current measurement was stored and later on subtracted from the measurements.

### **2.3.2 White reference**

A white reference is used as 'baseline' at which close to 100% of all the radiance of the light source is reflected towards the sensor (Hatchell 1999). The white reference measurements for this thesis were performed by measuring a white Spectralon panel from nadir position, at a sensor – target distance of 40 cm, under the same illumination conditions as the vegetation measurements. Just like the dark-current measurements, a white reference measurement was taken before each measurement sequence.

### **2.3.3 Measurements**

Before the measurement of a target, the dark-current and white reference were determined. After this, the spectrometer was set to nadir position and moved down 40 cm. The target was placed under the spectrometer on a height-adjustable table and moved up such that the top of the canopy was at the same height as the spectrometer. Finally the spectrometer was moved 40 cm up again and the programmed measurement positions over the hemisphere were measured. To increase the signal-to-noise ratio, at each measurement position, 15 measurements were taken and averaged. The goniometer was programmed to measure the nadir positions multiple times during a measurement sequence. This was done in order to determine whether the targets and the spectrometer had remained constant during the measurements. A measurement sequence took just over 16 minutes. Once the measurements of a target were completed, a white Spectralon panel was measured again at nadir position at a sensor – target distance of 40 cm, in order to see if the spectrometer had remained constant during the measurements. If the result of this measurement was not satisfactory the above described protocol was repeated and the target was measured again over the hemisphere.

## 2.4 Terminology

In literature, the terminology concerning multi-angular reflectance measurements is often used incorrectly. The incorrect use of terminology can be a considerable source of systematic error (Schaepman-Strub et al. 2006). The following section gives an overview of the most commonly used reflectance terminology and explains the correct terminology for reflectance quantity of the measurements that are performed for this thesis.

### 2.4.1 Bidirectional reflectance distribution function

The BRDF is the mathematical description of reflectance anisotropy, as defined by Nicodemus et al. (1977). The BRDF ( $f_r$ ) describes the reflectance of a surface as function of incidence irradiance ( $E_i$ ) from a given direction ( $\theta_i, \varphi_i$ ) and radiance ( $L_r$ ) reflected into a specific direction ( $\theta_r, \varphi_r$ ) at a given wavelength ( $\lambda$ ), see equation(1).

$$f_r(\theta_i, \varphi_i; \theta_r, \varphi_r; \lambda) = \frac{dL_r(\theta_i, \varphi_i; \theta_r, \varphi_r; \lambda)}{dE_i(\theta_i, \varphi_i; \lambda)} \quad (1)$$

Where:

- $f_r$  = Bidirectional reflectance distribution function (BRDF) [ $\text{sr}^{-1}$ ]
- $L_r$  = Radiance [ $\text{W m}^{-2} \text{sr}^{-1} \text{nm}^{-1}$ ]
- $E_i$  = Incidence irradiance [ $\text{W m}^{-2} \text{nm}^{-1}$ ]

### 2.4.2 Bidirectional reflectance factor

In practice, it is not possible to measure the BRDF directly. Therefore, angular integration of a number of bidirectional reflectance factors (BRFs) is often used to approximate the BRDF. The BRF ( $R$ ) is defined as the ratio of radiance reflected by a target ( $L$ ) at a specific illumination and viewing geometry ( $\theta_i, \varphi_i; \theta_r, \varphi_r$ ) to the reflected radiance by an ideal (lossless) and perfectly diffuse (Lambertian) (i.e., non-absorbing and non-transmitting (Martonchik et al. 2000)) surface ( $L_{ref}$ ) at the same viewing and illumination geometry at a given wavelength ( $\lambda$ ), Equation (2).

$$R(\theta_i, \varphi_i; \theta_r, \varphi_r; \lambda) = \frac{L(\theta_i, \varphi_i; \theta_r, \varphi_r; \lambda)}{L_{ref}(\theta_i, \varphi_i; \theta_r, \varphi_r; \lambda)} \quad (2)$$

Where:

- $R$  = Bidirectional reflectance factor (BRF) [-]
- $L$  = Radiance [ $\text{W m}^{-2} \text{sr}^{-1} \text{nm}^{-1}$ ]
- $L_{ref}$  = Radiance of a reference panel [ $\text{W m}^{-2} \text{sr}^{-1} \text{nm}^{-1}$ ]

### 2.4.3 Biconical reflectance factor

To measure a BRF, an infinite small sensor IFOV would be required. The BRF of a target can only be approximated by sensors with a small IFOV (of up to  $3^\circ$ ) (Beisl 2001). The smaller the IFOV, the better the approximation of the BRF (Martonchik et al. 2000). For the measurements, which are performed for this thesis, a sensor with an IFOV of  $8^\circ$  was used and besides this, the used light source has a conical field of illumination due to the absence of a collimator. Therefore, the correct terminology for the measurements is the biconical reflectance factor (BCRF), or conical-conical reflectance factor

(CCRF) (Schaepman-Strub et al. 2006). The mathematical description of the biconical reflectance factor is shown in equation (3).

$$R(\theta_i, \varphi_i, \omega_i; \theta_r, \varphi_r, \omega_r; \lambda) = \frac{\int_{\omega_r} \int_{\omega_i} f_r(\theta_i, \varphi_i; \theta_r, \varphi_r; \lambda) * L_i(\theta_i, \varphi_i; \lambda) * d\Omega_i * d\Omega_r}{(\Omega_r/\pi) * \int_{\omega_i} L_i(\theta_i, \varphi_i; \lambda) * d\Omega_i} \quad (3)$$

Where:

- $R$  = Biconical reflectance factor [-]
- $\omega$  = The solid angle of the cone
- $\Omega$  = The projected solid angle of the cone

The measurements, which are performed for this thesis, are here after referred to as biconical reflectance factors or BCRFs.

## 2.5 Targets

40 x 40 cm plots of freshly grown lawn grass (*Lolium perenne* L.) and watercress (*Nasturtium officinale* R.Br.) served as the targets for the multi-angular measurements (*Figure 11*). The lawn grass and watercress vegetation were chosen for their specific LAD. Lawn grass has an erectophile (vertical) LAD and watercress has a planophile (horizontal) LAD (Sandmeier et al. 1998a). Lawn grass leaves are monocotyledonous leaves with a compact mesophyll structure and watercress leaves are dicotyledonous leaves with spongy parenchyma and air cavities (Jacquemoud and Baret 1990). Measurements were performed on 7 and 18 days old lawn grass and watercress canopies.

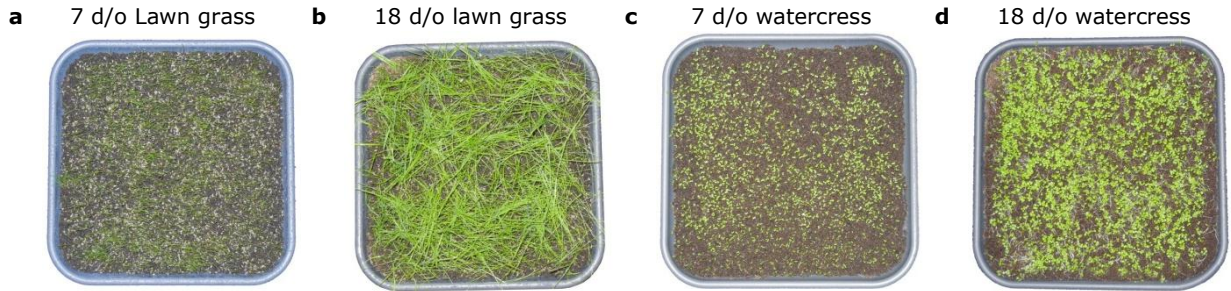


*Figure 11. Photographs taken at approximately nadir position of: a) 7 days old lawn grass; b) 18 days old lawn grass; c) 7 days old watercress; d) 18 days old watercress.*

### 2.5.1 Plot size

To ensure that the spectrometer was only measuring the target at all observation angles, the ground instantaneous field of view (GIFOV) of the spectrometer at all observation angles is calculated using the equations of Dangel et al. (2005). The GIFOV changes from circular at nadir position to elliptical at off-nadir view zenith angles (VZAs). Equation (4) determines the radius of the GIFOV over the circular axis ((b): see *Figure 12b*) of the ellipse at a sensor - target distance ( $d_s$ ) and an IFOV ( $\alpha$ ).

$$b = d_s \tan(\alpha) \quad (4)$$

Where:

- b = Radius over the circular axis of the ellipse [cm]
- $d_s$  = Distance between the sensor and centre of the target [cm]
- $\alpha$  = Half of the sensor IFOV angle [°]

The length of the long axis of the GIFOV in the direction towards the sensor ( $a_s$ ) is shorter compared to the length of the axis away from the sensor ( $a_l$ ), see *Figure 12b*. Equation (5) allows for the calculation of the short and long axis of the GIFOV.

$$a_{s,l} = d_s \frac{\sin(\alpha)}{\sin\left(\frac{\pi}{2} \pm \theta - \alpha\right)} \quad (5)$$

Where:

- $a_s$  = Length over the short axis of the ellipse [cm]
- $a_l$  = Length over the long axis of the ellipse [cm]
- $\theta$  = View zenith angle [°]

With an increasing VZA, both the length of the long and short axis increase and thereby also the surface area that is measured by the spectrometer. This surface area can be calculated by equation (6).

$$A = 0.5a_s b\pi + 0.5a_l b\pi \tag{6}$$

Where:

A = surface area measured by the sensor [cm<sup>2</sup>]

Figure 12a shows the relation between the VZA and the surface area measured by the sensor. At a VZA of 60° the surface area measured by the sensor is almost twice as big compared to the surface area measured at nadir position. Figure 12b shows the GIFOVs in relation to the vegetation targets that are observed by the spectrometer at nadir position and at a VZA of 60°. 60° is the greatest observation VZA applied in this thesis. Even at a VZA of 60°, the GIFOV of the spectrometer does not reach outside the vegetation plot. This ensures that at all VZAs, only the actual target is observed.

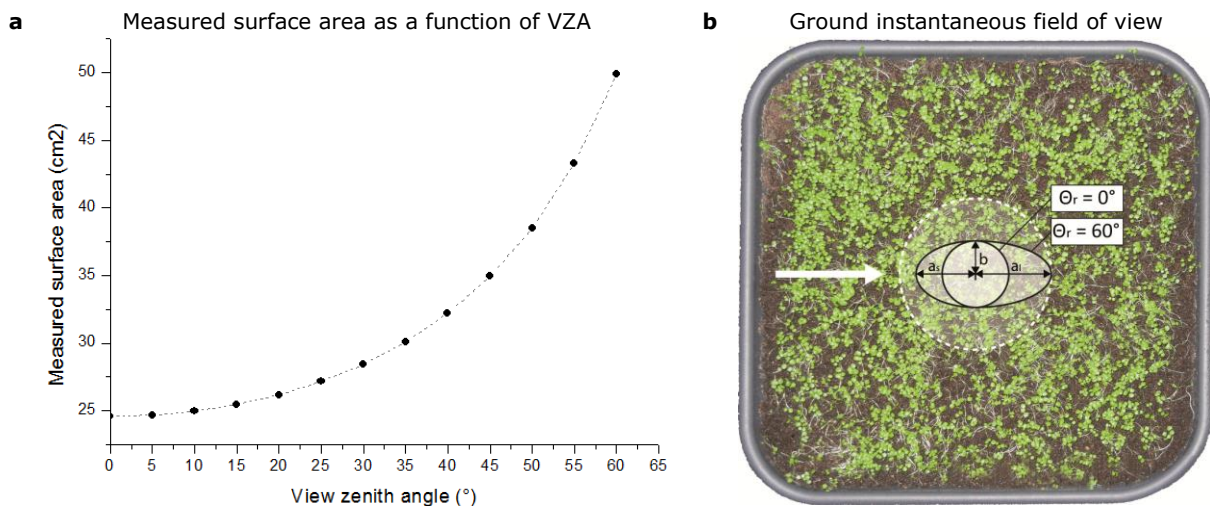


Figure 12. Relation between the VZA and the observed surface area: **a)** for an IFOV of 8° and a sensor – target distance of 40 cm; **b)** a visualization of the area that is measured at nadir position and at a VZA of 60°. The arrow indicates the viewing direction that results in the depicted GIFOV and the dashed circle indicates the theoretical range of the covered area at different viewing directions.

### 2.5.2 Sowing density

The Lawn grass was sown at a density of 260 grams of seeds per square meter and the watercress at a density of 4 grams of seeds per square meter. The seeds were distributed as evenly as possible.

### 2.5.3 Soil

The soil on which the lawn grass and watercress was grown had a specific composition, based on mull (peat dust), sand and lime, which makes it suitable for fast germination of seeds. It has an organic matter content of 17% and contained 0.6 kg/m<sup>3</sup> fertilizer (14% nitrogen, 16% phosphorus and 18% potassium).

### 2.5.4 Growing conditions

The growing conditions were not optimal. Since the laboratory measurements took place in the end of January, the lawn grass and watercress were sown in the beginning of January, which is mid-winter in the Netherlands. Therefore, only a limited amount of sunlight was available. The vegetation was grown inside an office, next to a window.

### 2.5.5 Vegetation cover

Each of the vegetation targets had a different proportion of vegetation cover, which was determined as follows: first a photograph of the individual vegetation targets was taken at approximately nadir position, using a Nikon Coolpix S8100 digital camera (*Figure 13a*). Second, the images were spatially geocoded and resampled using Erdas Imagine 2011 version 11.0.4 software, based on the known coordinates of the ground control points (GCPs) in *Figure 13b*. By applying a fourth order polynomial transformation based on 16 GCPs, an output image with a cell size of 1 x 1 mm was created. A fourth order polynomial transformation was applied, because this returned the lowest root mean squared error (RMSE) and produced a visually good result, see *Figure 13c*. Thirdly, the vegetated pixels were separated from the non-vegetated by applying equation (7) in the Erdas Imagine modeller (*Figure 13d*).

$$(Green > Blue) \text{ AND } (Green > Red) \text{ AND } (Green > 90^*) \tag{7}$$

Where:

- Green = The pixel value of a pixel in the green band
- Blue = The pixel value of a pixel in the blue band
- Red = The pixel value of a pixel in the red band

\*90 is used as a threshold to make sure that soil pixels with a higher green than red and blue pixel value are not selected.

Based on a visual assessment, the classification of vegetated pixels was found sufficient. See *Figure 13d* for the classification result of the 18 days old watercress.

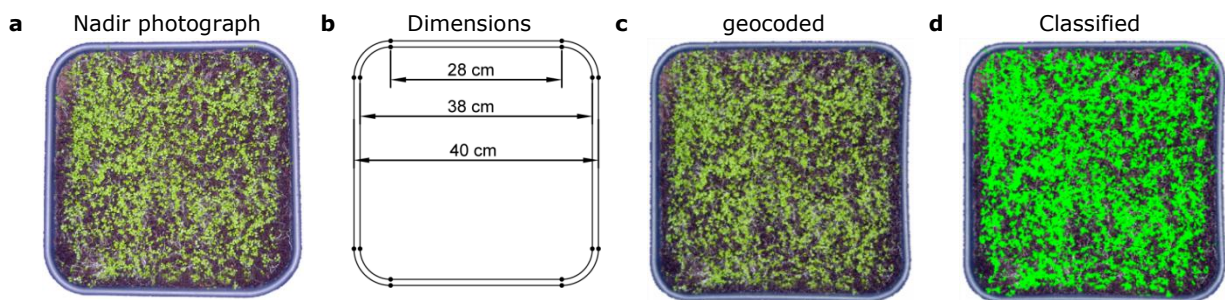


*Figure 13. 18 days old watercress: a) a photograph taken at approximately nadir position; b) known GCPs (black dots) that are used for the geocoding and resampling; c) the result of the resampling method; d) pixels that are classified as vegetation by applying equation (7).*

By multiplying the known pixel size of the resampled images with the number of pixels classified as vegetation, the percentage vegetation cover was determined, see *Table 2*.

### 2.5.6 Leaf orientation value

The Leaf Orientation Value (LOV), as defined by Pepper et al. (1977), is a function, which can be used to describe the LAD. The LOV is determined using equation (8).

$$LOV = \sum_{i=1}^n ([\theta(l_f/l)]_i/n) \tag{8}$$

Where:

- LOV = Leaf Orientation Value [°]
- θ = Leaf angle from horizontal at stalk [°]
- l<sub>f</sub> = Length from leaf collar to flagging point [cm]
- l = Total leaf blade length [cm]
- n = Number of measured leaves [-]

To determine the LOV, per target, a sample of 30 leaves was used. Vegetation with a LOV greater than 45 are considered as erectophile, based on the classification of Huang et al. (2011). The LOVs of the 7 and 18 days old lawn grass and the 7 and 18 days old watercress are shown in *Table 2*. It was not possible to determine the LOV of the 7 and 18 days old watercress due to the small size of the leaves.

### 2.5.7 Leaf and canopy dimensions

The leaf dimensions: the average leaf width and average leaf length are based on a sample of 30 leaves. The leaf dimensions of the 7 and 18 days old lawn grass and the 7 and 18 days old watercress, together with the average canopy height, are shown in *Table 2*.

*Table 2. Overview of the properties of the lawn grass and old watercress targets. LOV, average leaf length and average leaf width are based on a sample of 30 measurements per vegetation target.*

Vegetation type	Vegetation coverage (%)	Average height (cm)	LOV (°)	Average leaf length (cm)	Average leaf width (cm)
7 days old lawn grass	28.52	4.09 (1.04)	52.72 (4.73)	4.58 (1.10)	0.075**
18 days old lawn grass	71.74	7.23 (1.39)	74.68 (12.80)	9.89 (1.90)	0.1**
7 days old watercress	17.45	0.5**	***	0.3 (0.06)*	0.3 (0.06)*
18 days old watercress	42.75	1**	***	0.19 (0.08)*	0.19 (0.08)*

*The values between brackets indicate the standard deviation.*

*\* The watercress leaves were approximately round. Therefore, the leaf length and leaf width are equal.*

*\*\* Values based on an estimation: the targets were too small to measure this.*

*\*\*\* It was not possible to determine the LOV due to the small size of the leaves.*

## 2.6 Soil-leaf-canopy model

The SLC-model (Verhoef and Bach 2007), is a RT model, which is able to simulate a canopy layer and soil BRDF background by means of the four-stream flux interaction concept (Verhoef 1985; Verhoef and Bach 2003). The SLC-model combines the modified Hapke soil BRDF model (Hapke 1981), a robust version of the PROSPECT leaf model (Jacquemoud and Baret 1990), and 4SAIL2, a canopy RT model (Verhoef 1984). For the simulations, performed for this thesis, a demo version of the SLC-model was used. *Table 3* gives an overview of the input parameters of the SLC-model (Verhoef and Bach 2012).

*Table 3. Overview of the input parameters of the SLC-model and their units. Source: (Verhoef and Bach 2012).*

Parameter	Description	Unit
Hapke_b	Hapke phase function parameter b	-
Hapke_c	Hapke phase function parameter c	-
Hapke_h	Hapke hot-spot width parameter	-
Hapke_B0	Hapke hot-spot magnitude parameter	-
SM %	Soil moisture percentage	-
Cab_green	Chlorophyll content green leaves	$\mu\text{g}/\text{cm}^2$
Cw_green	Water content green leaves	$\text{g}/\text{cm}^2$
Cdm_green	Dry matter content green leaves	$\text{g}/\text{cm}^2$
Cs_green	Brown pigment content green leaves	-
N_green	Mesophyll structure parameter green leaves	-
Cab_brown	Chlorophyll content brown leaves	$\mu\text{g}/\text{cm}^2$
Cw_brown	Water content brown leaves	$\text{g}/\text{cm}^2$
Cdm_brown	Dry matter content brown leaves	$\text{g}/\text{cm}^2$
Cs_brown	Brown pigment content brown leaves	-
N_brown	Mesophyll structure parameter brown leaves	-
LAI	Total leaf area index (per crown)	$\text{m}^2/\text{m}^2$
LIDFa	LIDF parameter a	-
LIDFb	LIDF parameter b	-
hot	Hot-spot parameter	-
fB	Fraction brown leaf area	-
Diss	Layer dissociation factor	-
Cv	Vertical crown cover fraction	-
zeta	Tree shape factor	-
sza	Solar zenith angle	degree
vza	Viewing zenith angle	degree
raa	Relative azimuth angle	degree

In the following sections, an overview of the SLC parameters and how their values were determined are described. First, the soil parameters will be described, followed by the leaf parameters and finally the canopy parameters. Some measurements were performed in order to obtain the parameter values of chlorophyll content, LAI, hot-spot size and tree shape factor. Therefore, they could be seen as part of the results, however, since the emphasis of this thesis is on the spectral measurements and simulations, they are considered as part of the methodology.

## **2.6.1 SOIL**

This section describes the soil parameters, which are based on Hapke soil BRDF model (Hapke 1981). Due to limited knowledge about the soil parameters, the soil parameters were left at their default values, which are based on values that Pinty et al. (1989) found for a ploughed soil.

### **2.6.1.1 Hapke b and c**

The Hapke b and c parameters are the coefficients of the Legendre polynomial expansion used to describe the particle phase function. Hapke b = 0.84 and Hapke c = 0.68 were used for the simulations.

### **2.6.1.2 Hapke $B_0$**

The parameter  $B_0$  describes the relative magnitude of the hot-spot peak (Hapke 1981; Verhoef and Bach 2007). The value of  $B_0$  was set at 0.23.

### **2.6.1.3 Hapke h**

The Hapke h parameter is used to characterize hot-spot surge, which can be related to the grain size distribution, the porosity and the gradient of compaction with depth (Pinty et al. 1989). For the simulations, Hapke h was set at 0.30.

### **2.6.1.4 SM%**

The SM% parameter describes the soil moisture content. The SM% value was set at its default value of 5%.

### **2.6.1.5 Input spectral signature soil**

Several different soil signatures are already pre-programmed in the demo version of the SLC-model. However, none of these spectral signatures appears similar to the spectral signature of the soil on which the vegetation was grown. Therefore, nadir measurements of the soil, acquired at an illumination angle 30° and 45° were used as an input for the SLC-model simulations.

The SLC-model uses the single scattering albedo as an input in order to produce a reflectance factor. Therefore, the measured soil reflectance was transformed to single scattering albedo data. However, the relation between single scattering albedo and soil reflectance is wavelength dependent and there is no clear mathematical method to perform this transformation. Therefore, the nadir measurements of the bare soil at an illumination angle of 30° and 45° were used as the single scattering albedo input and a reflectance factor (with the viewing and illumination settings in the SLC-model set exactly the same as during the laboratory measurements) was created. By using Microsoft Excel, a 2<sup>nd</sup> order polynomial relation between the single scattering albedo and the reflectance factor was determined, see *Figure 14*.

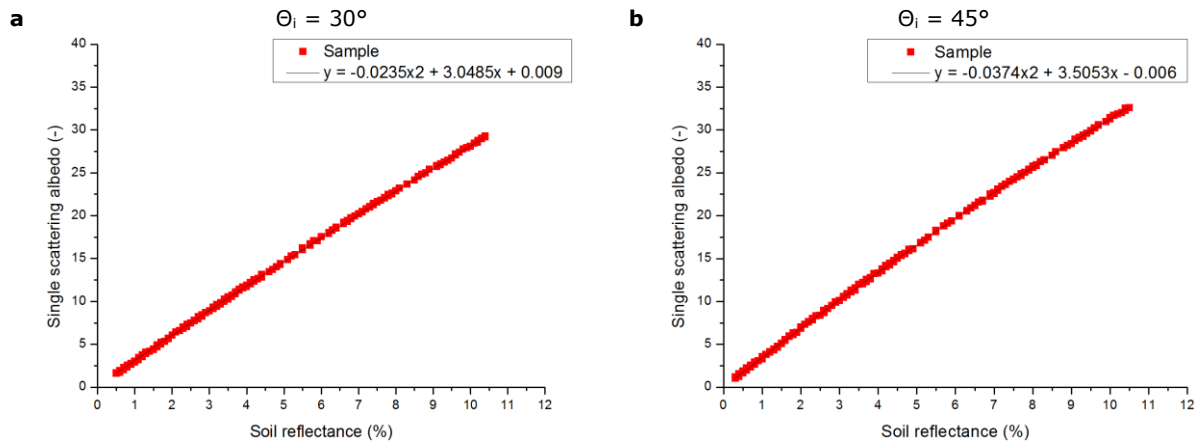


Figure 14. Relation between single scattering albedo and the soil reflectance output of the SLC-model at **a)**  $\vartheta_i = 30^\circ$ ; **b)**  $\vartheta_i = 45^\circ$ . Both functions have a  $R^2$  of 0.9999.

The measured soil signature was transformed to the single scattering albedo by applying the equations in Figure 14. This resulted in a RMSE of 0.475% and 0.087%, for  $\theta_i = 30^\circ$  and  $\theta_i = 45^\circ$  respectively, of the soil signature and the single scattering albedo. This single scattering albedo input is used later on to do the simulations of the laboratory measurements.

## 2.6.2 LEAF

This section describes the collection and determination of the leaf parameters, which are based on PROSPECT leaf model (Jacquemoud and Baret 1990). PROSPECT is a radiative transfer model, which is based on the plate model (Allen et al. 1969), where a leaf is assumed to be a stack of several plates with a refractive index and absorption coefficient, which are separated by air spaces. The absorption of the leaves is defined as a linear combination of its biochemical properties and the corresponding absorption coefficient.

### 2.6.2.1 Chlorophyll content

Several methods, both destructive and non-destructive, exist for the determination of the chlorophyll content. A commonly used non-destructive method to determine the chlorophyll content is by the use of a SPAD meter. However, the SPAD only measures the relative chlorophyll content, which is not suitable as input parameter for the SLC-model, since the chlorophyll content input parameter of the SLC-model is expressed in  $\mu\text{g}/\text{cm}^2$ . Besides this, the leaves of the lawn grass and the watercress were too small to be measured by a SPAD. Therefore a destructive method to measure the chlorophyll content, developed by Bruinsma (1963), was applied. This commonly used method (e.g. de Kok et al. (1978); Lance and Guy (1992); Kawa-Miszczak et al. (2009); Yin and Ashihara (2009); Botha et al. (2010)) is able to determine the chlorophyll content based on the absorption coefficients at the chlorophyll a and chlorophyll b absorption at particular wavelengths in the red region of the spectrum. A detailed explanation of this method and the protocol that was followed in order to get the results is given below.

Of the 7 days and 18 days old lawn grass and watercress, four samples of 5000  $\mu\text{g}$  were taken and weighed using a Mettler AE260 Delta Range weighing device. A sample of 5000  $\mu\text{g}$  resembles approximately one or two grass haulms of the 18 days old lawn grass, two to three grass haulms of the 7 days old lawn grass, three to four leaves of the 18 days old watercress and six to eight leaves of the 7 days old watercress.

The samples were frozen to  $-80^\circ\text{C}$  for 30 minutes immediately after they were collected and weighed. After this, the samples were crushed using a mortar and 1 ml of 100% acetone was added. Next, the samples were homogenized for two minutes using an Eppendorf 5432 mixer. Finally, the acetone solvent was separated from the crushed leaves by placing them in an Eppendorf 5417C centrifuge for 1 minute at 12000 RPM (or 15300 RCF). The acetone, containing the dissolved chlorophyll was collected and again 1 ml of 100% acetone was added to the samples and the mixing and centrifuging was repeated. In order to extract all the chlorophyll from the samples, this procedure was repeated until the crushed leaves appeared colourless (white). For all the samples, the crushed leaves appeared colourless after repeating this procedure twice. Since chlorophyll is highly volatile, the samples were kept in ice during the whole procedure to make sure that the chlorophyll would not volatilize.

The chlorophyll of all samples was solved in 2 ml of acetone. Of this 2 ml, 1 ml was placed into a 1 ml cuvette. As a final step, the absorption coefficients of the samples were measured by a Beckman DU<sup>®</sup> 7500 UV spectrophotometer at 644.8 nm and at 661.6 nm. As a reference point for the absorption coefficients, a blank (a 1 ml cuvette containing only the 100% acetone) was measured. By applying

equation (9) and (10), the chlorophyll a and b content, respectively, in  $\mu\text{g/ml}$  can be calculated. Equation (11) gives the total chlorophyll a and chlorophyll b concentration (Lichtenthaler 1987).

$$c_a = 11.24A_{661.6} - 2.04A_{644.8} \quad (9)$$

$$c_b = 20.13A_{644.8} - 4.19A_{661.6} \quad (10)$$

$$C_{a+b} = 7.05A_{661.6} - 18.09A_{644.8} \quad (11)$$

Where:

- $c_a$  = Chlorophyll a concentration [ $\mu\text{g/ml}$ ]
- $c_b$  = Chlorophyll b concentration [ $\mu\text{g/ml}$ ]
- $C_{a+b}$  = Chlorophyll a and b concentration [ $\mu\text{g/ml}$ ]
- $A_{644.8}$  = Extinction rate measured at 644.8 nm
- $A_{661.6}$  = Extinction rate measured at 661.8 nm

By using the LAI (see section 2.6.3.1) the units were transformed from  $\mu\text{g/ml}$  to  $\mu\text{g/cm}^2$ . The average chlorophyll content of 7 and 18 days old lawn grass and 7 and 18 days old watercress in  $\mu\text{g/cm}^2$  can be found in *Table 4*. These results are used as an input to the SLC-model.

*Table 4. Chlorophyll content of 7 and 18 days old lawn grass and 7 and 18 days old watercress*

Vegetation type	Chlorophyll content ( $\mu\text{g/cm}^2$ )
7 days old lawn grass	99.43 (7.28)
18 days old lawn grass	123.65 (10.10)
7 days old watercress	69.35 (28.32)
18 days old watercress	88.10 (40.88)

*The values between brackets indicate the standard deviation.*

### 2.6.2.2 Water content and Dry matter content

The water content (Cw) parameter describes the water content within a leaf in  $\text{g/cm}^2$ . The percentage water content can easily be determined by subtracting the dry weight of the vegetation from the fresh weight of the vegetation. The difference between the two is the water content (Seelig et al. 2008). However, the vegetation samples were accidentally destroyed before the dry weight could be measured. Therefore, a water content percentage of 75% was used, based upon the control group in an experiment with grasses performed by Al-Qahtani (2009). The water content in  $\text{g/cm}^2$  was determined as a function of the percentage water content, combined with LAI (section 2.6.3.1) and the fresh weight of the samples. The dry matter content (Cdm) is determined as the remaining 25% of the weight. The water content and dry matter content are shown in *Table 5*.

*Table 5. Water content and dry matter content of 7 and 18 days old lawn grass and 7 and 18 days old watercress in  $\mu\text{g}/\text{cm}^2$ .*

Vegetation type	Water content ( $\text{g}/\text{cm}^2$ )	Dry matter content ( $\text{g}/\text{cm}^2$ )
7 days old lawn grass	0.0133	0.0044
18 days old lawn grass	0.0303	0.0101
7 days old watercress	0.0007	0.0002
18 days old watercress	0.0015	0.0005

### **2.6.2.3 Brown pigment content**

The Cs parameter is used to describe the brown pigment content. Based on a visual inspection of both the lawn grass and watercress canopies, there was no brown pigment found. Therefore the Cs parameter is not taken into account during the simulations.

### **2.6.2.4 Mesophyll structure parameter**

The N parameter describes the mesophyll structure of the leaves (Jacquemoud and Baret 1990). Lawn grass is a monocotyledonous plant species and watercress is a dicotyledonous plant species. N values ranging between 1 and 1.5 represent monocotyledonous leaves with a compact mesophyll structure and N values ranging between 2 and 2.5 correspond to dicotyledonous leaves with spongy parenchyma and air cavities (Jacquemoud and Baret 1990). As input value for the SLC-model, the average values of the ranges were used: N = 1.25 for the lawn grass and N = 2 for the watercress.

### 2.6.3 CANOPY

The canopy parameters, which are used as input to the SLC-model, originate from the 4SAIL2 model of Verhoef (1984). This section describes the used parameter settings and how the canopy parameters were determined.

#### 2.6.3.1 Leaf area index

The LAI, as first defined by Watson (1947), is expressed by ratio of one-sided leaf surface (m<sup>2</sup>) to the ground surface (m<sup>2</sup>). The LAI of the vegetation targets is determined by collecting the leaves within a known surface area (a quarter of the vegetation plots), pasting them on a white A4 size paper and scanning them using a Canon PIXMA MG5100 scanner. The scanned images were classified in two classes: vegetation and non-vegetation. Since the surface area of an A4 paper is known, the surface area of the leaves could be calculated. *Table 6* shows the LAI of 7 and 18 days old lawn grass and 7 and 18 days old watercress. These LAI values are used as input to the SLC-model.

*Table 6. Leaf area index of 7 and 18 days old lawn grass and 7 and 18 days old watercress.*

Vegetation type	Leaf Area Index (LAI)
7 days old lawn grass	0.79
18 days old lawn grass	1.20
7 days old watercress	0.18
18 days old watercress	0.28

#### 2.6.3.2 Leaf inclination distribution function

The leaf inclination distribution function (LIDF) parameters describe the shape and orientation of the leaves. LIDFa controls the average leaf inclination and LIDFb influences the shape of the leaves distribution (Verhoef 1998). For the simulations with the SLC-model, extreme version parameters were used: for the lawn grass LIDFa = -1 and LIDFb = 0, corresponding to a canopy that consists of completely vertical leaves and for the watercress LIDFa = 1 and LIDFb = 0, corresponding to a canopy that consists of completely horizontal leaves.

#### 2.6.3.3 Hot-spot size parameter

The hot-spot size parameter (hot) is established as a function of length and width of the leaf projected on a horizontal plane, as observed from nadir position, and the canopy height (Verhoef and Bach 2007), based upon equations of (Kuusk 1985). For this thesis, the average leaf length ( $l_{leaf}$ ), the average leaf width ( $w_{leaf}$ ) and the average canopy height ( $h_{canopy}$ ) based on a sample of 30 leaves, is used to determine the hot-spot size parameter (Equation(12)).

$$Hot = \frac{l_{leaf} * w_{leaf}}{h_{canopy}} \quad (12)$$

Where:

Hot = Hot-spot size parameter [-]

$l_{leaf}$  = Average leaf length projected on the horizontal plane [cm]

$w_{leaf}$  = Average leaf width projected on the horizontal plane [cm]

$h_{canopy}$  = Average canopy height [cm]

In *Table 7*, the hot-spot size parameters of 7 and 18 days old lawn grass and 7 and 18 days old watercress can be found.

*Table 7. Hot-spot size parameter of 7 and 18 days old lawn grass and 7 and 18 days old watercress.*

Vegetation type	Hot-spot size parameter
7 days old lawn grass	0.0089
18 days old lawn grass	0.0507
7 days old watercress	0.0587
18 days old watercress	0.0691

#### 2.6.3.4 Fraction brown leaf area

The fraction brown leaf area (fB) parameter allows for the mixing of green and brown elements within a canopy. Since there are no brown elements present in the canopies of both the lawn grass and the watercress, the fB parameter was not taken into account during the simulations.

#### 2.6.3.5 Dissociation factor

The dissociation factor (diss) is a parameter, which describes the distribution of the brown material between two canopy layers. Since there was no brown material present in both the lawn grass and the watercress, this parameter was not taken into account.

#### 2.6.3.6 Vertical crown cover fraction

The vertical crown cover fraction (Cv) parameter describes the crown clumping effect through the crown cover. Because the vegetation was as evenly distributed as possible, no clumping was assumed and therefore the parameter was set at 100, corresponding to an evenly distributed canopy.

#### 2.6.3.7 Tree shape factor

The tree shape factor (zeta) is defined as the ratio of the average crown diameter as observed from nadir position ( $0.5(r_l + r_w)$ ) to the average height of the crown centre above ground ( $0.5(h_{\text{canopy}})$ ). The tree shape factor is calculated for individual leaves using equation (13).

$$\text{Zeta} = \frac{0.5(r_l + r_w)}{0.5(h_{\text{canopy}})} \quad (13)$$

Where:

Zeta = Tree shape factor [-]

$r_l$  = Radius from the centre over the leaf till the edge over de length of the leaf, projected on the horizontal plane [cm]

$r_w$  = Radius from the centre over the leaf till the edge over de width of the leaf, projected on the horizontal plane [cm]

$h_{\text{canopy}}$  = The average canopy height (*Table 2*) [cm]

In *Table 8*, the tree shape parameters of 7 and 18 days old lawn grass and 7 and 18 days old watercress can be found.

*Table 8. Tree shape factor of 7 and 18 days old lawn grass and 7 and 18 days old watercress.*

Vegetation type	Tree shape factor
7 days old lawn grass	0.0681
18 days old lawn grass	0.2606
7 days old watercress	0.1933
18 days old watercress	0.1483

However, if  $C_v = 100$ , the tree shape factor is non-influential (Laurent et al. 2011b). The values in *Table 8* are used during the simulations, but had no effect on the outcome.

### 2.6.4 SLC-model input parameters

*Table 9* gives an overview of the SLC-model parameters as they were used to simulate the laboratory measurements. These parameters settings were used to simulate all the positions in the hemisphere that were measured in the laboratory.

*Table 9. An overview of the input parameters for the SLC-model as used during the simulations.*

Parameter	Unit	Lawn grass		Watercress	
		7 days old	18 days old	7 days old	18 days old
Hapke_b	-	0.84	0.84	0.84	0.84
Hapke_c	-	0.68	0.68	0.68	0.68
Hapke_h	-	0.30	0.30	0.30	0.30
Hapke_B0	-	0.23	0.23	0.23	0.23
SM %	-	5	5	5	5
Cab_green	$\mu\text{g}/\text{cm}^2$	99.28	123.46	74.42	87.97
Cw_green	$\text{g}/\text{cm}^2$	0.0133	0.0303	0.0007	0.0015
Cdm_green	$\text{g}/\text{cm}^2$	0.0044	0.0101	0.0002	0.0005
Cs_green	-	0	0	0	0
N_green	-	1.25	1.25	2	2
Cab_brown	$\mu\text{g}/\text{cm}^2$	0	0	0	0
Cw_brown	$\text{g}/\text{cm}^2$	0	0	0	0
Cdm_brown	$\text{g}/\text{cm}^2$	0	0	0	0
Cs_brown	-	0	0	0	0
N_brown	-	0	0	0	0
LAI	$\text{m}^2/\text{m}^2$	0.79	1.2	0.18	0.28
LIDFa	-	-1	-1	1	1
LIDFb	-	0	0	0	0
hot	-	0.0088	0.0507	0.0587	0.0691
fB	-	0	0	0	0
D	-	0	0	0	0
Cv	-	100	100	100	100
zeta	-	0.0681	0.2606	0.1933	0.1483
sza	deg	varies	varies	varies	varies
vza	deg	varies	varies	varies	varies
raa	deg	varies	varies	varies	varies

## 2.7 Pre-processing

A common known problem of multi-angular reflectance measurements using a goniometer is the shadow that is casted over the target when the sensor is positioned between the light source and the target (close to, or at the hot-spot position) (Sandmeier and Strahler 2000). Shadows cause incorrect measurement results and the positions at which a shadow occurs should be left out of the analysis. The problem of shadows also is an issue at the goniometer facility. Although the robot arm is programmed very carefully to measure close to the hot-spot position and to avoid the arm itself to be positioned in the hot-spot, there are still some positions at which there is a shadow over the target. In order to determine whether the sensor or the robot arm was casting a shadow at a certain position, the Spectralon reference panel was measured at all the positions, at which the vegetation targets were measured as well. Positions where a BCRF  $< 0.8$  was measured were left out of the analysis. At an illumination angle of  $30^\circ$ , ten positions of the 62 unique positions that were measured, were left out because the inspection of the reflectance of the Spectralon panel indicated the influence of shadows (*Figure 15a*). At an illumination angle of  $45^\circ$ , only two positions were not included in the analysis due to the influence of shadows (*Figure 15b*). The positions at  $60^\circ$  zenith and  $270^\circ$ ,  $300^\circ$  and  $330^\circ$  azimuth were not measured, because it was already known from former experiments that the robot arm is not able to reach these positions, since they were located on the opposite site of the robot.

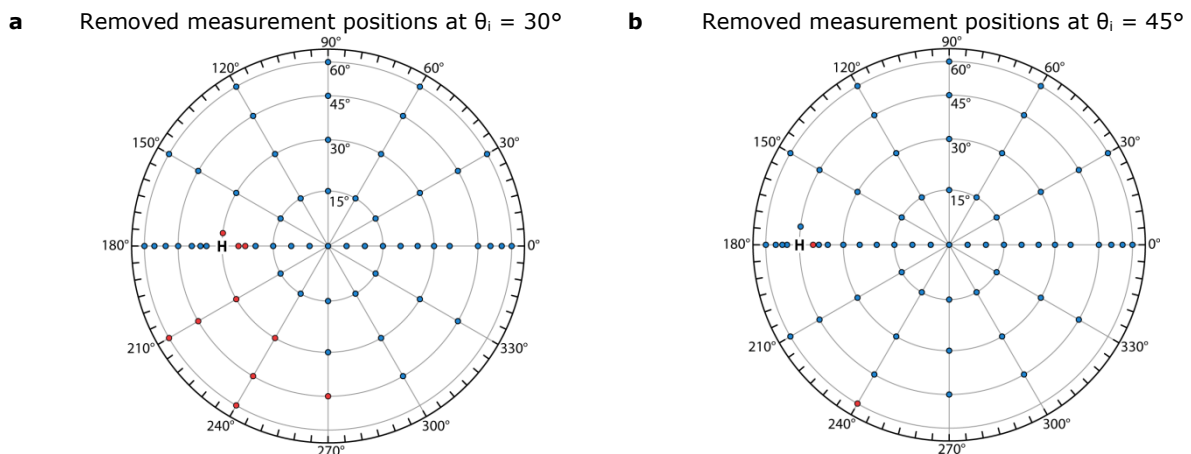


*Figure 15. Positions that were influenced by shadows caused by the robot arm over the targets for: a)  $\vartheta_i = 30^\circ$ ; b)  $\vartheta_i = 45^\circ$ . The red dots indicate the measurement positions that were influenced by shadows and the blue dots indicate the measurements which were not influenced.*

In order to concentrate on anisotropic reflectance effects, all reflectance data is normalized to a standard reflectance. In this way, anisotropic effects were separated from the underlying reflectance of the measured targets (Sandmeier et al. 1998a). In order to normalize the reflectance of the targets, the nadir reflectance is used. The result of this nadir normalization is called the anisotropy factor (ANIF), see equation (14) as defined by Sandmeier et al. (1998a). The ANIF describes the proportion of reflected radiance ( $R$ ) into a specific direction ( $\theta_r, \varphi_r$ ) at a given illumination geometry ( $\theta_i, \varphi_i$ ) at a given wavelength ( $\lambda$ ) relative to the nadir reflectance factor ( $R_0$ ) at the same illumination geometry. The ANIF is strongly dependent on the illumination geometry. Using the spectral albedo for normalization would therefore be better, because it does not depend on the illumination geometry (Strub et al. 2002). However, to make the results in this thesis comparable to the results of

Sandmeier et al. (1998a), who also measured the reflectance anisotropy of lawn grass and watercress canopies, normalization by the nadir reflectance factor has been applied.

$$ANIF(\lambda, \theta_i, \varphi_i, \theta_r, \varphi_r) = \frac{R(\lambda, \theta_i, \varphi_i, \theta_r, \varphi_r)}{R_0(\lambda, \theta_i, \varphi_i)} \quad (14)$$

Where:

ANIF = Anisotropy factor

R = Reflectance factor

R<sub>0</sub> = Nadir reflectance factor

Reflectance anisotropy is wavelength dependent. Most reflectance anisotropy for vegetation occurs at wavelengths where there is relatively high proportion of absorption. In the NIR, the low proportion of absorption and thus higher proportion of (multiple) scattering results in a reduction of the contrast between illuminated and shadowed parts of the canopy (Kimes 1983). Sandmeier et al. (1998a) introduced the anisotropy index (ANIX), which is able to capture the quantity of reflectance anisotropy of a target per spectral band. The ANIX is the ratio of the maximum and minimum reflectance factor, R<sub>max</sub> and R<sub>min</sub>, respectively, over a defined azimuthal plane (equation (15)). The principal plane is often used to determine the ANIX, because the greatest differences in reflectance factors occur here.

$$ANIX(\lambda) = \frac{R_{max}(\lambda)}{R_{min}(\lambda)} \quad (15)$$

Where:

ANIX = Anisotropy index

R<sub>max</sub> = Maximum reflectance factor

R<sub>min</sub> = Minimum reflectance factor

Anisotropy indices are computed for all measured and simulated targets, in order to describe their quantity of anisotropic reflectance effects.

Polar plots are commonly used for the presentation of multi angular measurements over a hemisphere (e.g. Combes et al. (2007); Schopfer et al. (2008)). Polar plots are surface graphs of XYZ data, plotted in a 2D space (OriginLab 2007). Polar plots are able to give an overview of the anisotropic reflectance effects over the full hemisphere. In order to create a polar contour plot, the locations of the measurement positions are described in polar coordinates. The original measurement positions are saved together with the corresponding zenith and azimuth angle. The zenith angles range from -60° to 60° and the azimuth angles from 0° to 180° to describe the measured hemisphere. These coordinates are transformed to polar coordinates which consist of an angle (*theta*) and a radius (*r*). The angle ranges from 0° to 360°. The radius describes the distance between a measurement position and the nadir position. After the transformation to polar coordinates, the dataset consists of an angle, a radius and a BCRF measurement at a specific wavelength ranging from 350 nm to 2499 nm, see *Table 10*.

*Table 10. Structure of the dataset for the creation of polar contour plots.*

Radius (theta)	Radius (r)	350 nm	... nm	2499 nm
0° - 359°	Distance from nadir position	BCRF measurement at 350 nm	BCRF measurement at ... nm	BCRF measurement at 2499 nm

The polar plots in this thesis are created with OriginPro 8.5.0 SR1 (OriginLab, Corporation, MA, Northampton, USA) software. The polar plots are drawn in three steps which are applied by default by the OrginPro software: triangulation, linear interpolation and B-spline smoothing (for a detailed description see the OriginPro user guide: OriginLab (2007)).

To assess the ability of the SLC-model to reproduce the laboratory measurements, RMSE of the measured and simulated reflectance, for all wavelengths in the range 400 nm to 2400 nm at a 10 nm interval, has been calculated using equation (16). The BCRFs of the laboratory measurements and the BRFs simulated by the SLC-model are both multiplied by a factor 100 in order to convert them to reflectance values.

$$RMSE = \sqrt{\frac{1}{n} \sum_{j=1}^n (\rho_j - \hat{\rho}_j)^2} \tag{16}$$

Where:

$\rho$  = Reflectance simulated by the SLC-model [%]

$\hat{\rho}$  = Reflectance measured by the spectrometer in the laboratory [%]

The RMSE values have been determined for all measured positions in the principal plane at an illumination angle of 45°, for the soil and vegetation targets. Lower RMSE values indicate a smaller difference between the measured and the simulated reflectance and thus a closer approximation of the laboratory measurements by the SLC-model.



### **3 RESULTS AND DISCUSSION**

In this section the results of both the laboratory measurements and the simulations with the SLC-model are described. First, the laboratory measurements will be treated and second, the results of the simulations of the SLC-model, both at an illumination angle of 45°. Finally the results of the measurements and simulations at an illumination angle of 30° will be discussed. It is assumed that besides a shift of the hot-spot position and a reduction of the anisotropic reflectance behaviour (Kimes 1983), similar effects will be observed at an illumination angle of 30° and 45°. Therefore, for the difference in illumination angle, most attention will be paid to the difference in ANIX.

### 3.1 Laboratory measurements

In order to make sure that the measurements of a measurement sequence were not affected by changes of the vegetation, repetitive measurements were taken at nadir position. To be able to compare all measurements within a measurement sequence, it is important that the targets can be assumed to be constant. Strong irradiance of the laboratory light source could result in vegetation stress like wilting and dehydration, which alters the reflected signal and thereby the observed reflectance anisotropy (Sandmeier et al. 1998b). The results of the repetitive measurements are displayed in *Figure 16*. No clear differences between the repetitive measurements can be observed.

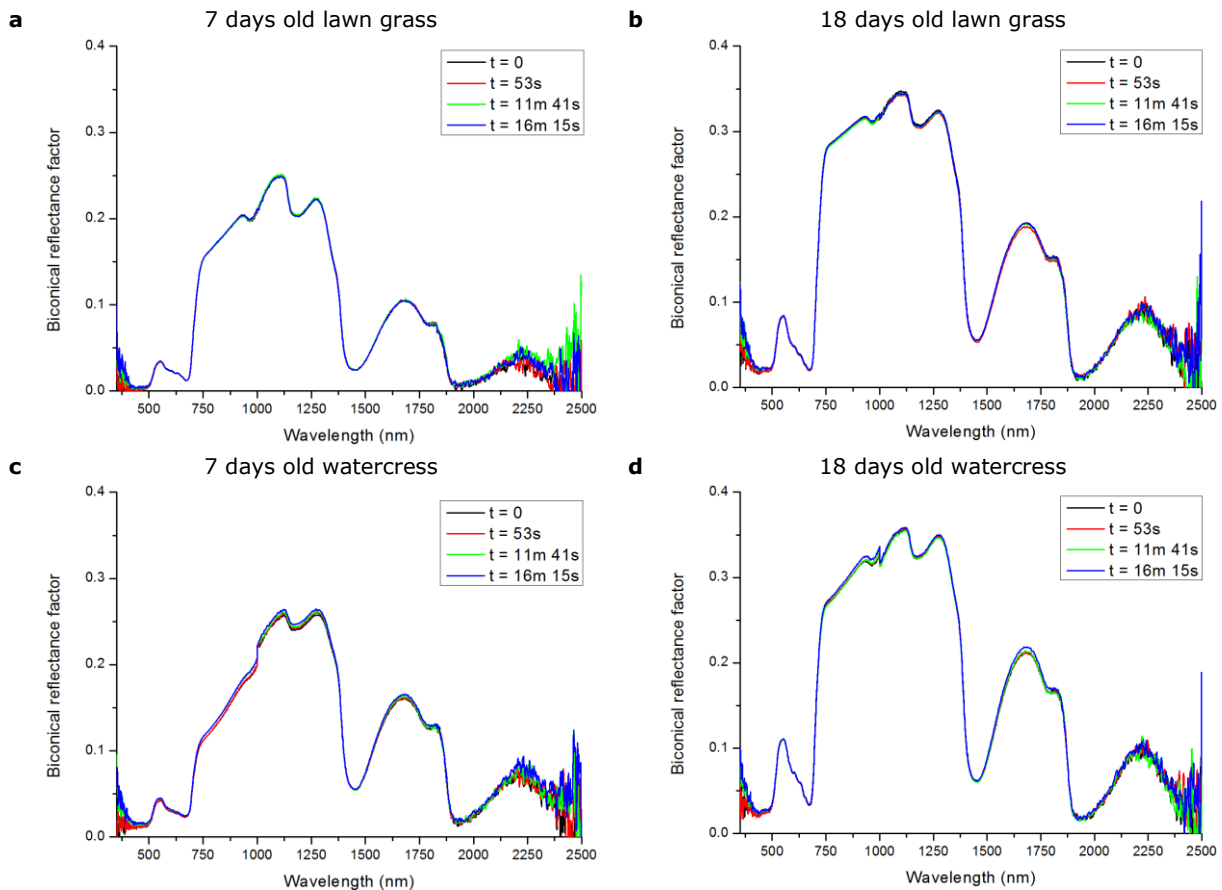


*Figure 16. Repetitive BCRF measurements taken at nadir position of a) 7 days old lawn grass and; b) 18 days old lawn grass; c) 7 days old watercress; d) 18 days old watercress. ‘t’ is the time of the start of the measurements.*

The average root mean squared (RMS) difference with the measurement at  $t = 0$  over the 500 – 1900 nm interval for the vegetation targets is given in *Table 11*. The low RMS differences indicate that there are only minor differences between the repetitive measurements. Therefore, it can be concluded that within the short acquisition time of the measurements there are no signs of dehydration and wilting of the vegetation, and thus, that all measurements within a measurement sequence are comparable.

*Table 11. RMS differences between the repetitive measurements at nadir position of the lawn grass and watercress targets over the 500 – 1900 nm interval.*

Vegetation type	Measurement comparison		
	1 – 2	1 – 3	1 – 4
7 days old lawn grass	0.00115	0.00160	0.00120
18 days old lawn grass	0.00286	0.00183	0.00165
7 days old watercress	0.00150	0.00343	0.00464
18 days old watercress	0.00110	0.00182	0.00380

### 3.1.1 Bare soil

The soil on which the vegetation targets were grown is measured at the same positions as the vegetation samples. In the backward scatter direction, the BCRFs increase with an increasing viewing zenith angle (*Figure 17a*). This effect is caused by the roughness of the soil. The laboratory lamp causes parts of the soil which are orientated towards the lamp to be illuminated and therefore there is an increase in the BCRF that is observed in the backward scatter direction. In the forward scatter direction, up to a VZA of 30°, there is a small decrease in BCRF. This is because at these positions, the less illuminated and shadowed parts of the soil are observed. At a VZA of 50° and 60° (*Figure 17b*) the BCRFs are higher compared to the BCRF observed at nadir position, which indicates that the bare soil also contains a specular reflectance component.

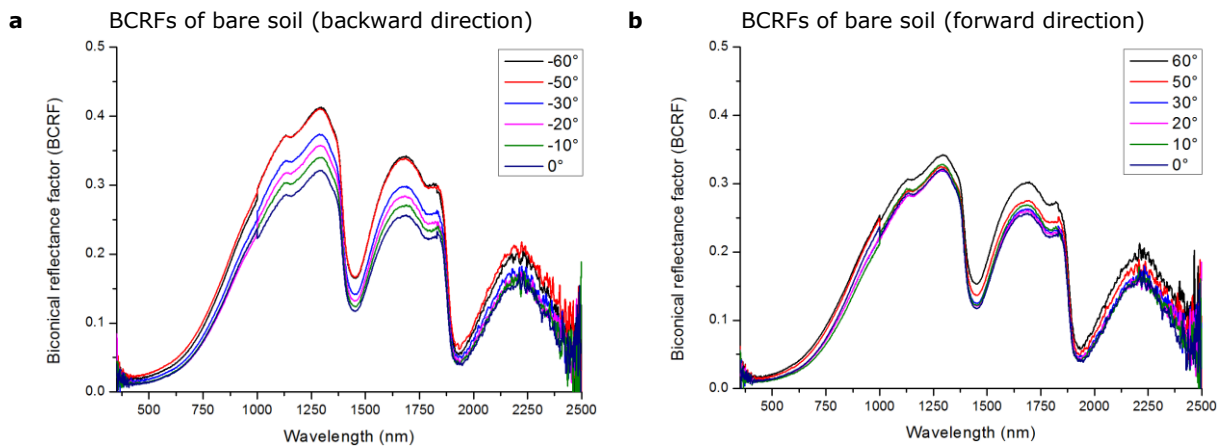


*Figure 17. BCRFs of bare soil observed at a VZA of 10°, 20°, 30°, 50° and 60° in the principal plane in a) the backward scatter direction; b) the forward scatter direction. In both a and b the BCRF observed at nadir position is displayed as a reference. ( $\vartheta_i = -45^\circ$ )*

*Figure 18a* shows how the BCRFs of the bare soil changes at different VZAs for five wavelengths between 550 nm and 1200 nm. The BCRFs are higher at longer wavelengths, which is caused by the typical higher reflectance of the soil at longer wavelengths. This does not give any information about the anisotropic reflectance effects of the bare soil. In order to get an insight in the reflectance anisotropy of the soil, the BCRFs of all measurement positions were normalized by the nadir observed BCRF, see *Figure 18b*. Here it becomes clear that the shorter wavelengths (550 nm, 670 nm and 730 nm) displayed more anisotropic behaviour compared to the longer wavelengths (900 nm and 1200 nm). *Figure 18b* shows a clear increase in ANIF around the hot-spot position and the lowest ANIFs are found in the forward scatter direction, up to 45°. At VZAs greater than 45°, the ANIF increases again, indicating a forward scattering component.

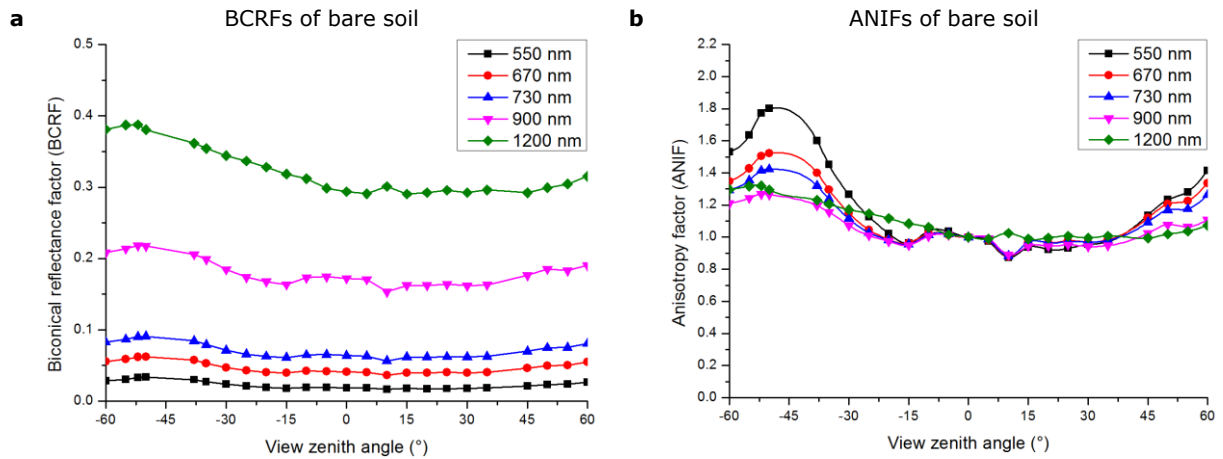


Figure 18. BCRFs of bare soil in the principal plane: **a)** observed at 550 nm, 670 nm, 730 nm, 900 nm and 1200 nm; **b)** the nadir normalized reflectance (ANIF) at 550 nm 670 nm, 730 nm, 900 nm and 1200 nm observed in the principal plane. The symbols represent the measurement positions and the lines represent interpolated data based on a spline. ( $\vartheta_i = -45^\circ$ )

The polar plots in *Figure 19a-f* give an insight in the anisotropic reflectance behaviour of the bare soil over the measured hemisphere between 550 and 1600 nm. The hot-spot is clearly visible at 550 nm (*Figure 19a* at  $\varphi = 180^\circ$  and  $\theta = 45^\circ$ ). At longer wavelengths (900 – 1600 nm) the hot-spot is less pronounced. Independent of the wavelength, the lowest BCRFs are found slightly in the forward scatter direction: the positions at which the spectrometer observed the highest proportion of the shaded parts of the soil. The highest BCRFs are found in the backward scatter direction, with a maximum around the hot-spot position: the position where the spectrometer only observes the illuminated parts of the soil. The reflectance anisotropy of a soil depends on its roughness at micro and at larger scales. The increased BCRFs in the backward scatter direction is most pronounced for rough soils at larger scales (Wang et al. 2012). Smoothness of the soil particles on a micro scale results in specular reflectance of the incoming radiance (Cierniewski and Verbrugghe 1997). A forward scattering component is particularly found in sandy soils, caused by the high proportion of specular reflectance due to the smooth surface of sand particles (Barducci et al. 2009). Soils with a relatively high organic matter content also have a higher proportion of specular reflectance compared to soils with a lower organic matter content (Mulders 1987) as cited in Cierniewski and Verbrugghe (1997). Possibly, a combination of the soils smoothness at micro scale and the high organic matter content (17%) of the measured soil resulted in the observed forward scattering reflectance.

Bare Soil

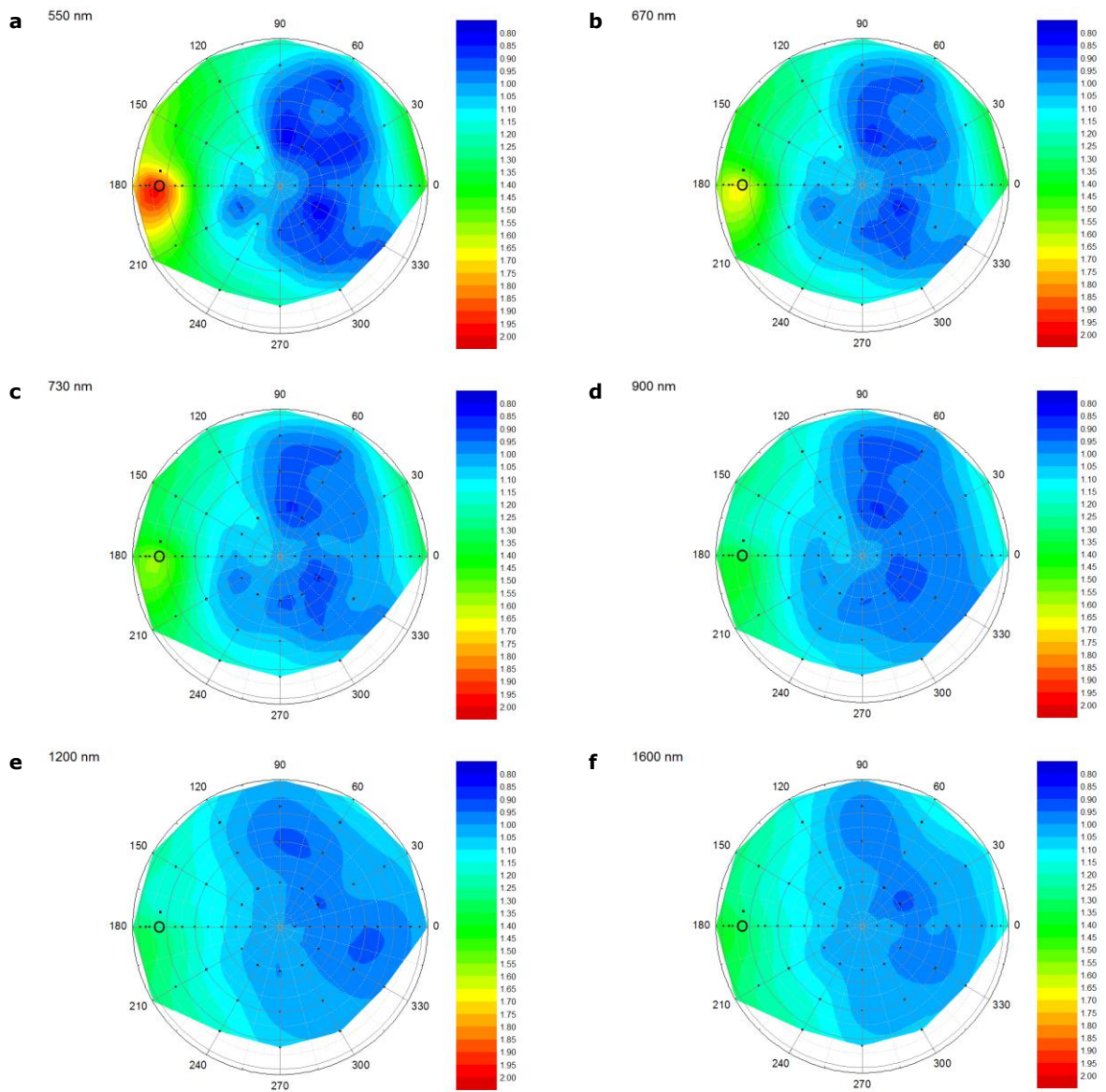
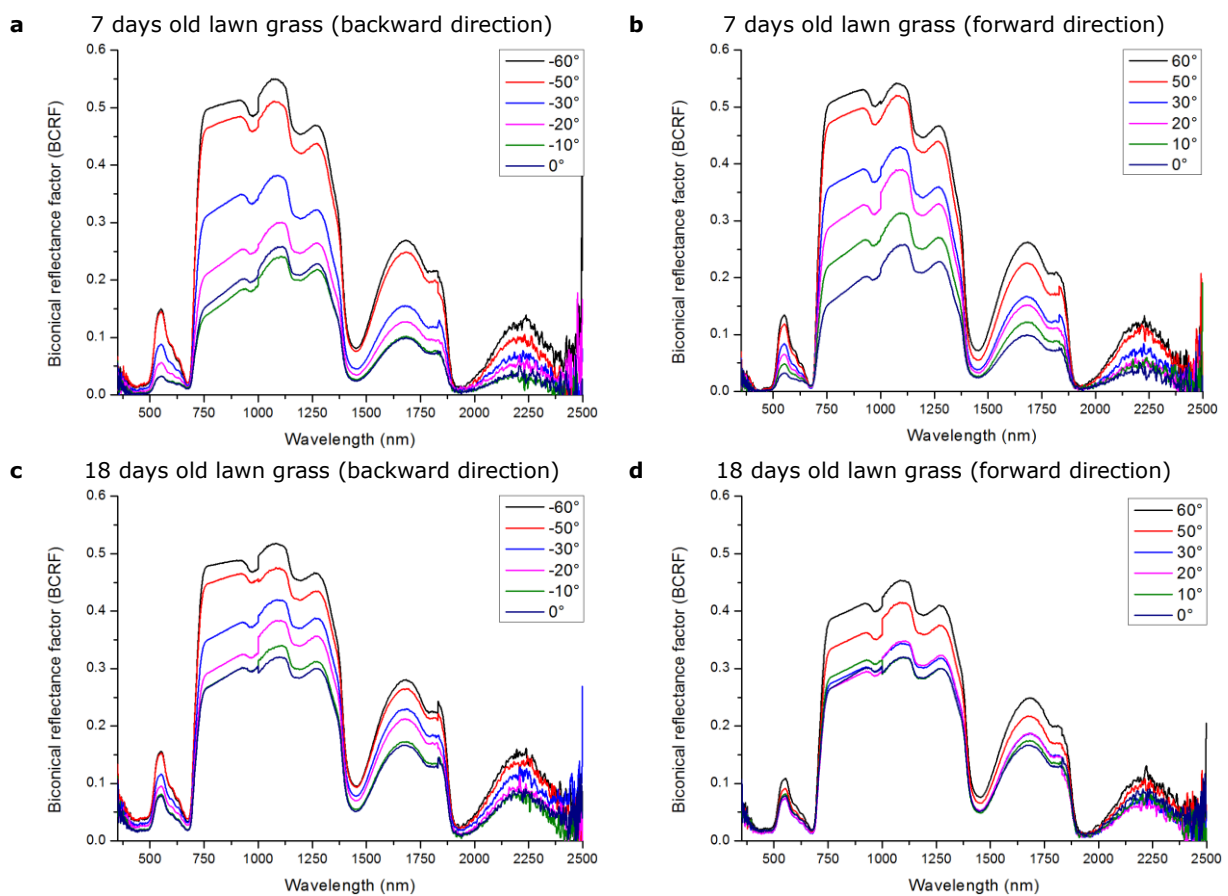


Figure 19. Interpolated polar plots of the observed ANIFs of bare soil at 550 nm, 670 nm, 730 nm, 900 nm, 1200 nm and 1600 nm. The black dots indicate the measurement positions and the circle indicate the hot-spot position.

### 3.1.2 Lawn grass

When observing from nadir position, the 18 days old lawn grass covered 71.74% of the surface and the young lawn grass only covered 28.52% (*Table 2*). The 18 days old lawn grass canopy consisted of more bent grass haulms and the 7 days old lawn grass consisted of more erect (vertical) grass haulms. The vegetation cover is of great importance when investigating the reflectance anisotropy, since there is a great contrast in color between the light vegetation and the dark underlying soil and a difference in observed proportion of vegetation and soil at different viewing positions. Because of the low vegetation cover, the influence of the underlying soil is greater for the 7 days old lawn grass, compared to the 18 days old lawn grass. When increasing the VZA, the proportion of vegetation that is observed by the spectrometer also increases and thereby the measured reflectance factor also increases. This effect occurs at the 7 and 18 days old lawn grass, *Figure 20a* and *Figure 20b*, and *Figure 20c* and *Figure 20d*, respectively, however it is most pronounced for the 7 days old lawn grass.



*Figure 20. BCRFs of watercress observed in the principal plane at a VZA of 10°, 20°, 30°, 50° and 60°. a) 7 days old lawn grass in the backward scatter direction; b) 7 days old lawn grass in the forward scatter direction; c) 18 days old lawn grass in the backward scatter direction; d) 18 days old lawn grass in the forward scatter direction. In all the graphs, a measurement from the nadir position (VZA = 0°) is included as a reference. ( $\vartheta_i = -45^\circ$ )*

The increase in BCRF at increasing VZAs becomes more clear when displaying the BCRFs over the principal plane (*Figure 21*). In the forward and backward scatter direction, an increased VZA led to an increase in BCRF, resulting in bowl-shaped BCRF plots. The bowl-shaped curve is more pronounced for the 7 days old lawn grass (*Figure 21a*) compared to the 18 days old lawn grass (*Figure 21b*), due to the differences in proportion of vegetation cover at nadir position and at off-nadir VZAs. The

minimum BCRF of the 7 days old lawn grass slightly in the backward scatter direction is probably caused by inhomogeneity of the vegetation cover. The bowl-shaped BCRF does not occur at 670 nm. At 670 nm, the BCRF decreases in the forward scatter direction. This is due to the fact that at 670 nm, both chlorophyll a and b absorb a great proportion of the incoming radiation (Lichtenthaler 1987). In the forward scatter direction, radiation has to travel the longest path through the canopy and is most likely to be absorbed. This results in darker shadows in the forward scatter direction, due to the lower proportion of transmittance, and therefore in lower observed BCRFs.

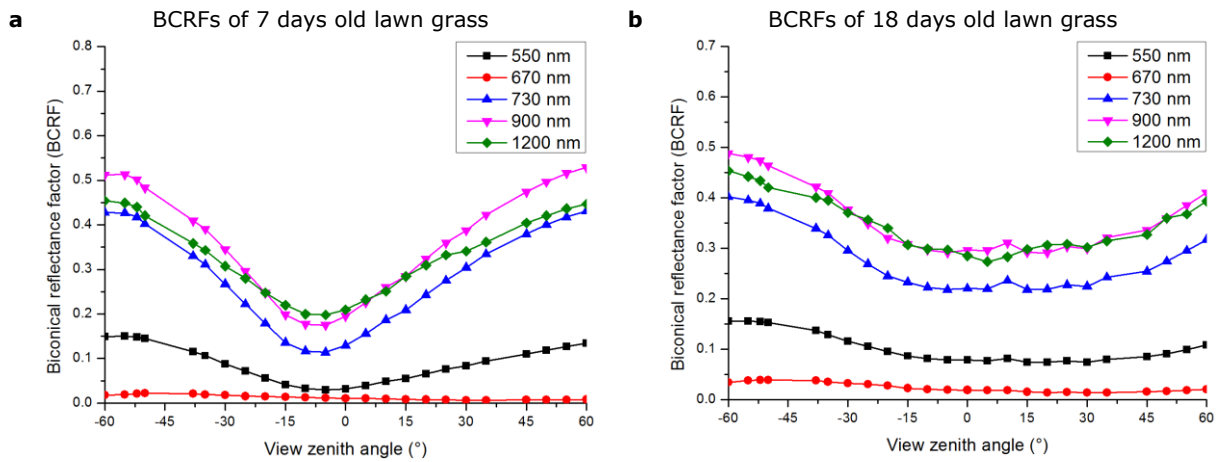


Figure 21. BCRFs of lawn grass observed over the principal plane at 550 nm, 670 nm, 730 nm, 900 nm and 1200 nm. **a)** 7 days old lawn grass; **b)** 18 days old lawn grass. The symbols represent the measurement positions and the lines represent interpolated data based on a spline. ( $\vartheta_i = -45^\circ$ )

The aforementioned effects become more clear when the off-nadir BCRFs are normalized by the nadir BCRF, see Figure 22a and Figure 22b. The decrease in BCRF at 670 nm in the forward scatter direction is now clearly observable. Less pronounced anisotropic effects occur in the NIR. This is due to the fact that in the NIR multiple scattering is dominant (Sandmeier et al. 1998a). Multiple scattering reduces the contrast between shadowed and illuminated parts of the canopy and thereby it diminishes anisotropic effects (Kimes 1983).

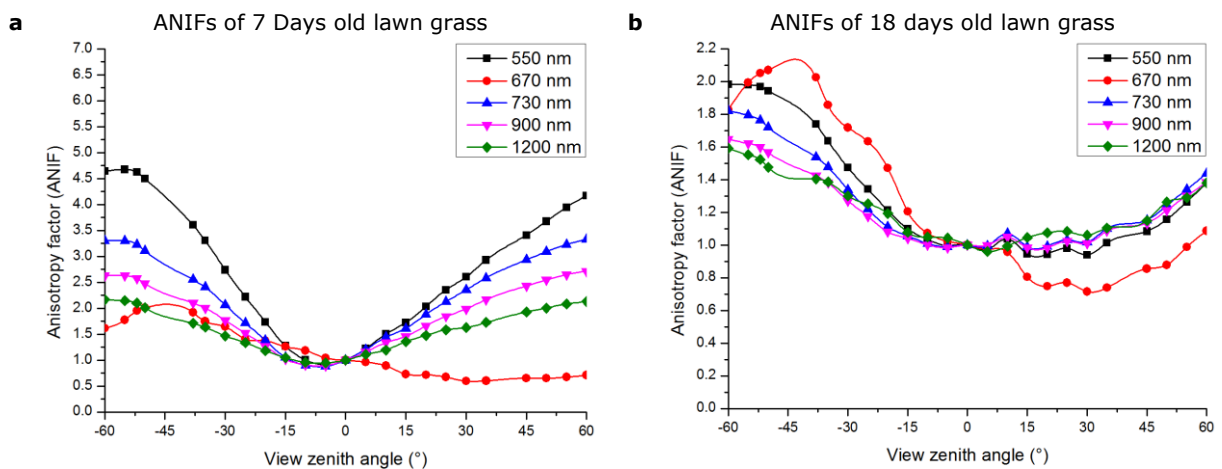


Figure 22. ANIFs of lawn grass observed over the principal plane at 550 nm, 670 nm, 730 nm, 900 nm and 1200 nm. **a)** 7 days old lawn grass; **b)** 18 days old lawn grass. The symbols represent the measurement positions and the lines represent interpolated data based on a spline. ( $\vartheta_i = -45^\circ$ )

The integrated polar plots in Figure 23a-f and Figure 24a-f give an insight in the anisotropic behaviour of 7 days old lawn grass and 18 days old lawn grass, respectively, over the measured hemisphere. Figure 23a shows the ANIFs of 7 days old lawn grass at 550 nm. There is a clear increased ANIF around the hot-spot position ( $\varphi = 180^\circ$  and  $\theta = 45^\circ$ ). The lowest for all depicted wavelengths (except 670 nm) ANIFs are found around the nadir position. Independently of the azimuth angle, the ANIF increased when the VZA increased. At 670 nm (Figure 23b) the chlorophyll absorption features are clearly visible, which resulted in a decreased ANIF in all directions except the backward scattering direction in the principal plane. The highest ANIF at 670 nm was found around the hot-spot position. Due to lower transmittance at longer wavelengths, the anisotropic effects decreased in the NIR (Figure 23c-f). The typical pattern of the lowest ANIF at the nadir position and the increasing ANIF at increasing off-nadir VZAs observed at 550 nm also occurs in the NIR region.

7 days old lawn grass

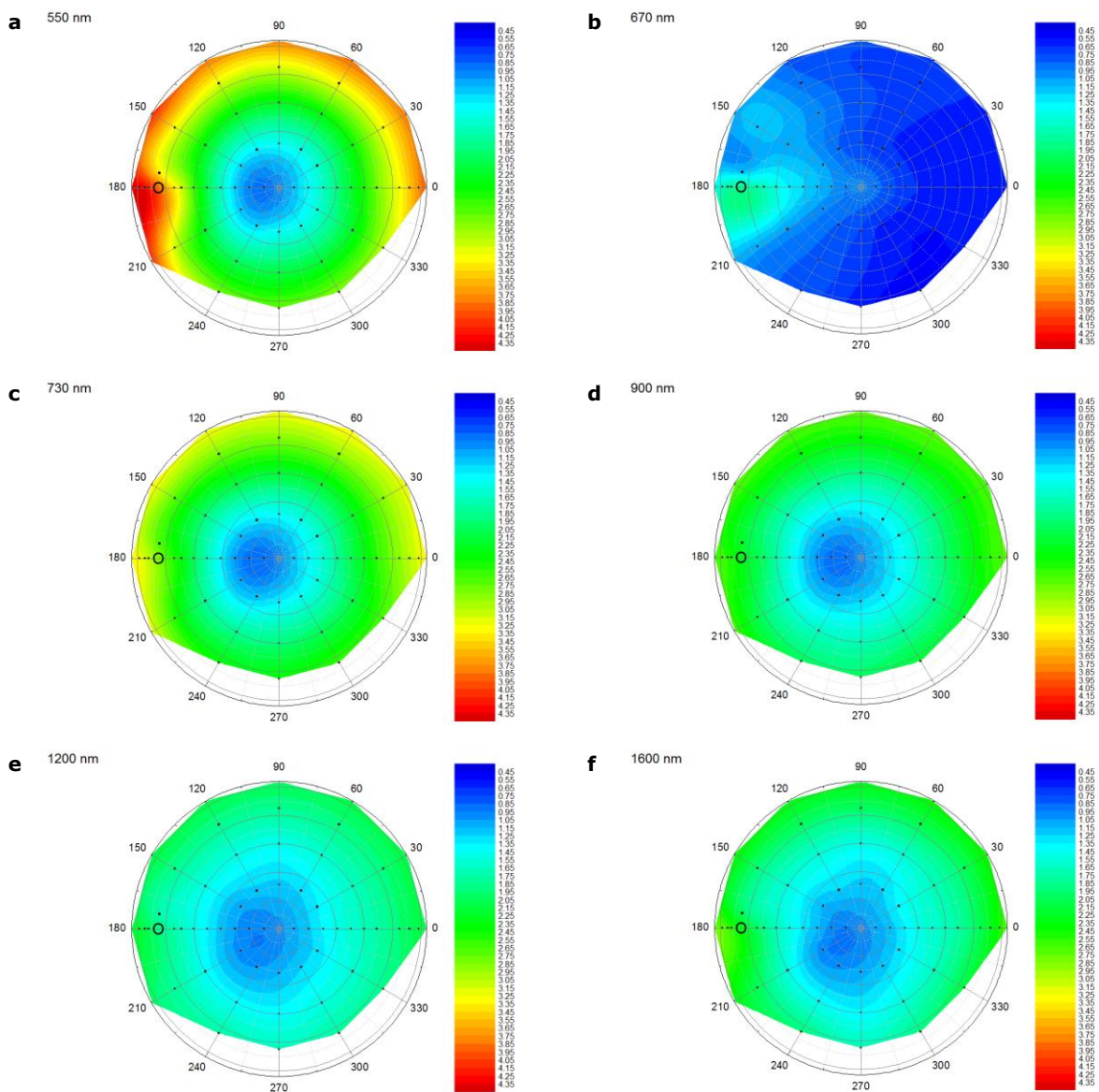


Figure 23. Interpolated polar plots of the observed ANIFs of 7 days old lawn grass at 550 nm, 670 nm, 730 nm, 900 nm, 1200 nm and 1600 nm. The black dots indicate the measurement positions and the circle indicates the hot-spot position.

The anisotropic reflectance effects of the 18 days old lawn grass over the measured hemisphere are shown in *Figure 24a-f*. The effects are less pronounced compared to the 7 days old lawn grass. At 550 nm the highest ANIFs are found in the backward direction (*Figure 24a*), however, not exactly around the hot-spot position. The lowest ANIFs around  $\varphi = 60^\circ$  and  $\theta = 30^\circ$  are likely to be caused by inhomogeneity of the target: probably at this position, the sensor was observing a gap or stronger shaded part of the canopy. At 670 nm (*Figure 24b*) the effects of the chlorophyll absorption did not result in decreased ANIFs in all azimuth directions as observed at the 7 days old lawn grass (*Figure 23b*). This is because there is a smaller difference in observed proportion of underlying soil visible at nadir position and at off-nadir positions for the 18 days old lawn grass, which results in smaller differences between the nadir observed BCRF and BCRFs observed at off-nadir VZAs and therefore in less extreme ANIFs. There is, however, a more pronounced dark-spot present at the 18 days old lawn grass at 670 nm. Due to the higher canopy cover of the 18 days old lawn grass, the minimum ANIF is shifted in the forward scatter direction, compared to the minimum ANIF at nadir position at the 7 days old lawn grass. Just like at the 7 days old lawn grass, the anisotropic reflectance effects were most pronounced in the visible wavelengths and decreased at increasing wavelengths.

The results of the measurements of the 18 days old lawn grass are more similar to the results of the measurements of Sandmeier et al. (1998a), compared to the 7 days old lawn grass. This is because the measurements of Sandmeier et al. (1998a) were performed on a lawn grass canopy, which completely covered the surface. The complete vegetation cover had as a result that there was no influence of the underlying soil. This is also the case for the 18 days old lawn grass. Due to the higher proportion of vegetation cover, there is less influence of the soil on the observed reflectance anisotropy. Therefore, the 18 days old lawn grass better approximates the anisotropic reflectance behaviour of lawn grass, because the observed reflectance anisotropy of the 7 days old lawn grass is strongly affected by the underlying soil.

18 days old lawn grass

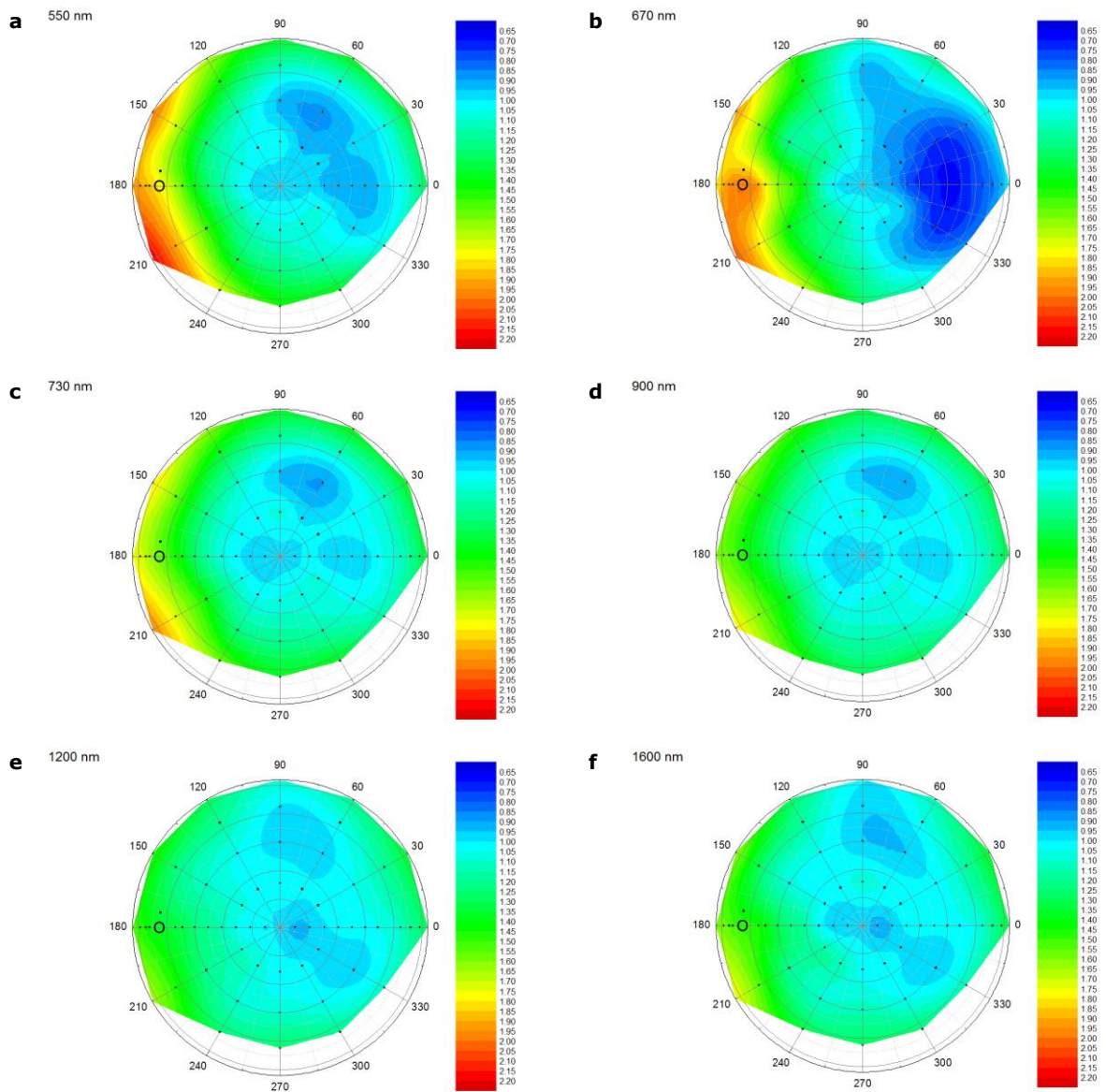


Figure 24. Interpolated polar plots of the observed ANIFs of 18 days old lawn grass at 550 nm, 670 nm, 730 nm, 900 nm, 1200 nm and 1600 nm. The black dots indicate the measurement positions and the circle indicates the hot-spot position.

### 3.1.3 Watercress

The young watercress covered 17.45% of the surface and the old watercress covered 42.75% (see Table 2). Due to the brighter colour of the watercress compared to the underlying soil, the reflectance factors of the 7 days old watercress were lower (Figure 25a and Figure 25b), compared to the 18 days old watercress (Figure 25c and Figure 25d). Both the 7 days and 18 days old watercress showed an increase in reflectance factor in the backward scatter direction (Figure 25a and Figure 25c). The lowest BCRFs were found in the forward direction, close to the nadir position. This is caused by the less-illuminated parts of the vegetation and soil, and the shadow caused by the vegetation and soil particles that are observed at these positions. At VZAs  $> 30^\circ$  the reflectance was higher compared to the nadir reflectance, indicating a specular scattering component (Figure 25c and Figure 25d).

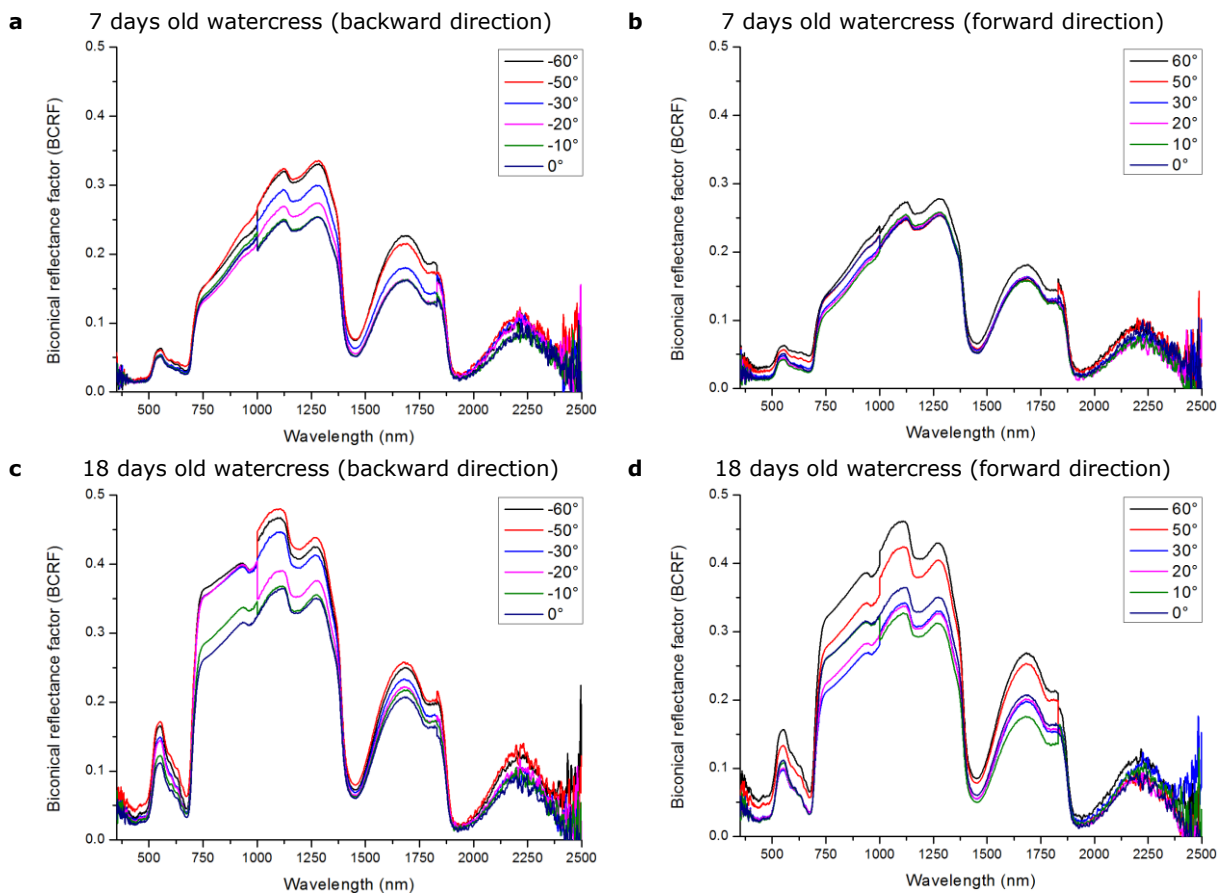


Figure 25. BCRFs of watercress observed in the principal plane at a VZA of  $10^\circ$ ,  $20^\circ$ ,  $30^\circ$ ,  $50^\circ$  and  $60^\circ$  of **a)** 7 days old watercress in the backward scatter direction; **b)** 7 days old watercress in the forward scatter direction; **c)** 18 days old watercress in the backward scatter direction; **d)** 18 days old watercress in the forward scatter direction. In all the graphs, a measurement from the nadir position (VZA =  $0^\circ$ ) is included as a reference. ( $\vartheta_i = -45^\circ$ )

Figure 26 shows the BCRF observations over the principal plane observed at five different wavelengths. An increase in the VZA in the backward scatter direction resulted in a small increase in the BCRF. In the forward scatter direction, at a VZA  $> 30^\circ$ , the BCRFs also increased with an increasing VZA. This results in a bowl-shape BCRF signature for both the 7 days and 18 days old watercress (see Figure 26a and Figure 26b, respectively). Close to the hot-spot position, in the forward scatter direction, the lowest BCRFs are found. Overall, the BCRFs of the 7 days old watercress are lower

compared to the 18 days old watercress, due to the lower percentage of vegetation cover of the 7 days old watercress, which results in a smaller proportion of dark underlying soil that is observed by the spectrometer.

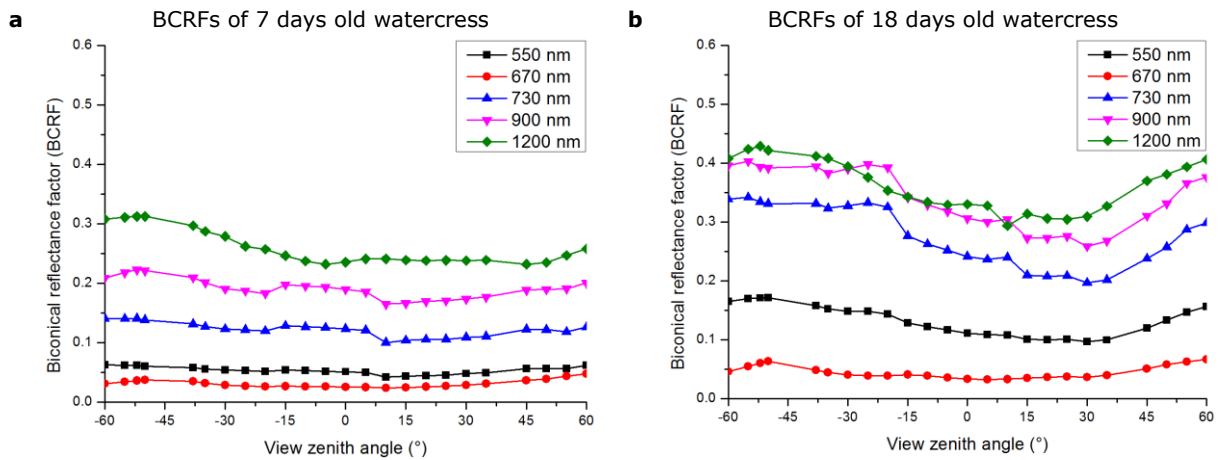


Figure 26. BCRFs of watercress observed in the principal plane at 550 nm, 670 nm, 730 nm, 900 nm and 1200 nm observed at different VZAs of **a)** 7 days old watercress; **b)** 18 days old watercress. The symbols represent the measurement positions and the lines represent interpolated data based on a spline. ( $\vartheta_i = -45^\circ$ )

Normalizing the off-nadir BCRFs by the nadir BCRF gives a more clear insight in the anisotropic behaviour of the watercress (Figure 27). At 670 nm the anisotropic effects were most pronounced, resulting in ANIFs around 1.5 and 1.9 close to the hot-spot and around 1.9 and 2.0 in the forward scatter direction for 7 days old and 18 days old watercress, respectively, at 670 nm. The other displayed wavelengths display less pronounced reflectance anisotropy, however bowl-shaped pattern can be distinguished, indicating both a forward and backward scattering component in the watercress targets.

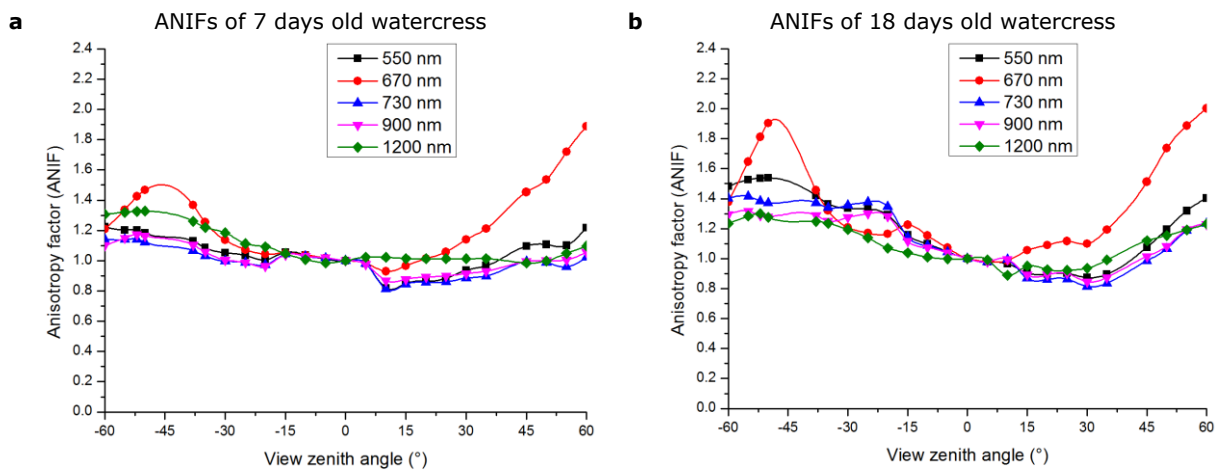
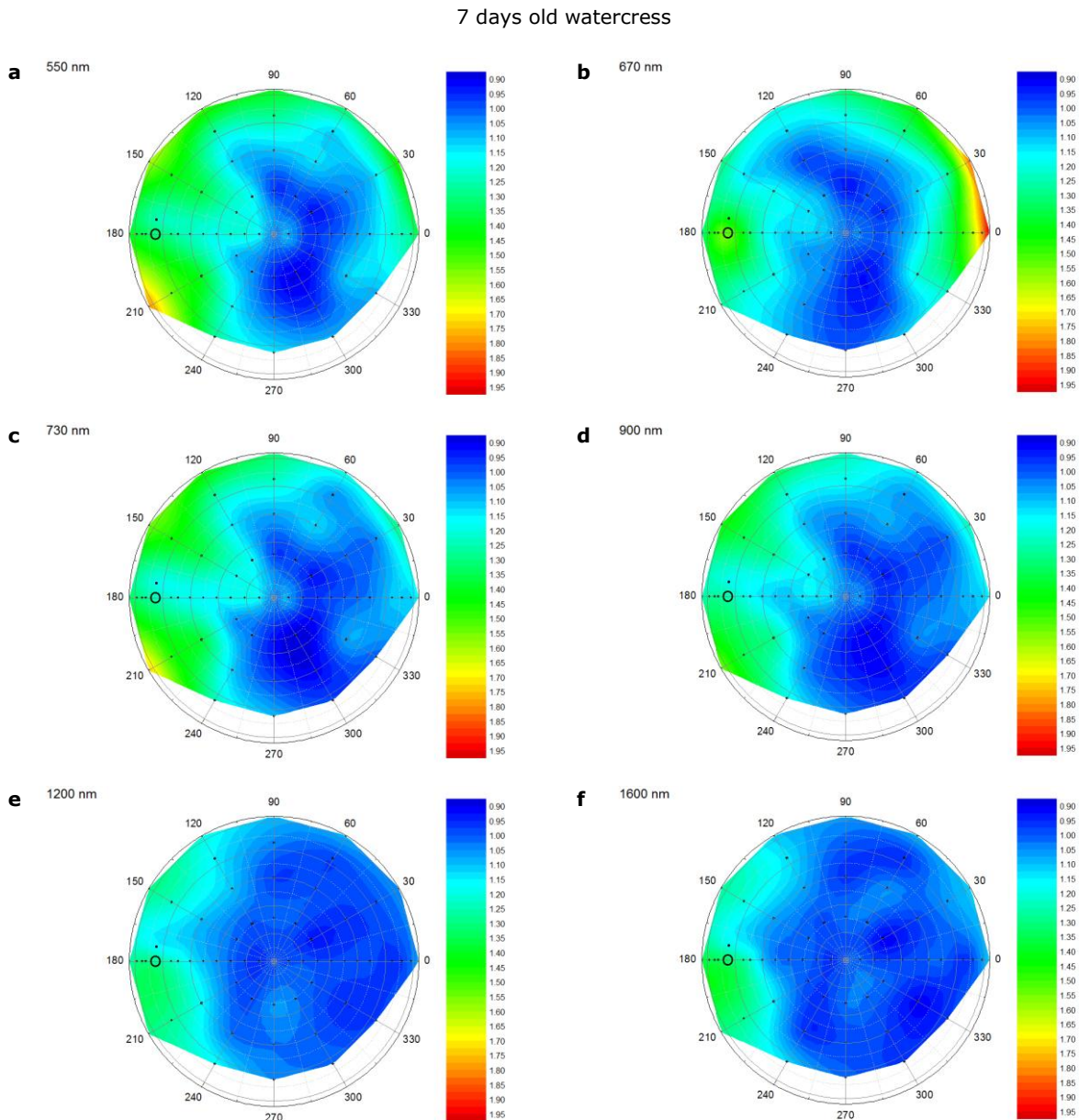


Figure 27. ANIFs of watercress observed in the principal plane at 550 nm, 670 nm, 730 nm, 900 nm and 1200 nm at different VZAs of **a)** 7 days old watercress; **b)** 18 days old watercress. The symbols represent the measurement positions and the lines represent interpolated data based on a spline. ( $\vartheta_i = -45^\circ$ )

The polar plots based on the ANIFs of the 7 days old watercress indicate a hot-spot in the backward scatter direction (*Figure 28a-f*). At 670 nm, 1200 nm and 1600 nm, the highest ANIFs are found around the hot-spot position. At 550 nm and 730 nm, the greatest ANIFs are found in the backward scatter direction, although they are not exactly around the hot-spot position. The lowest ANIFs are found in the forward scatter direction close to the nadir position. In the visible part, the anisotropic reflectance effects were most pronounced. In the NIR, the anisotropic reflectance effects are less pronounced.



*Figure 28. Interpolated polar plots of the observed ANIFs of 7 days old watercress at 550 nm, 670 nm, 730 nm, 900 nm, 1200 nm and 1600 nm. The black dots indicate the measurement positions and the circle indicates the hot-spot position*

For the 18 days old watercress (*Figure 29*), similar patterns are found. The highest ANIFs are found in the backward scatter direction, around the hot-spot position. The most pronounced hot-spot occurs at 670 nm (*Figure 29b*). In the visible part, the anisotropic effects were most pronounced and in the NIR the anisotropic effect diminished. At all wavelengths, the lowest ANIFs are found close to nadir in the forward scatter direction. This was also observed by Sandmeier et al. (1998a). There appears to be a second dark-spot around  $\varphi = 60^\circ$  and  $\theta = 30^\circ - 60^\circ$ . This dark spot is probably caused by inhomogeneity of the watercress target. At these positions, the spectrometer probably observed a greater proportion of soil and a smaller proportion of watercress leaves, resulting in a low ANIF. The observed forward scattering is typical for vegetation with planophile leaves (Grant 1987).

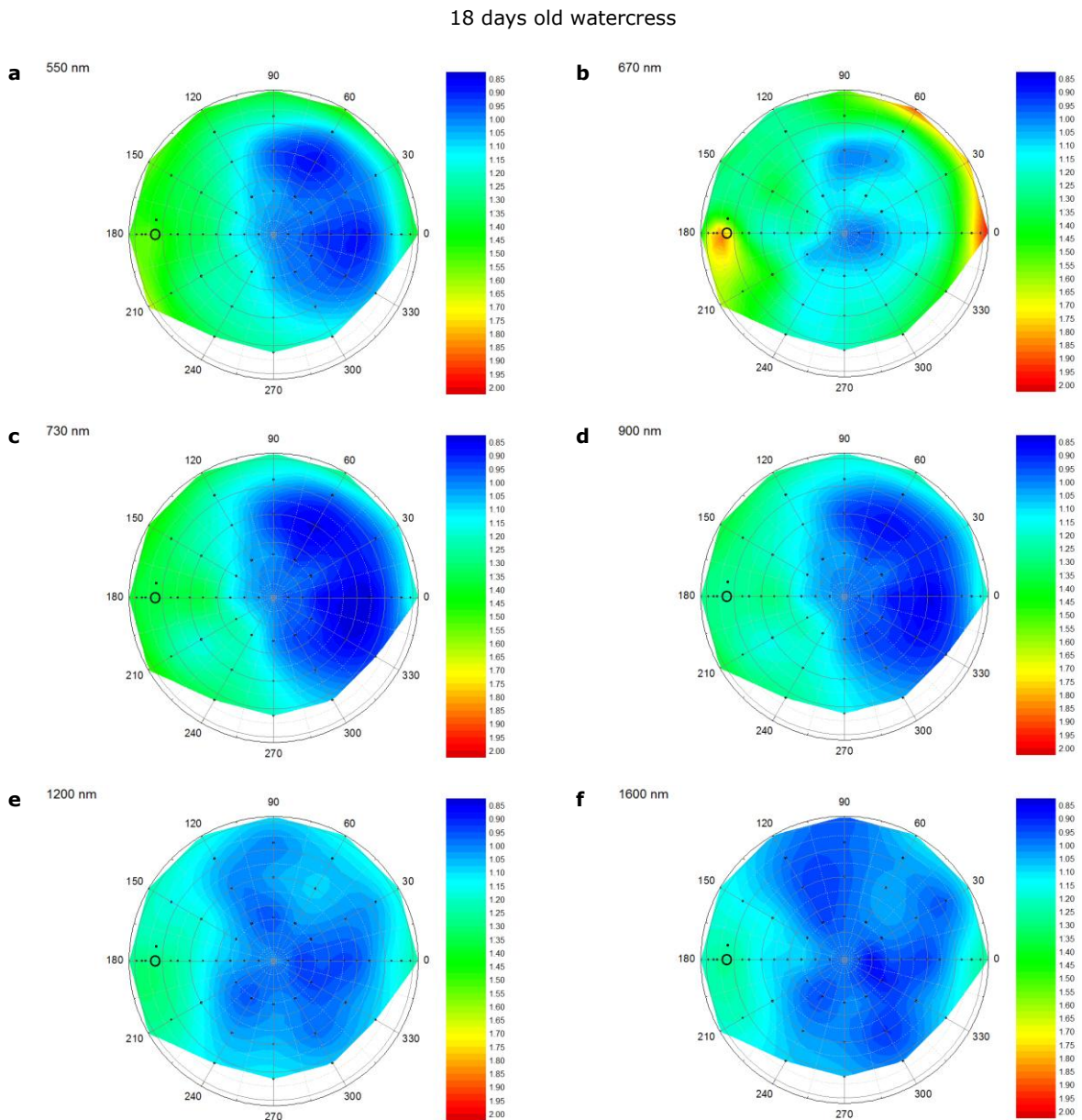


*Figure 29. Interpolated polar plots of the observed ANIFs of 18 days old watercress at 550 nm, 670 nm, 730 nm, 900 nm, 1200 nm and 1600 nm. The black dots indicate the measurement positions and the circle indicates the hot-spot position.*

### **3.2 SLC simulations**

This section describes the simulations of the laboratory measurements, which were performed using the SLC-model. The parameters, which are used as an input for the simulations can be found in *Table 9*. First, the simulation of the bare soil is described and second, the simulations of the lawn grass and finally the simulations of the watercress. The simulations will be compared to the laboratory measurements at three different positions: nadir, 60° backward scatter direction and 60° in the forward scatter direction. This allows for the investigation on the ability of the SLC-model to simulate the measured reflectance, as well as the anisotropic reflectance behaviour.

### 3.2.1 Bare soil

In *Figure 30* the bare soil simulations, created with the SLC-model are shown for the nadir position,  $60^\circ$  in the backward scatter direction and  $60^\circ$  in the forward direction, together with the measured spectral signatures at these positions. Since the measured soil signature at nadir position was used as the input data for the simulations, there is no noticeable difference between the measured and the simulated signature (*Figure 30*). At a VZA of  $60^\circ$  in the backward scatter direction, the SLC-model overestimated the reflectance (*Figure 30b*), while at a VZA of  $60^\circ$  in the forward direction, the SLC-model underestimated the reflectance (*Figure 30c*).

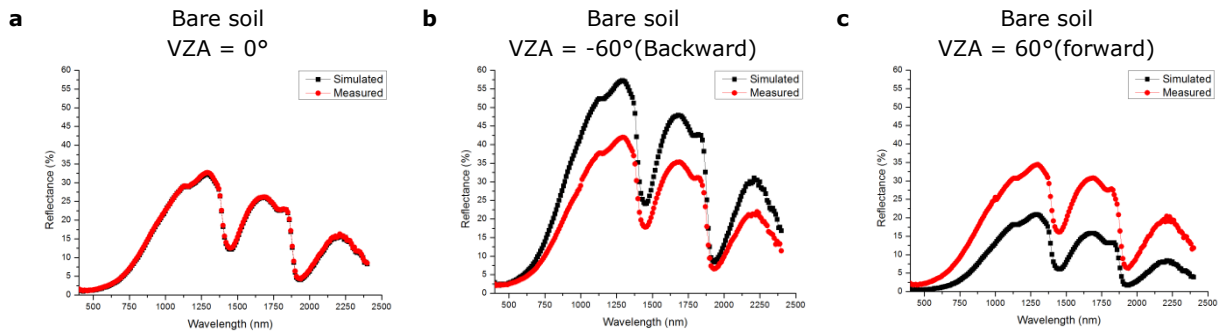


*Figure 30. Simulated (black) and measured (red) reflectance of bare soil: a) where VZA = 0°; b) where VZA = -60° (backward scatter direction); c) VZA = 60° (forward scatter direction). ( $\vartheta_i = -45^\circ$ )*

*Figure 31* shows the ANIFs of bare soil simulations over the principal plane. For all wavelengths, in the backward scatter direction, with an increasing VZA, the ANIF increased as well, while the ANIFs decreased at an increasing VZA in the forward direction. At 550 nm this effect seems to be the most pronounced, because at 550 nm the highest and lowest ANIFs are found in the backward and forward scatter direction, respectively (*Figure 31b*). With an increasing wavelength, the anisotropic effects diminished: at 1200 nm the lowest ANIFs are found in the backward scatter direction and the highest ANIFs in the forward scatter direction (*Figure 31b*).

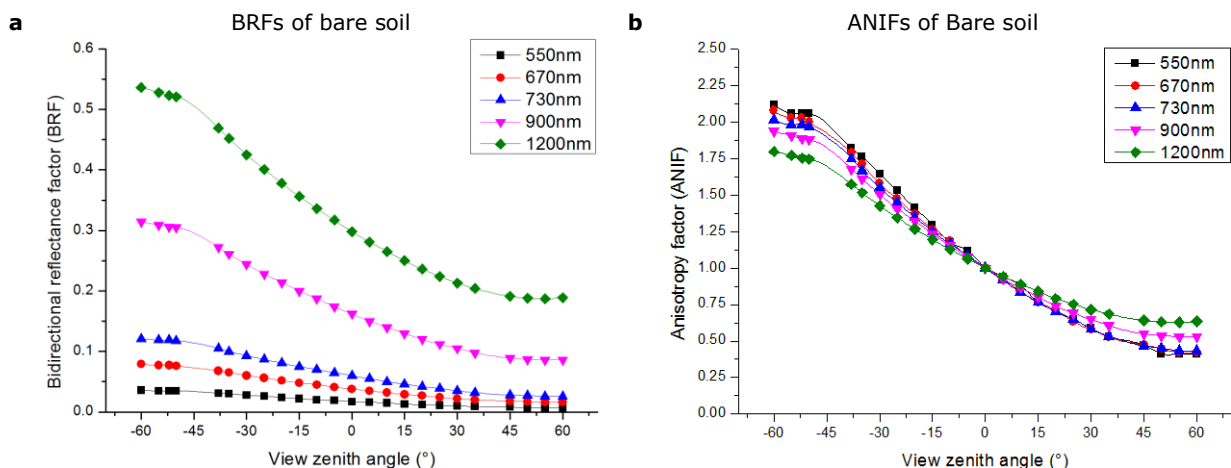


*Figure 31. Simulated BRFs and ANIFs of bare soil over the principal plane at 550 nm, 670 nm, 730 nm, 900 nm and 1200 nm. a) the BRFs; b) the ANIFs. The symbols represent the BRFs and ANIFs based on the simulations and the lines represent interpolated data based on a spline. ( $\vartheta_i = -45^\circ$ )*

Compared to the laboratory measurements, the SLC-model simulation produced azimuthally symmetrical polar plots. The highest ANIFs are found in the backward scatter direction. For all

wavelengths, which are displayed in *Figure 32*, the ANIF increased in the backward scatter direction and decreased in the forward scatter direction, where the greatest difference in ANIF are found at shorter wavelengths (*Figure 32a-c*). In the NIR, the differences between minimum and maximum ANIF decreased (*Figure 32d-f*). The used parameter settings, which were derived from a ploughed soil (Pinty et al. 1989), simulate a soil that exhibits strong backscattering behaviour and does not have a specular component. The bare soil that was measured in the laboratory does display a proportion of forward scattering. The simulated soil shows clearly pronounced backward scattering behaviour; however, there is no pronounced hot-spot present. This is caused by the parameter settings of the simulations, which result in a very wide and faint hot-spot that is difficult to recognize as a hot-spot (Verhoef and Bach 2007).

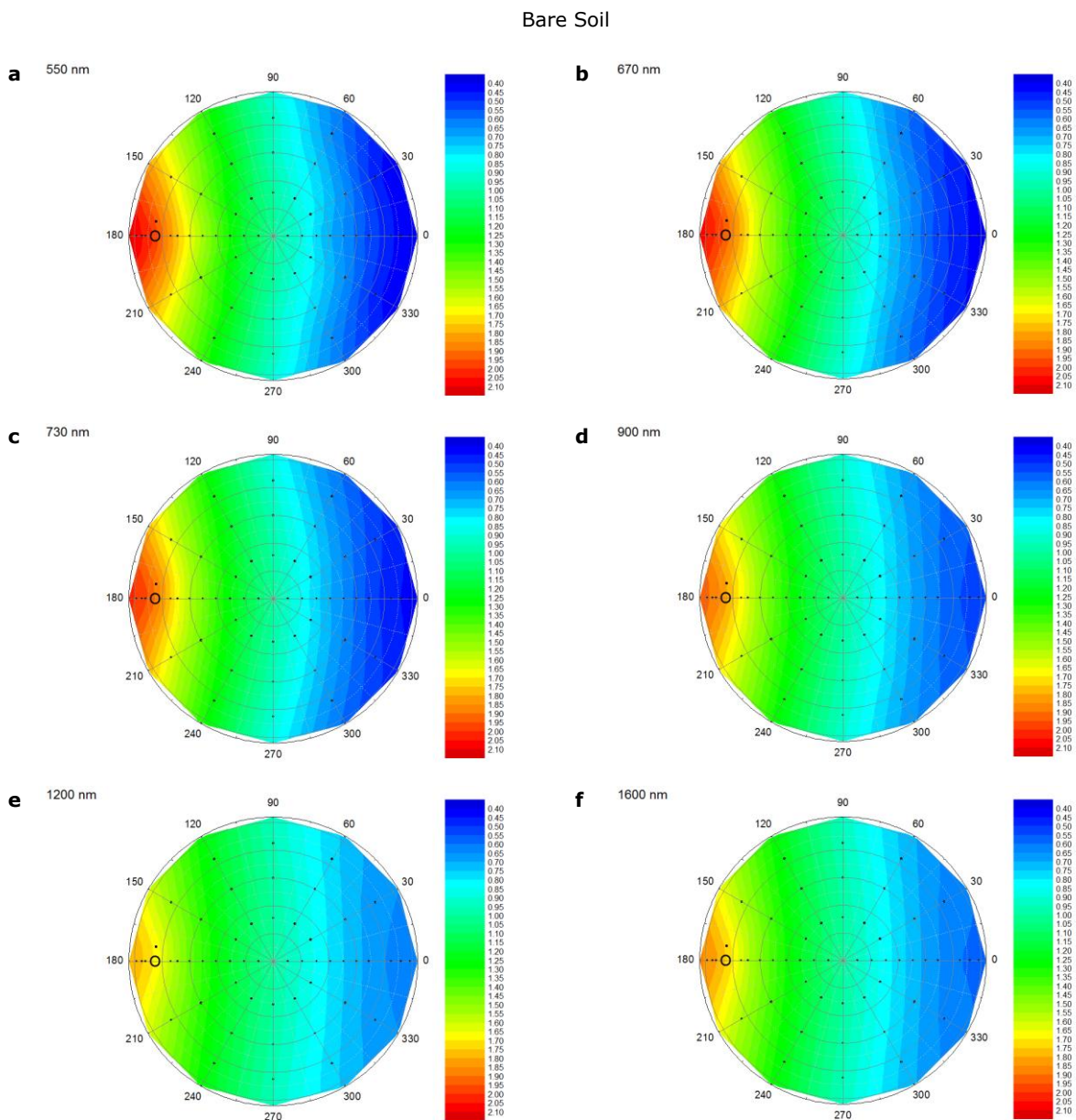


*Figure 32. Interpolated polar plots of the ANIFs of bare soil simulated by the SLC-model at 550 nm, 670 nm, 730 nm, 900 nm, 1200 nm and 1600 nm. The black dots indicate the measurement positions and the circle indicates the hot-spot position.*

### 3.2.2 7 Days old lawn grass

In *Figure 33* the measured and simulated spectral signatures of 7 days old lawn grass are displayed for a VZA at nadir position and a VZA of 60° in both the backward (*Figure 33b*) and forward (*Figure 33c*) direction. The pronounced peak in the green part of the spectrum (around 550 nm) which was measured by the spectrometer in the laboratory is not present at the simulations of the SLC-model. The simulated position of the red-edge (around 730 nm) occurs at the same regions as measured by the spectrometer. However, the position where the red-edge ends seems to be underestimated by the SLC-model. At nadir position, the SLC-model overestimated the laboratory measurements from 1100 nm to 2400 nm. At a VZA of 60° in both the forward and backward direction, the simulations seem similar to the laboratory measurements in this region.

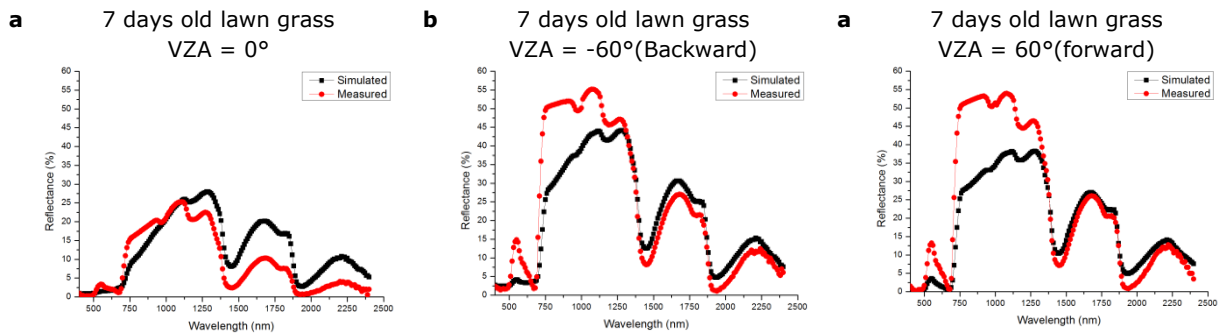


*Figure 33. Simulated (black) and measured (red) reflectance of 7 days old lawn grass: a) VZA = 0°; b) VZA = -60° (backward scatter direction); c) VZA = 60° (forward scatter direction). ( $\vartheta_i = -45^\circ$ )*

*Figure 34a* shows the BRFs of the 7 days old lawn grass simulation over the principal plane. All the wavelengths (except 670 nm) showed bowl-shape anisotropic reflectance effects. The reflectance anisotropy of the simulations is similar to the measured effects, although of a different magnitude (*Figure 22a*). The decrease of the ANIF in the forward scatter direction at 670 nm, simulated by the SLC-model, also occurred at the laboratory measurements.

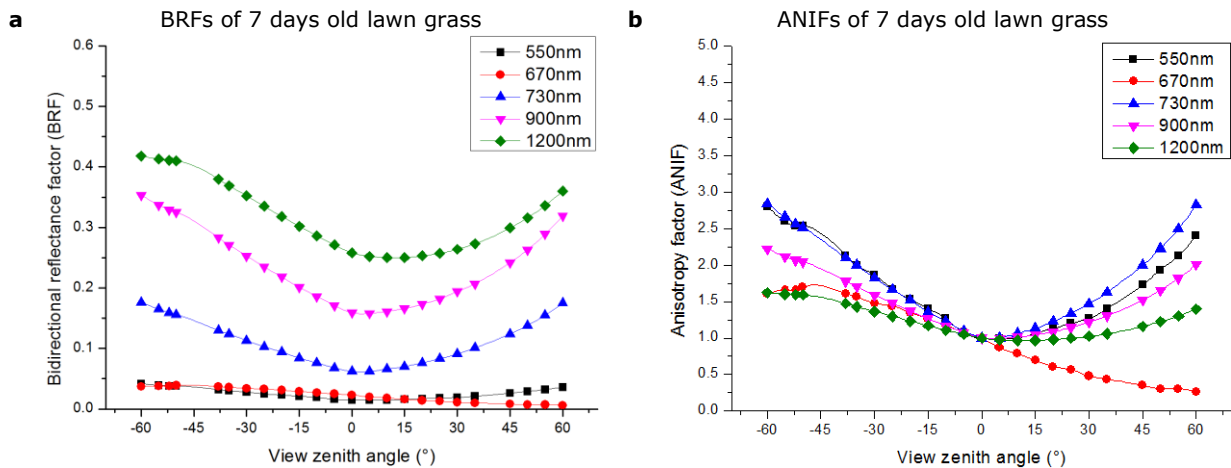


*Figure 34. Simulated BRFs and ANIFs of 7 days old lawn grass over the principal plane at 550 nm, 670 nm, 730 nm, 900 nm and 1200 nm. a) the BRFs; b) the ANIFs. The symbols represent BRFs and ANIFs based on the simulations and the lines represent interpolated data based on a spline. ( $\vartheta_i = -45^\circ$ )*

For all depicted wavelengths, there is no clear hot-spot present, which is likely the result of the parameter settings for the simulations: the size of the hot-spot is narrow due to the narrow leaves of

the lawn grass (Verhoef and Bach 2007). The simulations are most likely not close enough to the hot-spot position in order to capture the hot-spot effect. *Figure 35* displays the results of the SLC-model simulations over the measured hemisphere.

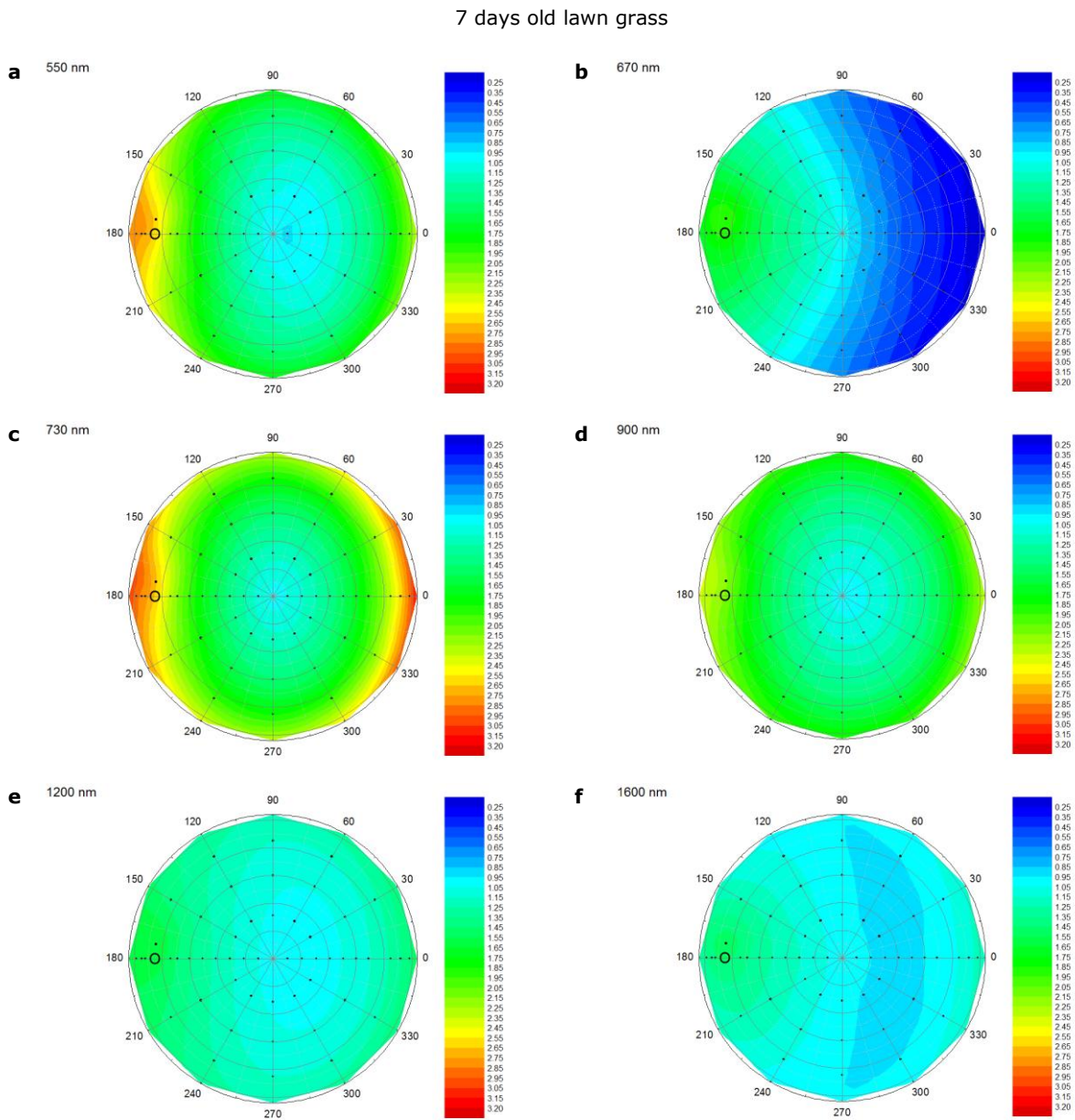


*Figure 35. Interpolated polar plots of the ANIFs of 7 days old lawn grass simulated by the SLC-model at 550 nm, 670 nm, 730 nm, 900 nm, 1200 nm and 1600 nm. The black dots indicate the measurement positions and the circle indicates the hot-spot position.*

The results show similar anisotropic reflectance effects as observed in the laboratory (*Figure 23*). The highest ANIFs are found in the backward scatter direction and the lowest ANIFs are found near nadir position, slightly in the forward direction, except at 670 nm. When the VZA increased, the ANIF also increased, for all depicted wavelengths except 670 nm. At 670 nm (*Figure 35b*) there was a decrease in ANIF in the forward scatter direction. The greatest anisotropic effects occurred at the visible wavelengths. In the NIR, the anisotropic effect diminished.

### 3.2.3 18 Days old lawn grass

Figure 36 displays the reflectance as measured in the laboratory and simulated by the SLC-model at VZA = 0°, VZA = -60° and VZA = 60°. The model was not able to simulate the measured peak at the green wavelength. Overall, the SLC-model simulations seem to underestimate the laboratory measurements. The (visually) closest match between the laboratory measurements and the SLC-model simulations appears to be at a VZA of 60° in the forward direction (Figure 36c).

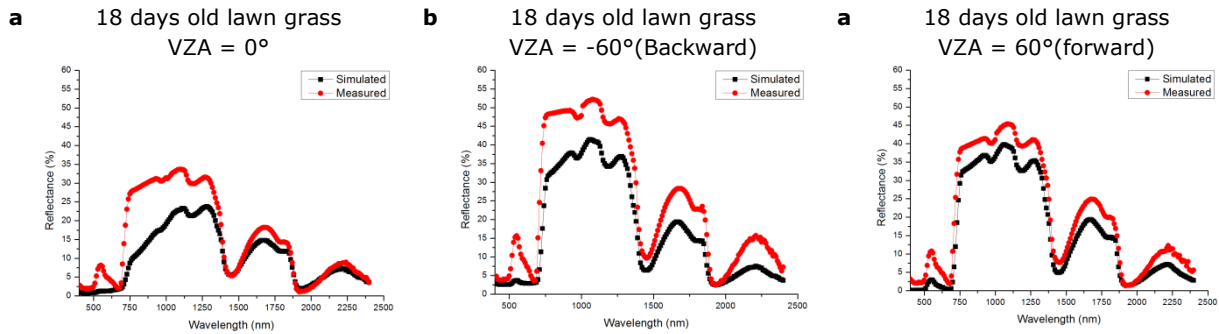


Figure 36. Simulated (black) and measured (red) reflectance of 18 days old lawn grass: **a)** VZA = 0°; **b)** VZA = -60° (backward scatter direction); **c)** VZA = 60° (forward scatter direction). ( $\vartheta_i = -45^\circ$ )

Plotting the ANIFs over the principal plane resulted in a bowl-shaped BRF graph (Figure 37b) for all depicted wavelengths, except 670 nm. Here, the ANIFs decreased when the VZA increased in the forward scatter direction. This effect was also found at the laboratory measurements (Figure 22b).

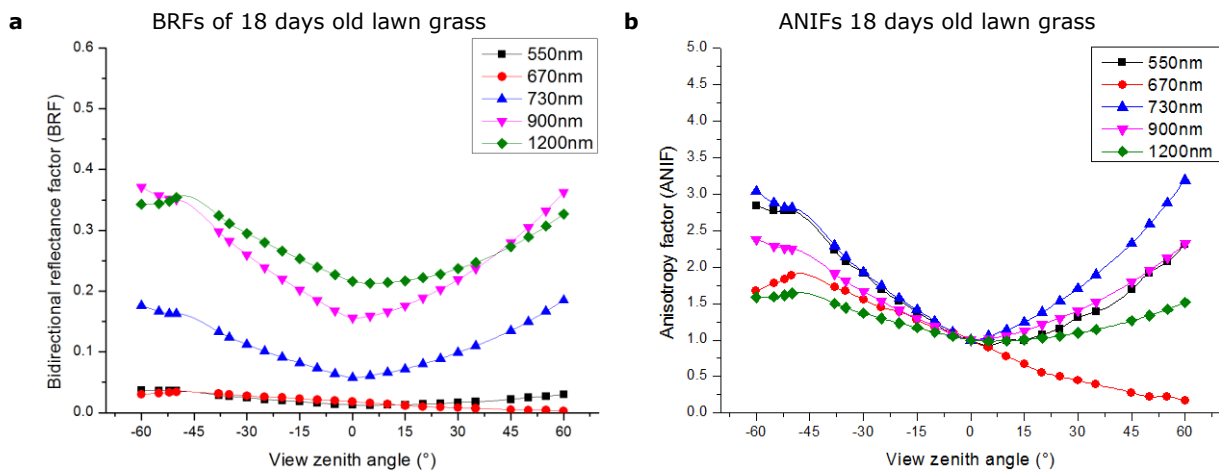


Figure 37. Simulated BRFs and ANIFs of 18 days old lawn grass over the principal plane at 550 nm, 670 nm, 730 nm, 900 nm and 1200 nm. **a)** the BRFs; **b)** the ANIFs. The symbols represent BRFs and ANIFs based on simulations and the lines represent interpolated data based on a spline. ( $\vartheta_i = -45^\circ$ )

The polar plots of the 18 days old lawn grass are displayed in Figure 38. At 550 nm, 730 nm and 900 nm the ANIFs increased when the VZA increased. This effect is less pronounced at 1200 nm and 1600 nm. For all wavelengths, the highest ANIFs were found in the backward scatter direction. For all wavelengths except 670 nm, the lowest ANIFs were found at the nadir position. At 670 nm, the ANIF decreased when the VZA in the forward scatter direction increased (Figure 38b). This effect was also observed during the laboratory measurements and the SLC-model simulations of the 7 days old lawn grass. However, the effect was not observed during the laboratory measurements of the 18 days old lawn grass. This is due to bent grass haulms of the 18 days old lawn grass. The simulations of the 18

days old lawn grass were performed using LAD parameter settings for completely vertical leaves; however, the leaf of the 18 days old lawn grass were not completely vertical, resulting in a difference between measured and modelled anisotropic reflectance behaviour. The leaves of the 7 days old lawn grass were almost completely vertical. Therefore the simulations of the 18 days old lawn grass appear similar to the laboratory measurements of the 7 days old lawn grass. The simulations in the visible wavelengths show the most pronounced anisotropic reflectance effects. Just like at the SLC-model simulations of the 7 days old lawn grass, no clear hot-spot effect was simulated, which is probably due to the narrow leaves of the 18 days old lawn grass.

18 days old lawn grass

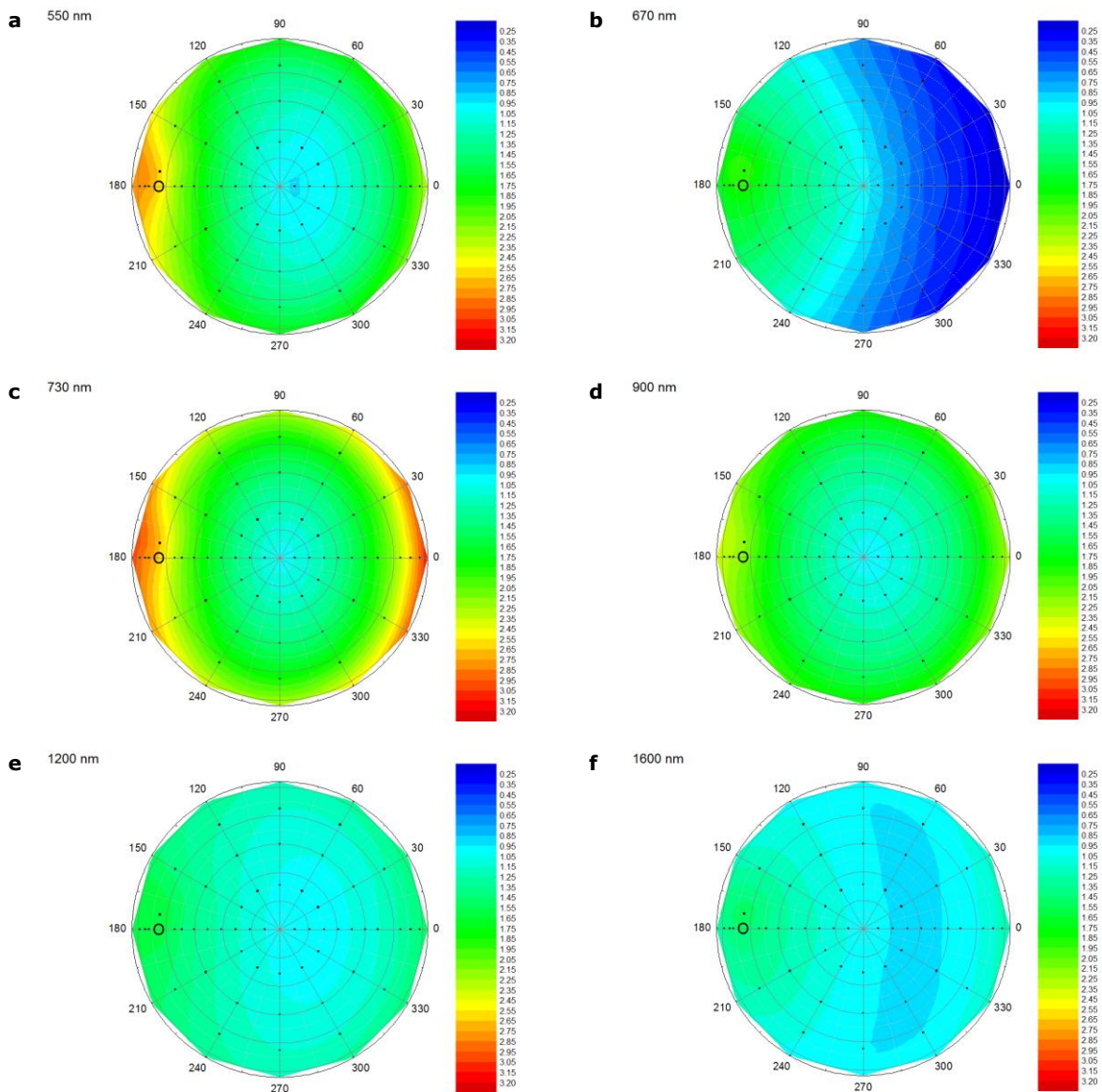


Figure 38. Interpolated polar plots of the ANIFs of 18 days old lawn grass simulated by the SLC-model at 550 nm, 670 nm, 730 nm, 900 nm, 1200 nm and 1600 nm. The black dots indicate the measurement positions and the circle indicates the hot-spot position.

### 3.2.4 7 Days old watercress

Figure 39 displays the reflectance of the laboratory measurements and the SLC-model simulations at VZA = 0°, VZA = -60° and VZA = 60° of the 7 days old watercress. At both a VZA at nadir and at 60° in the backward direction from approximately 700 nm, the SLC-simulations seem to overestimate the reflectance (Figure 39a and Figure 39b). At these positions, the peak in the green part of the spectrum, which was observed at the laboratory measurements, does not occur at the simulations. The best match between the laboratory measurements and the SLC-model simulations seems to be at 60° in the forward scatter direction (Figure 39c).

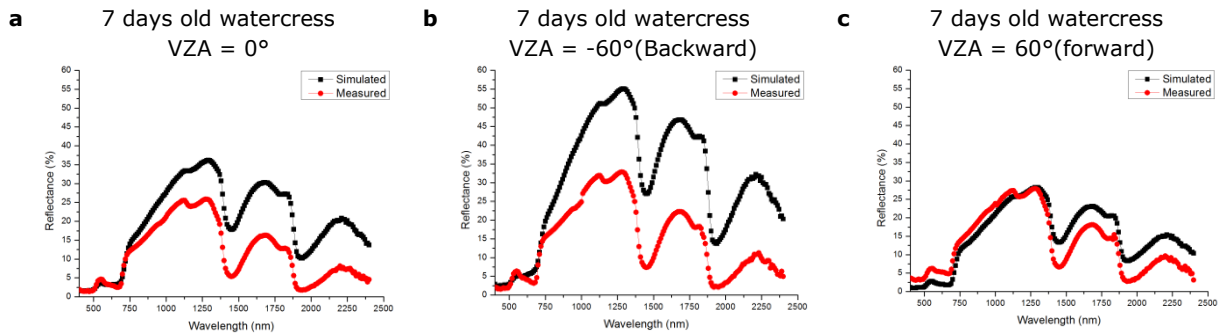


Figure 39. Simulated (black) and measured (red) reflectance of 7 days old watercress: **a)** VZA = 0°; **b)** VZA = -60° (backward scatter direction); **c)** VZA = 60° (forward scatter direction). ( $\vartheta_i = -45^\circ$ )

When normalizing the BRFs, it becomes clear that for the SLC-model simulations, the highest ANIFs occur in the back scatter direction around the hot-spot position (Figure 40b). The ANIFs decreased in the forward scatter direction when the VZA increased. At 670 nm, the anisotropic reflectance effects were the greatest. For the other depicted wavelengths, the anisotropic effects are almost similar.

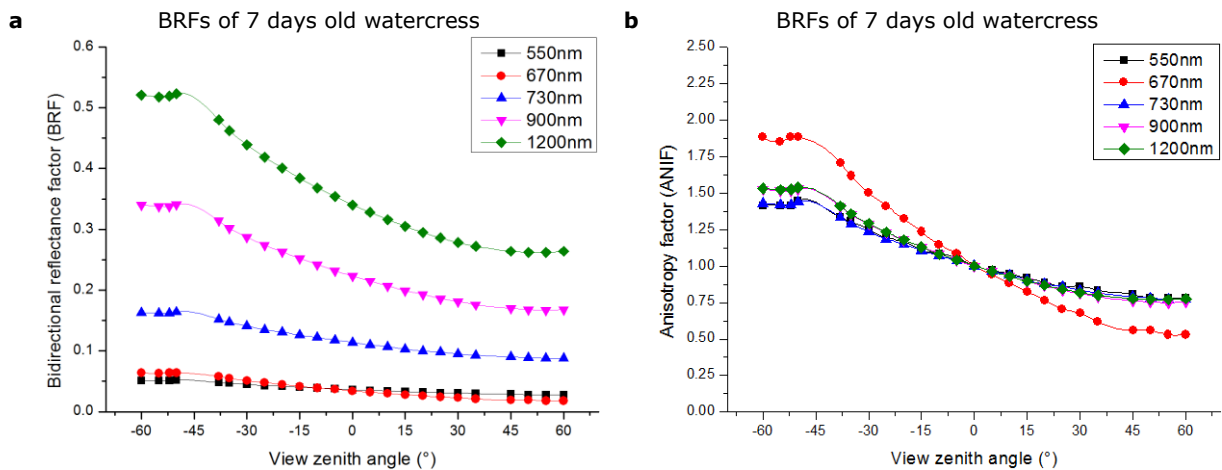


Figure 40. Simulated BRFs and ANIFs of 7 days old watercress over the principal plane at 550 nm, 670 nm, 730 nm, 900 nm and 1200 nm. **a)** the BRFs; **b)** the ANIFs. The symbols represent BRFs and ANIFs based on the simulations and the lines represent interpolated data based on a spline. ( $\vartheta_i = -45^\circ$ )

In the polar plots in Figure 41, the highest ANIFs are found in the backward scatter direction for all wavelengths. In the forward scatter direction, the ANIFs decreased when the VZA increased. The effects are similar at all wavelengths. The greatest anisotropic effects occur at 670 nm: here the highest and lowest ANIFs are found. Like at the simulations of the lawn grass, no clear hot-spot effect was simulated. Due to the low LAI of the 7 days old watercress, the simulations appear similar to the

simulation of the bare soil. The increased ANIF in the backward scatter direction is likely to be caused by the wide and faint hot-spot effect of the bare soil. Just like the bare soil, there appears to occur no forward scattering. It is possible that the forward scattering component of the planophile watercress leaves is dominated by the reflectance anisotropy of the bare soil due to the low LAI of the 7 days old watercress, resulting in the absence of a forward scattering component at the simulations.

7 days old watercress

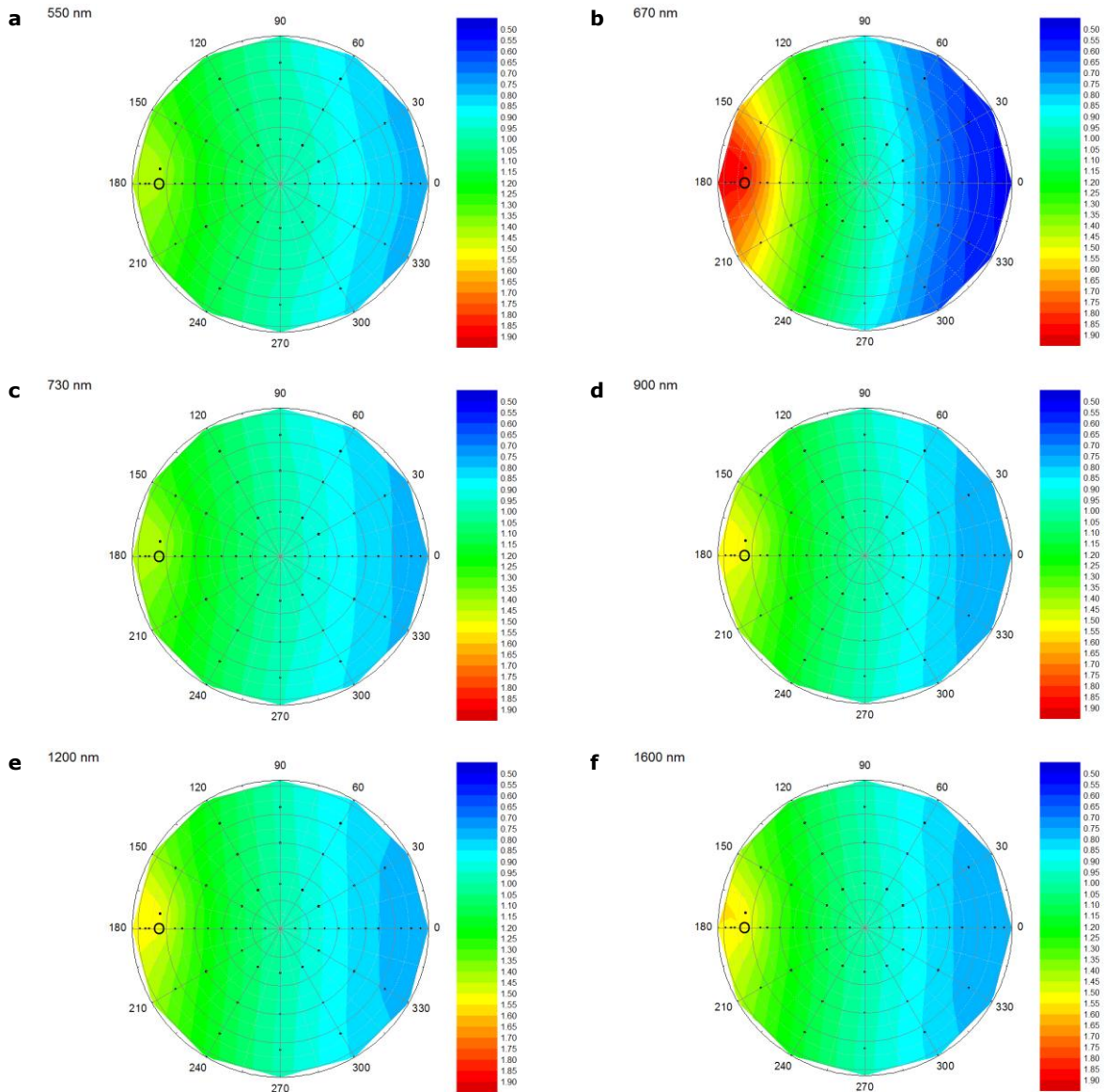


Figure 41. Interpolated polar plots of the ANIFs of 7 days old watercress simulated by the SLC-model at 550 nm, 670 nm, 730 nm, 900 nm, 1200 nm and 1600 nm. The black dots indicate the measurement positions and the circle indicates the hot-spot position.

### 3.2.5 18 Days old watercress

Figure 42 shows the simulations and laboratory measurements of the 18 days old watercress. The peak in the green part of the spectrum, measured in the laboratory, does not occur so pronounced at the simulations. At a VZA of 0° and 60° in the backward scatter direction, between 700 nm and 1000 nm, the simulations underestimated the reflectance and from 1000 nm till 2400 nm, the model overestimates the reflectance (Figure 42a and Figure 42b). At a VZA of 60° in the forward scatter direction, the model underestimates the laboratory measurement from 400 nm till 1400 nm and from 1400 nm till 2400 nm the model slightly overestimates the reflectance (Figure 42c).

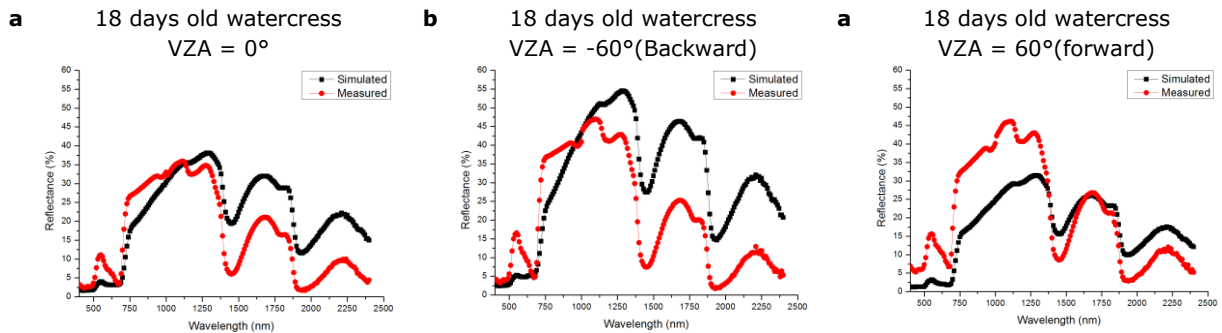


Figure 42. Simulated (black) and measured (red) reflectance of 18 days old watercress: **a)** VZA = 0°; **b)** VZA = -60° (backward scatter direction); **c)** VZA = 60° (forward scatter direction). ( $\vartheta_i = -45^\circ$ )

The BRFs and ANIFs in the principal plane indicate, for all depicted wavelengths, that the reflectance increased in the backward scatter direction, when the VZA increased, up to the hot-spot position (-45°) (Figure 43). At VZAs greater than the hot-spot position, the reflectance slightly decreased again. In the forward scatter direction, the reflectance decreased when the VZA increased. The most variation, and thus the most pronounced anisotropic effects, are found at 670 nm (Figure 43b).

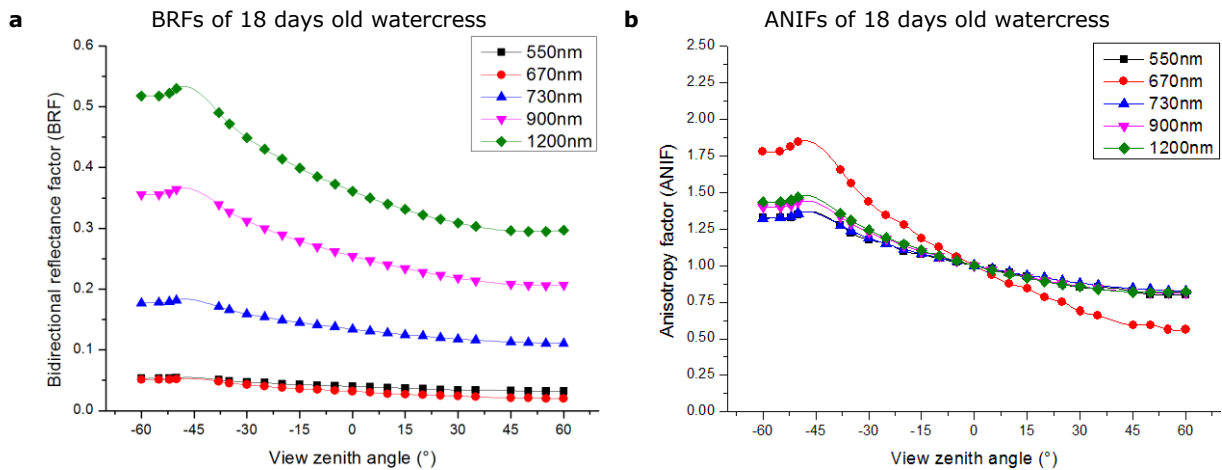
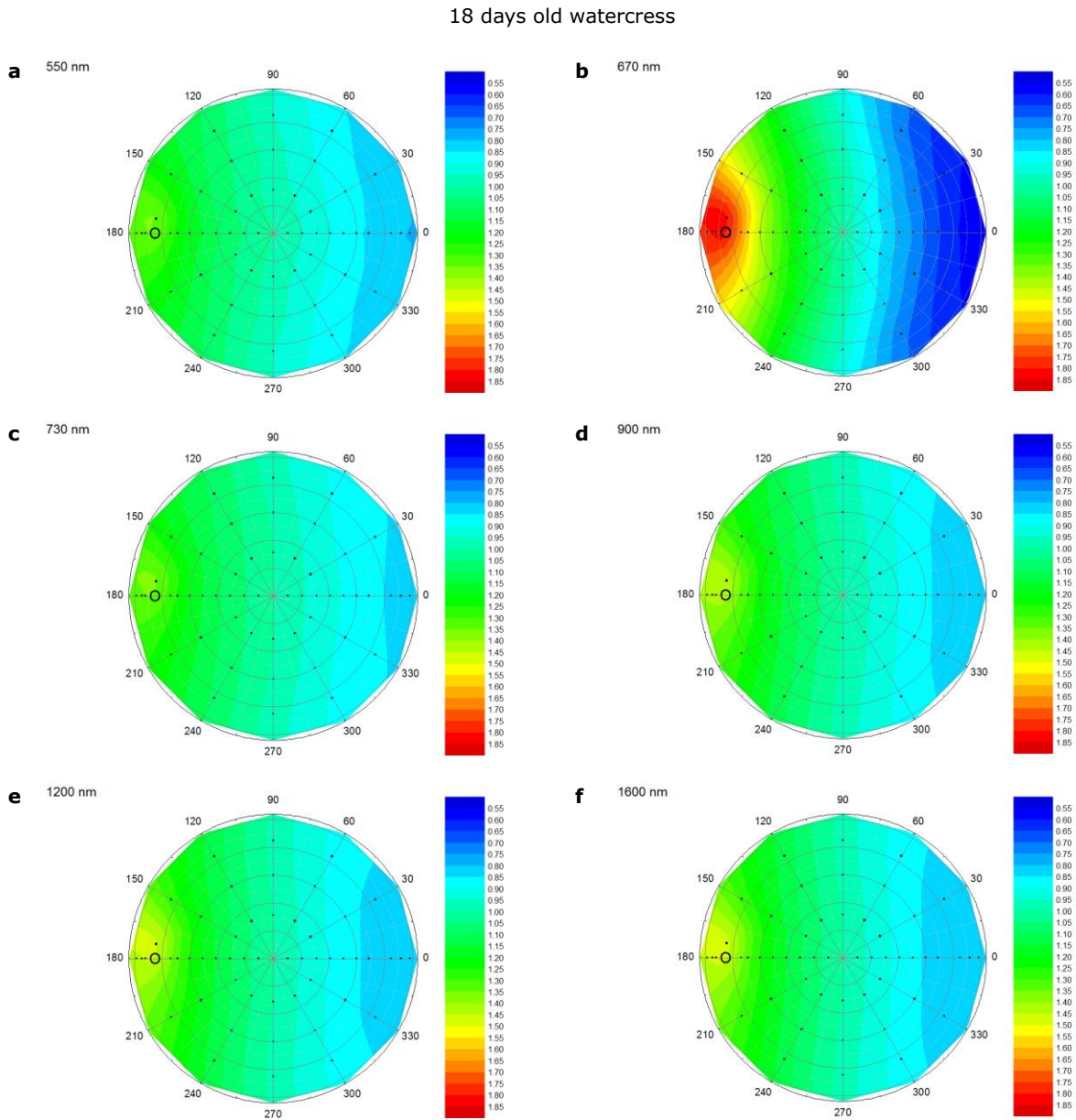


Figure 43. Simulated BRFs and ANIFs of 18 days old watercress over the principal plane at 550 nm, 670 nm, 730 nm, 900 nm and 1200 nm. **a)** the BRFs; **b)** the ANIFs. The symbols represent the BRFs and ANIFs based on simulations and the lines represent interpolated data based on a spline. ( $\vartheta_i = -45^\circ$ )

The polar plots, displayed in Figure 44, show increased ANIFs in the backscatter direction for all depicted wavelengths. Compared to the 7 days old watercress, the maximum ANIF occurs at the hot-spot position. This might be caused by the higher used value of the LAI parameter of the 18 days old

watercress compared to the 7 days old watercress. In the forward scatter direction, there was a decrease in ANIFs. The strongest reflectance anisotropy occurred at 670 nm (*Figure 44b*).



*Figure 44. Interpolated polar plots of the ANIFs of 18 days old watercress simulated by the SLC-model at 550 nm, 670 nm, 730 nm, 900 nm, 1200 nm and 1600 nm. The black dots indicate the measurement positions and the circle indicates the hot-spot position.*

### 3.3 Laboratory Measurements vs. SLC simulations

The ability of the SLC-model to simulate the laboratory measurements is assessed by the calculation of the RMSE of the measured and the simulated reflectance, for the 400 – 2400 nm range at an interval of 10 nm (see equation (16)). *Figure 45* shows how the RMSE (%) of the measured and simulated reflectance changed over the principal plane at the observation positions that were also measured in the laboratory, of the soil and vegetation targets.

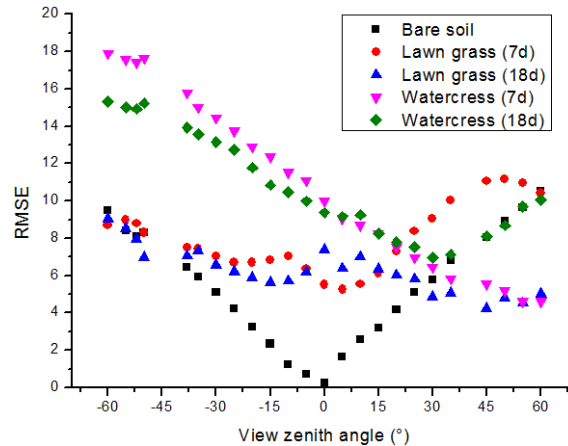


*Figure 45. RMSE (%) between the measured and simulated reflectance as a function of VZA over the principal plane. The symbols represent the RMSE of the simulations and the measurements and the lines represent interpolated data based on a spline. ( $\vartheta_i = -45^\circ$ )*

The RMSE of the bare soil input and output at nadir position is only 0.087%. The low RMSE is due to the fact that the bare soil which is measured in the laboratory is used as the input for the simulation of the bare soil output by the SLC-model at a VZA of  $0^\circ$ . When the VZA increased, independent of the direction over the principal plane, the RMSE of measured and simulated bare soil increased. In the forward scatter direction even up till 10.50% (VZA =  $60^\circ$ ). This could be the result of incorrect soil parameter settings. For the simulations, the soil parameters were left at their default value, which were parameters derived from a ploughed soil (Pinty et al. 1989). Because simulating off-nadir soil spectra results in an increase in RMSE values, it is likely that the used parameters do not apply to the soil that was measured in the laboratory. This also becomes clear when comparing the ANIF of the measurements and simulations over the bare soil at 670 and 900 nm (*Figure 46*). The measured bare soil has increased ANIFs around the hot-spot position and in the forward direction. The simulated bare soil has increasing ANIFs in the backward scattering direction and decreasing ANIFs in the forward scatter direction. This indicates that the soil parameters that were used for the simulations were insufficient to describe the reflectance anisotropy of the measured soil. The SLC-model overestimates the reflectance anisotropy.

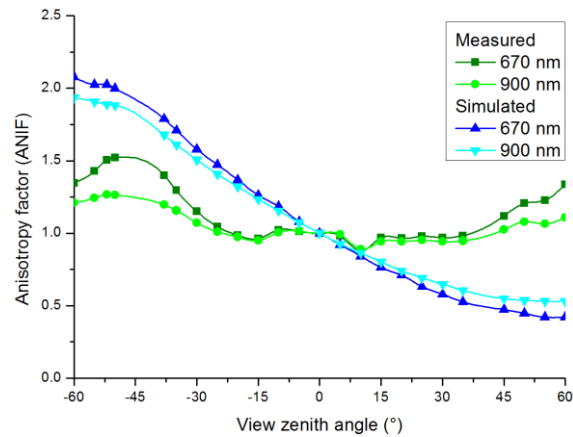


Figure 46. Measured and simulated ANIFs over the principal plane of bare soil, at 670 and 900 nm. The symbols represent the ANIFs of the simulations and the measurements and the lines represent interpolated data based on a spline. ( $\vartheta_i = -45^\circ$ )

Both the 7 days and 18 days old lawn grass have a RMSE between 5% and 10% in the backward scatter direction. In the forward scatter direction, the RMSE of the 7 days old lawn grass increased up to 11.16% (VZA = 50°), while the RMSE of the 18 days old lawn grass slightly decreased. Both the 7 days and 18 days old watercress have the highest RMSE in the backward scatter direction, up till 17.91% and 15.32% at VZA = -60°, for the 7 days and 18 days old watercress, respectively. For the 7 days old watercress, the RMSE decreased as the VZA increased in the forward scatter direction. For the 18 days old watercress, the RMSE decreased in the forward scatter direction up to a VZA of 30°. After this position the RMSE increased again. Although the measured and simulated spectra showed great differences, there were some effects, which the SLC-model was able to simulate. For instance, the increased ANIFs around the hot-spot position and the decreasing ANIF in the forward scatter direction at 670 nm and the increasing ANIFs at off-nadir VZAs at 900 nm for both the lawn grass targets, see Figure 47.

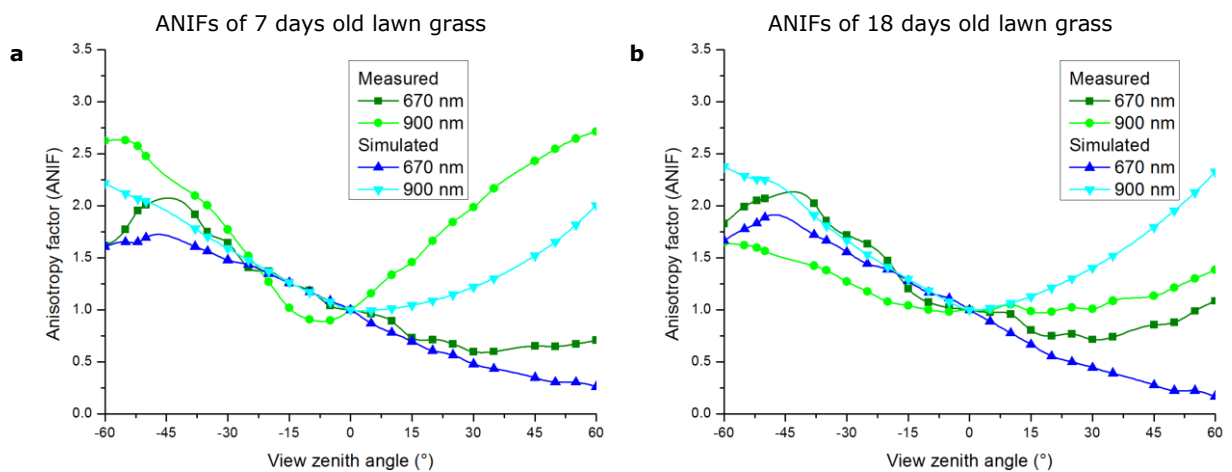
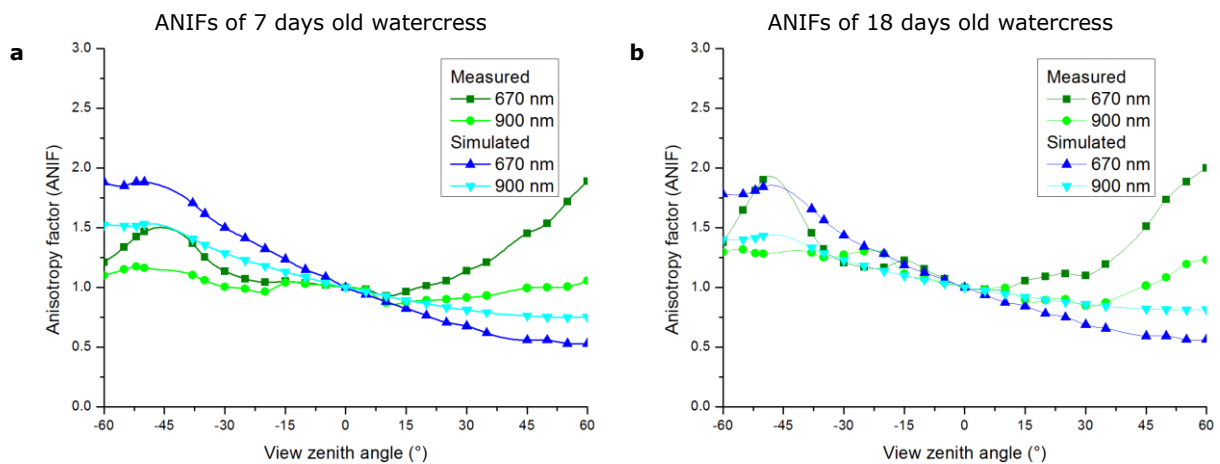


Figure 47. Measured and simulated ANIFs over the principal plane of lawn grass. **a)** 7 days old lawn grass; **b)** 18 days old lawn grass, at 670 and 900 nm. The symbols represent the ANIFs of the simulations and the measurements and the lines represent interpolated data based on a spline. ( $\vartheta_i = -45^\circ$ )

The watercress targets showed the highest RMSE values in the backward scatter direction, see Figure 45. At nadir position, the RMSE values of the watercress are the highest of all simulated vegetation

targets. This indicates that the used parameter settings for the simulation were not able to describe the measured watercress spectra. In the backward scatter direction, the RMSE of both targets increases up to 18% for the 18 days old lawn grass. However, in the backward scatter direction, the model was able to partly simulate the reflectance anisotropy of 18 days old watercress, resulting in nearly similar ANIFs at both 670 and 900 nm (*Figure 48*). The forward scattering component, which is present at the laboratory measurements, is not simulated by the SLC-model. This is probably because of the large contribution of the soil to the watercress simulations, due to the low LAI values of the watercress targets. The soil did not have a forward scattering component as well and probably therefore the watercress simulations did not either. Although the leaves of the watercress might have forward scattering properties, the backward scattering properties of the soil dominated this.



*Figure 48. Measured and simulated ANIFs over the principal plane of watercress. a) 7 days old watercress; b) 18 days old watercress, at 670 and 900 nm. The symbols represent the ANIFs of the simulations and the measurements and the lines represent interpolated data based on a spline. ( $\vartheta_i = -45^\circ$ )*

At nadir position, the RMSE of the bare soil is close to 0%. However, the RSME for the vegetation targets ranges from 5% to 11%. This indicates that the SLC-model is already not able to simulate the laboratory measurements accurately when using parameters, which were accurately derived from the vegetation, not even if only the nadir position is considered.

Apart from the possibility that incorrect vegetation parameters were applied, it is also possible that the high RMSE values are caused by the fact that the SLC-model simulates bidirectional reflectance factors, while in the laboratory biconical reflectance factors were measured. Because of the  $8^\circ$  field of view of the spectrometer, the laboratory measurements integrate the reflectance over a range of angles. Therefore, the laboratory measurements and the SLC simulation are different quantities. This could have as a result that the laboratory measurements, as performed using the set-up as described in the methodology section, are not comparable to the SLC simulations.

### 3.4 Illumination angle

In the previous sections, the measurements and simulations at an illumination angle of  $45^\circ$  were described. Changing the illumination angle, however, influences the magnitude and distribution of anisotropic reflectance effects (Kimes 1983). In order to measure this, the measurements and simulations over the hemisphere were repeated at an illumination angle of  $30^\circ$ . To provide an insight in the changes in the anisotropic effects at an illumination angle of  $30^\circ$ , polar plots of the ANIFs of the measurements and simulations of the soil and vegetation targets are displayed in *Figure 49 - Figure 53*.

Both the measurements and the simulations of the bare soil show a clear shift of the maximum ANIF towards the hot-spot position at all depicted wavelengths (*Figure 49*). For the measurements and simulations of the 7 and 18 days old lawn grass targets, the hot-spot shift is also present, only less pronounced, see *Figure 50* and *Figure 51*, respectively. Especially the simulations of the 7 days old lawn grass showed comparable anisotropic reflectance behaviour to the laboratory measurements. The simulations of the watercress targets show a clear hot-spot effect (*Figure 52* and *Figure 53*). The laboratory measurements of the watercress show an increased ANIF in the backward scatter direction; however, a clear hot-spot was not observed. The polar plots of the laboratory measurements of the watercress targets also show a strong asymmetrical pattern. This can be explained due to the inhomogeneous distribution of the watercress plants and the roughness of the soil. At different azimuthal viewing directions, independent of the zenith view angle, different proportions of the vegetation and the soil, and illuminated and shaded canopy parts are observed, resulting in an unexpected reflectance anisotropy pattern.

Overall, the same effects as observed at an illumination angle of  $45^\circ$  are found at an illumination of  $30^\circ$ . The major changes, as expected, are a shift of the hot-spot position and in some cases a decrease in anisotropic effects. Because the measured and simulated reflectance anisotropy is already described in detail in the previous sections, the reflectance anisotropy of the targets at an illumination angle of  $30^\circ$  will not be described any further. In the next section, the differences in reflectance anisotropy at changing illumination angles will be described by means of the ANIX.

Bare Soil

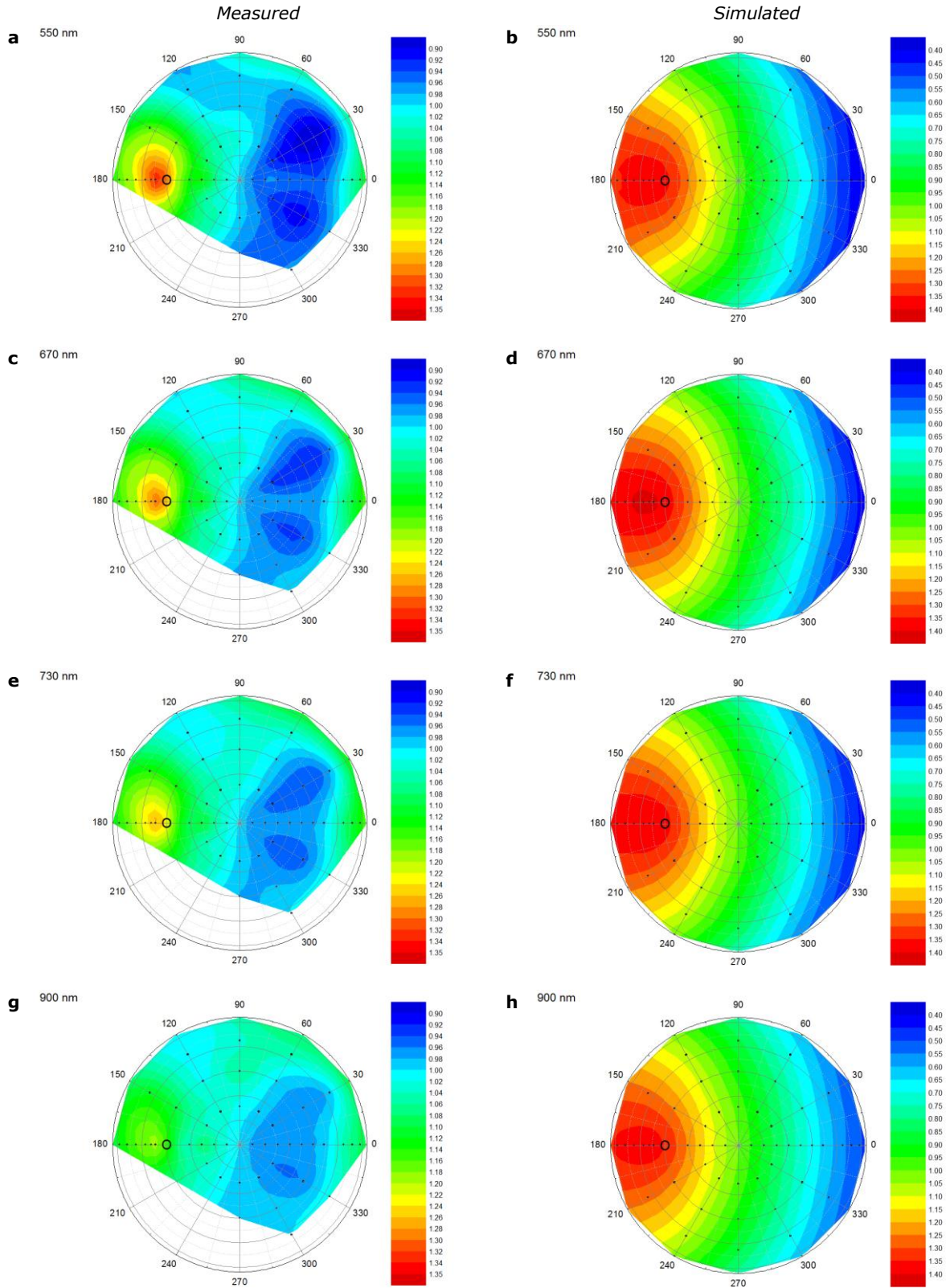


Figure 49. Interpolated polar plots of the ANIFs of bare soil as measured in the laboratory and simulated by the SLC-model at 550 nm, 670 nm, 730 nm and 900 nm. The black dots indicate the measurement positions and the circle indicates the hot-spot position.

7 days old lawn grass

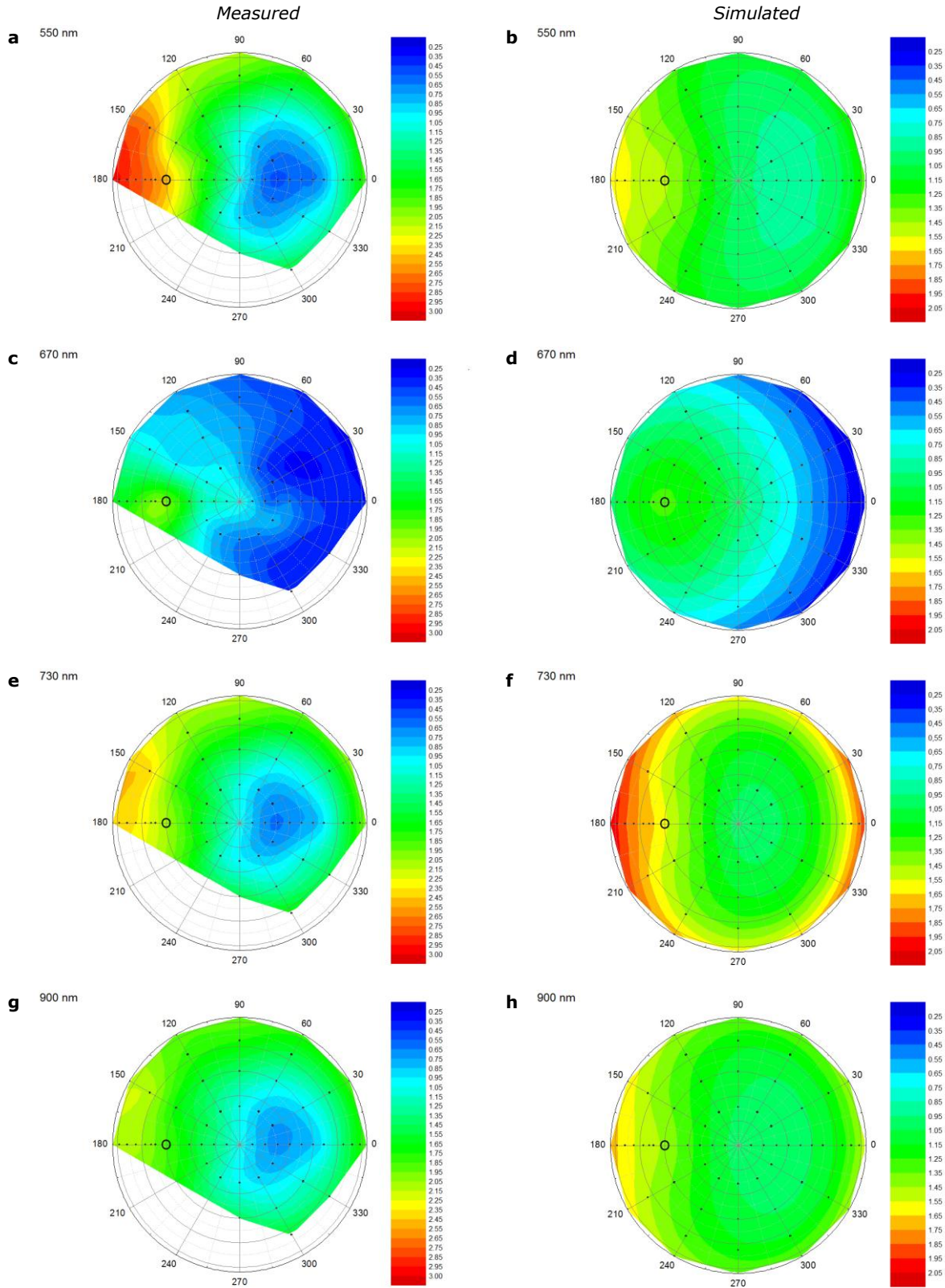


Figure 50. Interpolated polar plots of the ANIFs of 7 days old lawn grass as measured in the laboratory and simulated by the SLC-model at 550 nm, 670 nm, 730 nm and 900 nm. The black dots indicate the measurement positions and the circle indicates the hot-spot position.

18 days old lawn grass

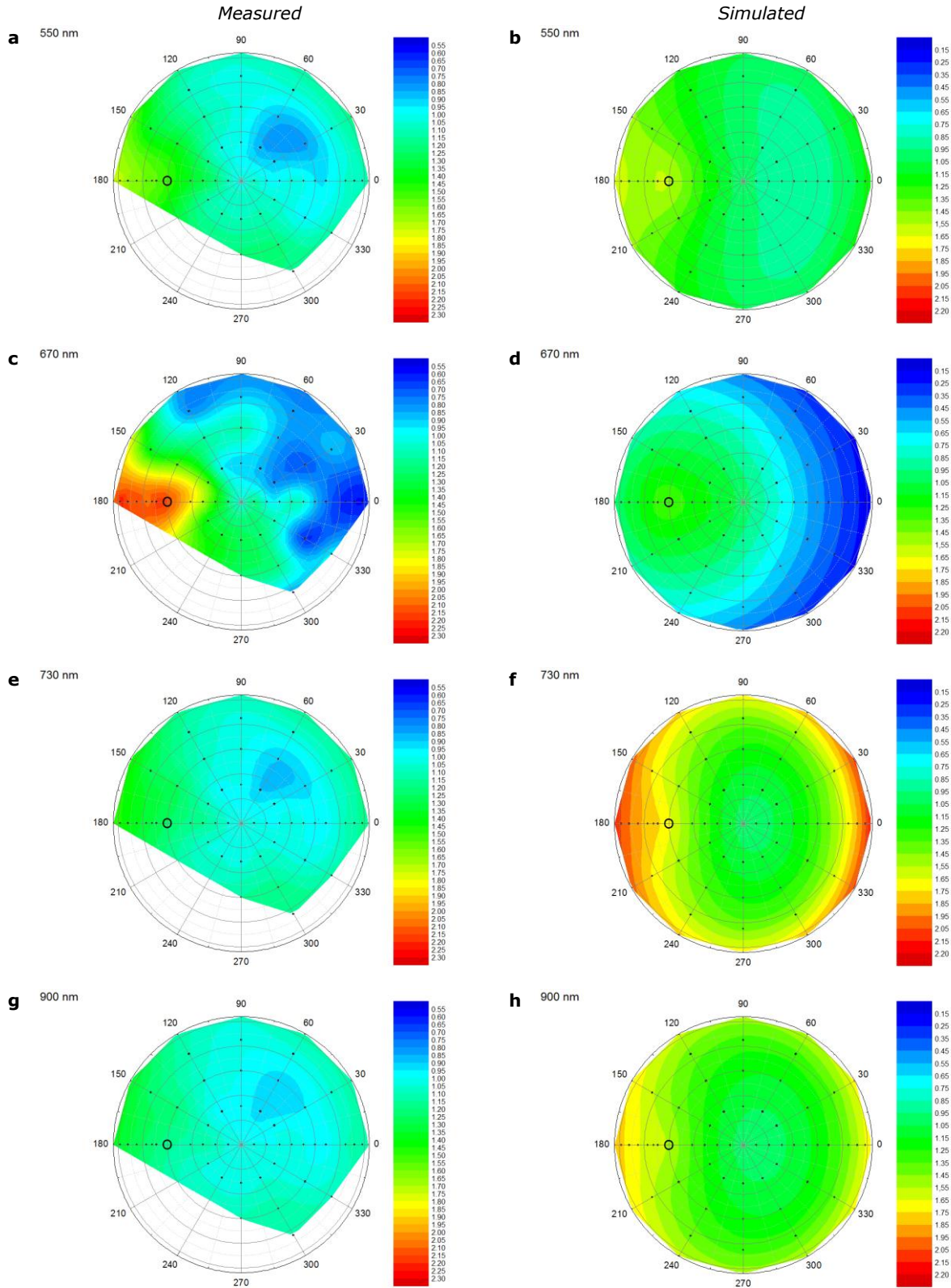


Figure 51. Interpolated polar plots of the ANIFs of 18 days old lawn grass as measured in the laboratory and simulated by the SLC-model at 550 nm, 670 nm, 730 nm and 900 nm. The black dots indicate the measurement positions and the circle indicates the hot-spot position.

7 days old watercress

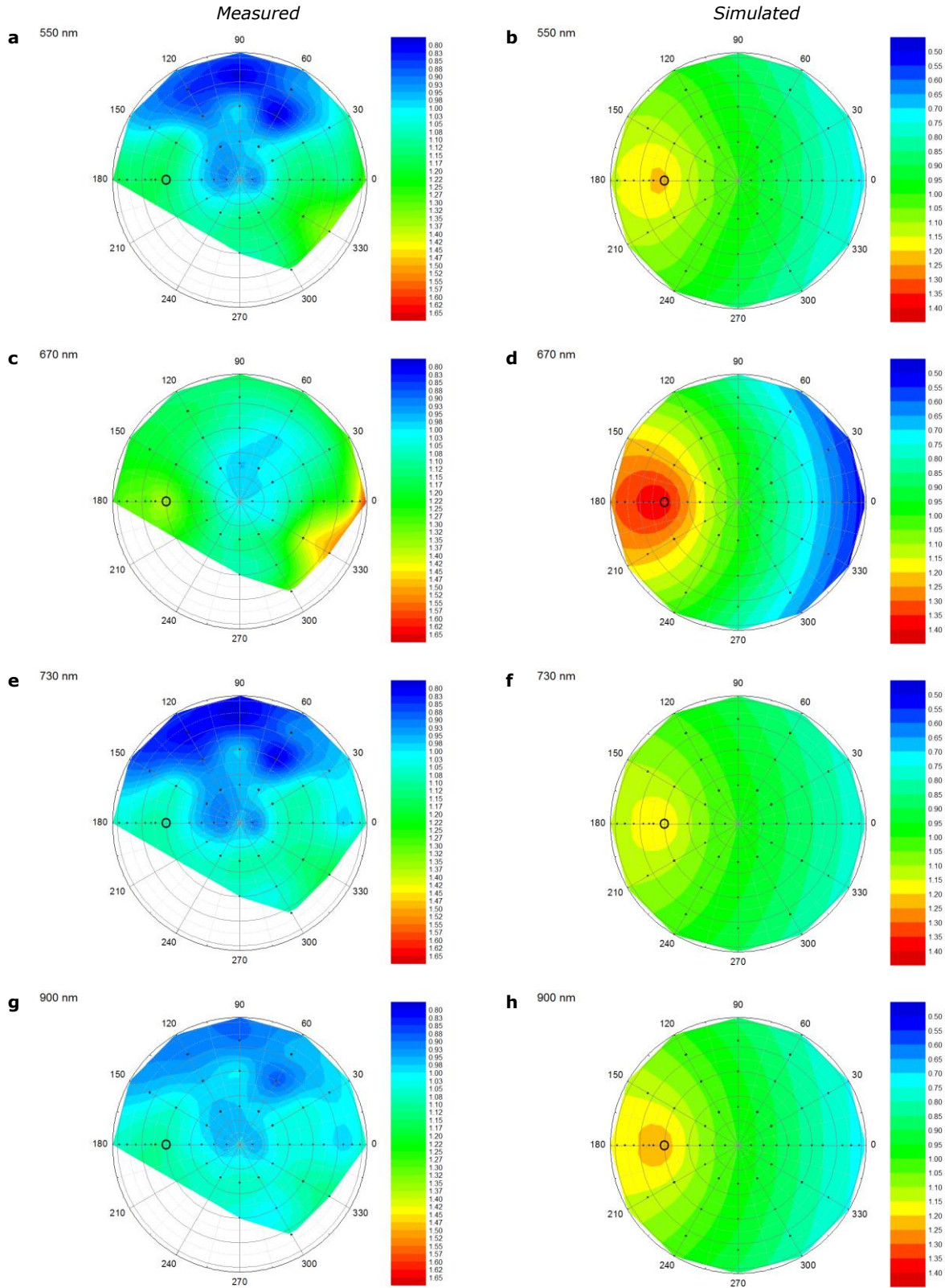


Figure 52. Interpolated polar plots of the ANIFs of 7 days old watercress as measured in the laboratory and simulated by the SLC-model at 550 nm, 670 nm, 730 nm and 900 nm. The black dots indicate the measurement positions and the circle indicates the hot-spot position.

18 days old watercress

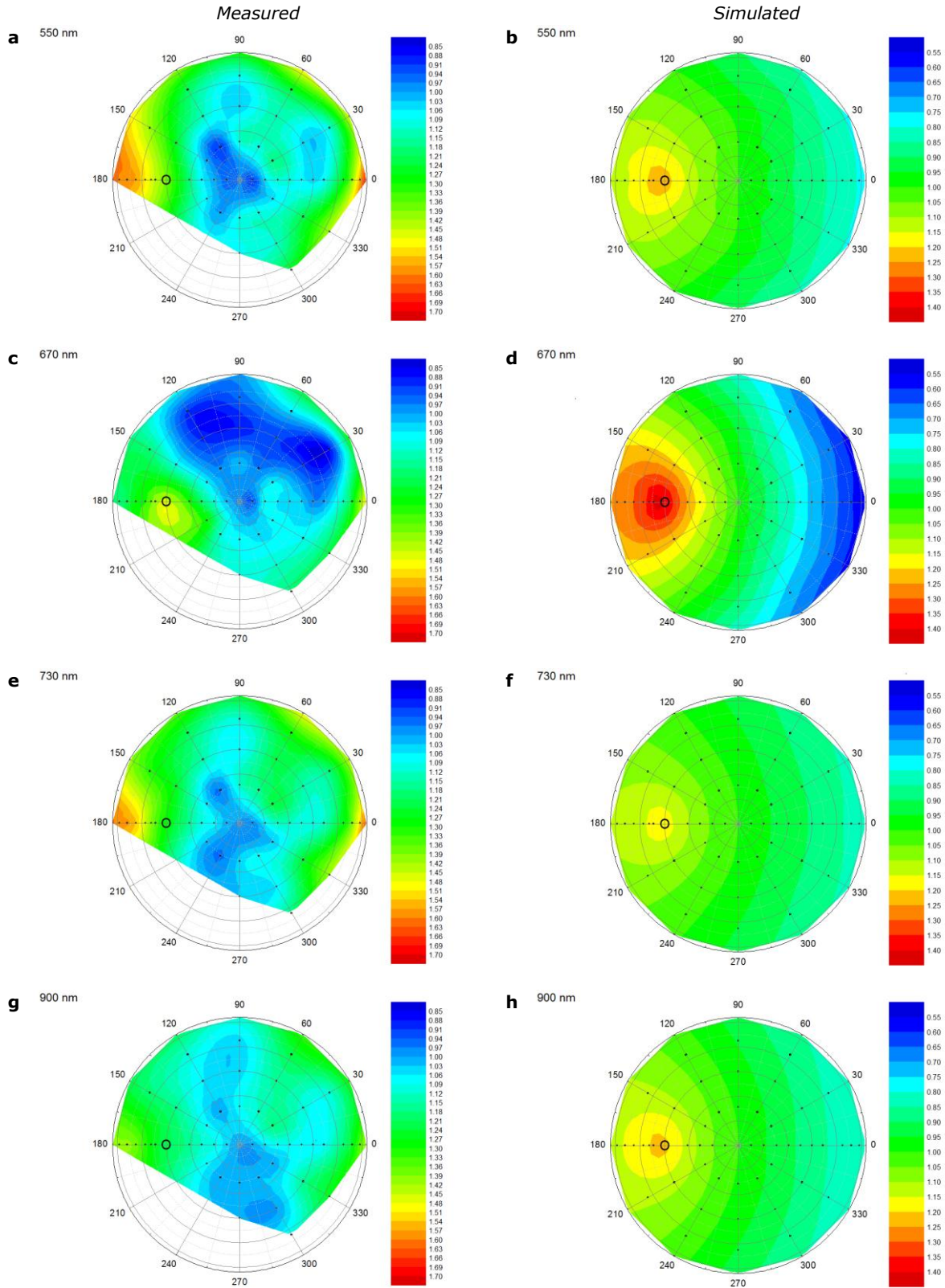
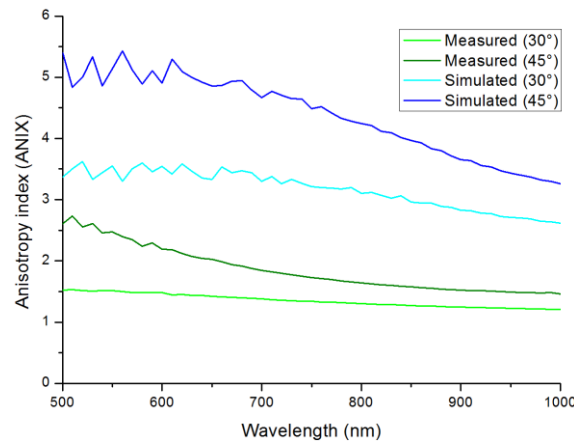


Figure 53. Interpolated polar plots of the ANIFs of 18 days old watercress as measured in the laboratory and simulated by the SLC-model at 550 nm, 670 nm, 730 nm and 900 nm. The black dots indicate the measurement positions and the circle indicates the hot-spot position.

### 3.5 Anisotropy index

The ANIX describes the magnitude of anisotropy over a defined plane, see equation (15) (Sandmeier et al. 1998a). *Figure 54* shows the anisotropy indices of the measured and simulated bare soil target over the principal plane. For both the measured and the simulated bare soil target, the highest anisotropy indices are observed at an illumination angle of 45°. The higher ANIX at a greater illumination angle is caused by the higher proportion of shadows that are produced at greater illumination angles, which result in a stronger contrast between illuminated and shadowed parts of the bare soil (Kimes 1983). The simulated bare soil returns a higher ANIX compared to the laboratory measurements. The reason for this, is that the parameters, which were applied to simulate the bare soil, were derived from a ploughed soil (Pinty et al. 1989), which was probably more rough compared to the bare soil that was measured in the laboratory. A rougher soil results in a stronger optical contrast between illuminated and shadowed parts of the soil and therefore greater varying reflectance factors and thus in a greater quantity of reflectance anisotropy (Jackson et al. 1990). This effect is in agreement with the results of Wang et al. (2012), who also found stronger reflectance anisotropy at rougher soils.



*Figure 54. Anisotropy indices (ANIX) of the measured and simulated bare soil as a function of wavelength at an illumination angle of 30° and 45°.*

*Figure 55* shows the ANIX of the measured and simulated vegetation targets. The simulated anisotropy indices of the 7 and 18 days old lawn grass (*Figure 55a* and *Figure 55b*) are in agreement with the physical mechanisms as described by Kimes (1983): a greater illumination angle results in stronger reflectance anisotropy. The ANIX of the measured 7 days old lawn grass data shows unexpected behaviour: the ANIX decreases at a greater illumination angle. An explanation for this could be the inhomogeneity of the lawn grass targets. Because the targets were moved between the measurements at a 30° and 45° illumination angle, it is possible that not exactly the same area was measured during the measurements at an illumination angle of 30° and 45°. This cannot be explained by the shadow mechanisms that are described by Kimes (1983) and could therefore indicate that different proportions of vegetation and bare soil are observed by the spectrometer at different illumination angles.

The greatest anisotropy indices, for both the lawn grass and the watercress, are found in the red part of the spectrum, with a peak ANIX around 670 nm. This is the result of the high proportion of chlorophyll absorption around 670 nm (Curran 1989), which results in a low ANIF in the forward

direction and therefore in a high ANIX. Due to the relative low amount of absorption in the green, and especially in the NIR, the contrast between the illuminated and shadowed parts of the canopy decreases, which results in a low ANIX. This is in agreement with the physical mechanism as described by Kimes (1983) and is also observed by Sandmeier et al. (1998a).

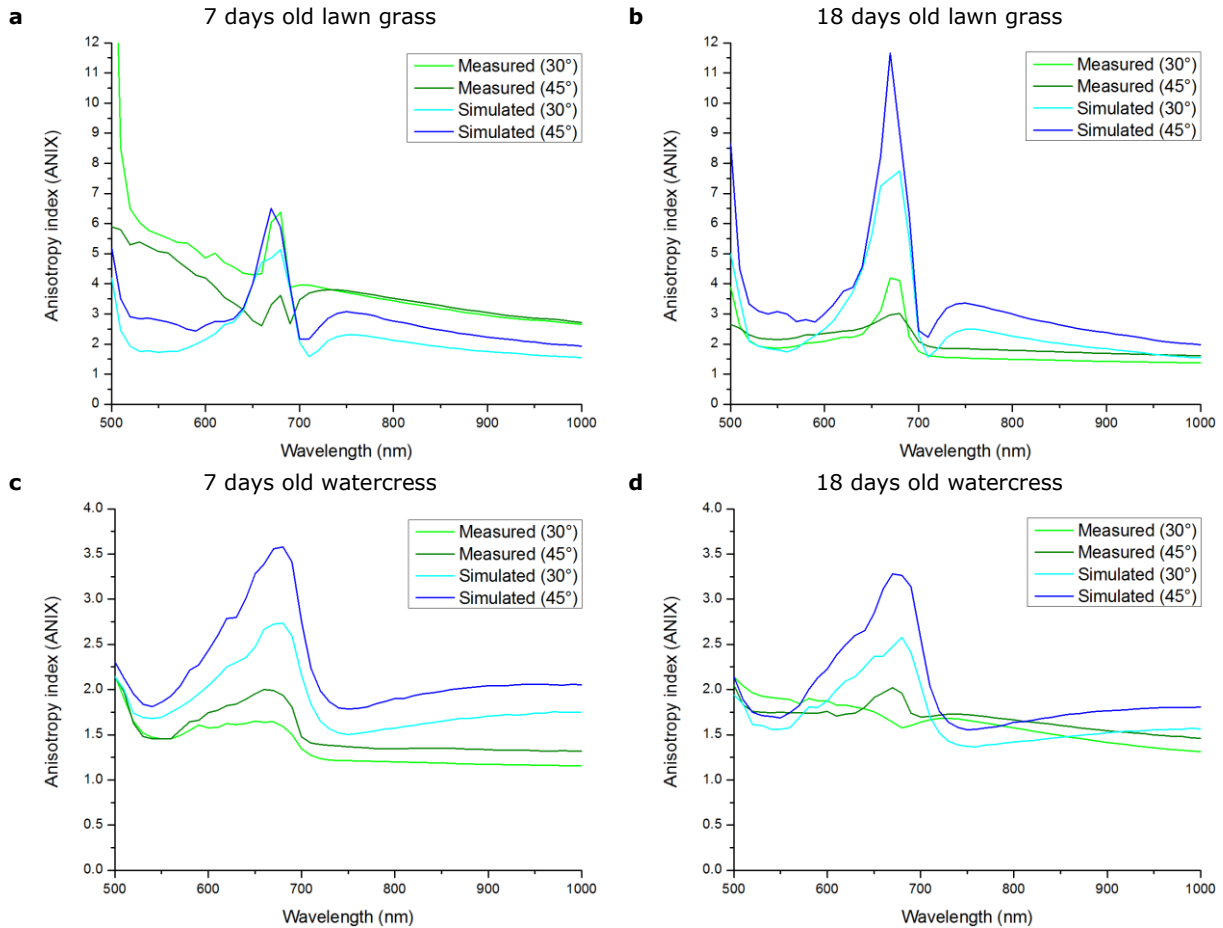


Figure 55. Anisotropy indices (ANIX) of the measured and simulated lawn grass and watercress as a function of wavelength at an illumination angel of 30° and 45°. **a)** 7 days old lawn grass; **b)** 18 days old lawn grass; **c)** 7 days old watercress and; **d)** 18 days old watercress.

Structural differences cause the ANIX of the lawn grass targets to be higher than the ANIX of the watercress targets. For the lawn grass targets, especially the 7 days old lawn grass, there is a great difference in the proportion of observed (light) vegetation and (dark) bare soil between nadir and off-nadir observations due to the erectophile LAD. This results in large differences in ANIF and thereby in high anisotropy indices. This contrast in observed proportion of vegetation and bare soil, observed at nadir and off-nadir positions, is not as great for the watercress targets due to the planophile LAD, resulting in smaller differences in ANIF and thus in smaller anisotropy indices. Both the laboratory measurements and the SLC simulations show this behaviour.



## 4 DISCUSSION

### 4.1 Parameters SLC-model

As shown in the results and discussion section, there is a great difference between measured and modelled reflectance. It is a possibility that the one or more of the parameter settings used for the vegetation simulations were incorrect. In order to try to obtain a better match between the laboratory measurements and the simulations, and to make sure that not just a single incorrect parameter was causing the differences, the SLC simulations were repeated with different settings for the LAI, LIDFa and LIDFb and the Cs and Cw parameters. During the simulations, only one of the parameters was changed, while the others were kept at the value of the original simulations. The outputs of the SLC-model were again compared to the laboratory measurements. The effect of changing parameter values was investigated for three positions over the principal plane. One in the backward scatter direction, one at nadir position and one in the forward scatter direction:  $-60^\circ$ ,  $0^\circ$  and  $60^\circ$ , respectively. Responsibilities

#### 4.1.1 Leaf Area Index

LAI is one of the key structural parameters that determines the spectral response of vegetation. It is a possibility that the difference between the measured and the simulated reflectance is caused by the fact that the spectrometer has a conical IFOV. Due to the conical IFOV, the spectrometer integrates a proportion of leaf elements over a range of angles, which might be higher compared to what was simulated by the SLC-model. Therefore, the simulations are repeated with a stepwise increased LAI value, see *Table 12*.

*Table 12. LAI parameter settings for the repeated SLC simulations.*

	Original	1	2	3	4
7 days old lawn grass	0.79	1.0	1.2	1.4	1.6
18 days old lawn grass	1.2	1.4	1.6	1.8	2.0
7 days old watercress	0.18	0.3	0.4	0.5	0.6
18 days old watercress	0.28	0.4	0.5	0.6	0.7

For the 7 days old lawn grass, increasing the LAI parameter seems to decrease the difference between the measured and simulated spectral signatures, see *Figure 56a-c*. The reflectance in the NIR is in particular better simulated by the SLC-model with higher LAI parameter values. The nadir and the backward scatter simulation of the 18 days old lawn grass, is negatively affected by the increasing LAI value for the 1000 – 2500 nm region, while the 700 – 1000 nm region is positively influenced, see *Figure 56a* and *Figure 56b*, respectively. In the latter region, the difference between measured and simulated reflectance decreases in the forward scatter direction (*Figure 56f*).

Increasing the LAI value does not have a positive effect on the watercress simulations, see *Figure 57*. The higher LAI values increase the difference between measured and simulated reflectance in the NIR region for both the 7 and 18 days old watercress. Only in the forward scatter direction, in the 800 – 1400 nm range, the simulations with higher LAI values better estimate the laboratory measurements, see *Figure 57f*. Judging the simulations with the increased LAI parameter settings, it

might be that decreasing the LAI would positively affect the watercress simulation, which indicates that in the original simulation the LAI was overestimated.

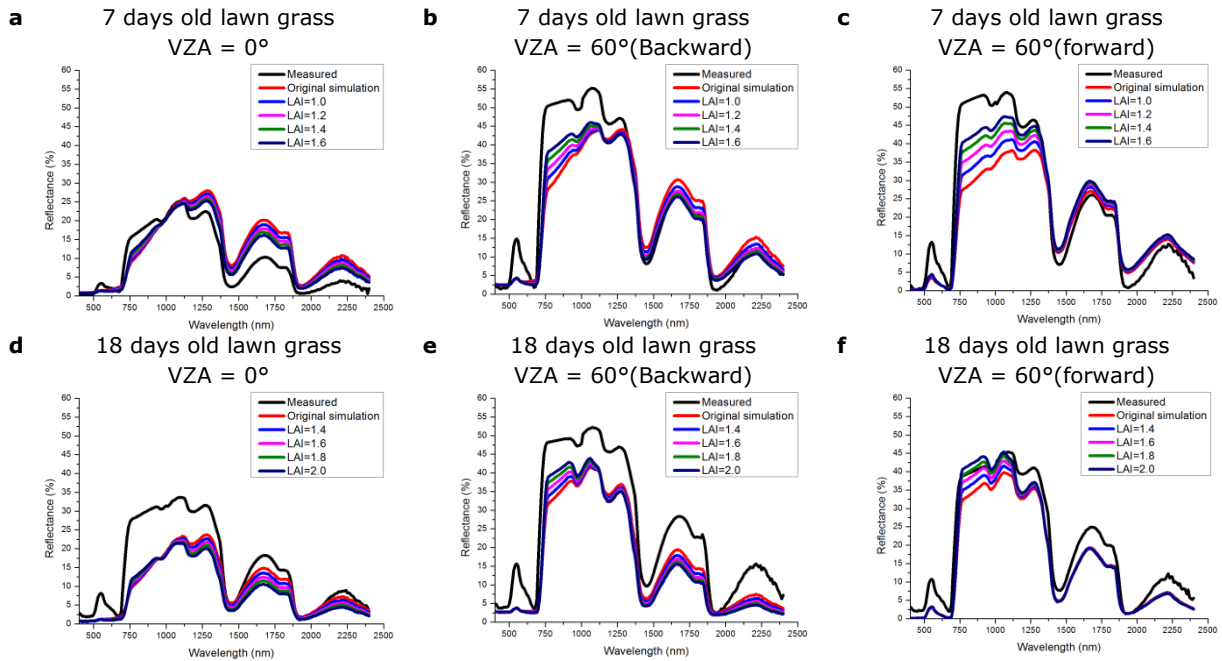


Figure 56. SLC simulations with different LAI values for lawn grass. For the 7 days old lawn grass: **a)** VZA = 0°; **b)** VZA = 60° (backward); **c)** VZA = 60° (forward) and for the 18 days old lawn grass: **d)** VZA = 0°; **e)** VZA = -60° (backward); **f)** VZA = 60° (forward).

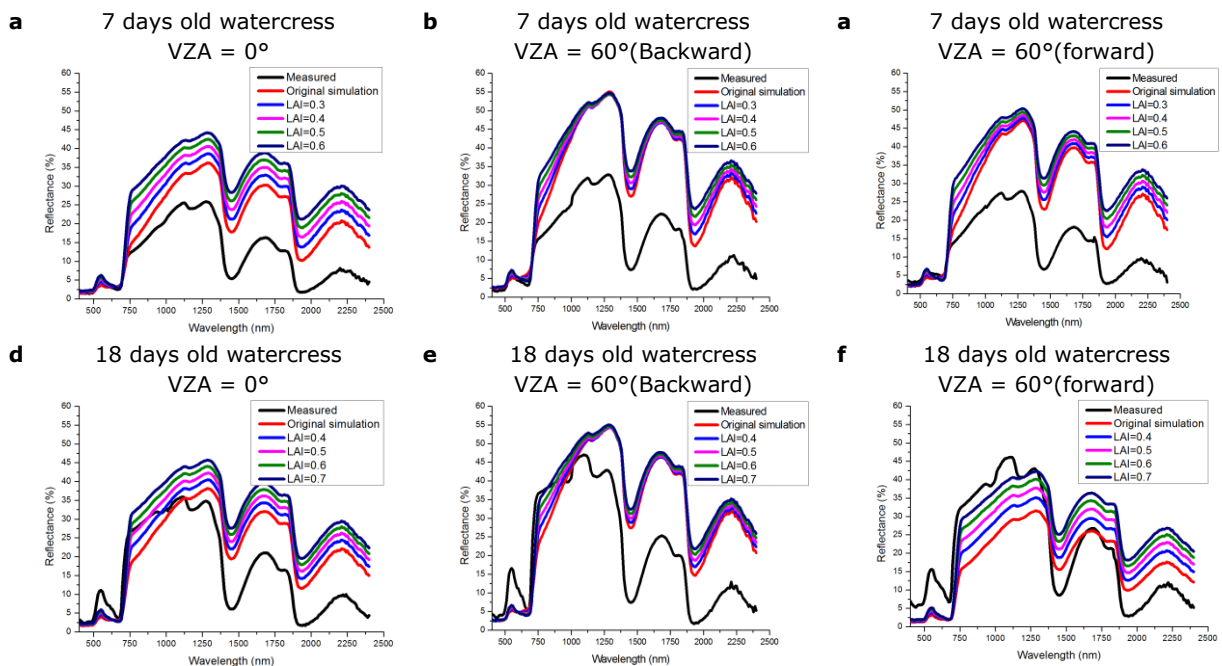


Figure 57. SLC simulations with different LAI values for watercress. For the 7 days old watercress: **a)** VZA = 0°; **b)** VZA = 60° (backward); **c)** VZA = 60° (forward) and for the 18 days old watercress: **d)** VZA = 0°; **e)** VZA = 60° (backward); **f)** VZA = 60° (forward).

The aforementioned changes in the reflectance result in changes in the RMSE, see Figure 58. The RMSE between the simulations and the measurements of the 7 days old lawn grass at all positions decreases, which could indicate that the LAI values for the original simulations were too low, see

Figure 58a. For the 7 days old watercress, all simulated positions were negatively influenced by the increasing LAI values, resulting in an increased RMSE, which could indicate that the LAI parameter in the original simulations was too high, see Figure 58b.

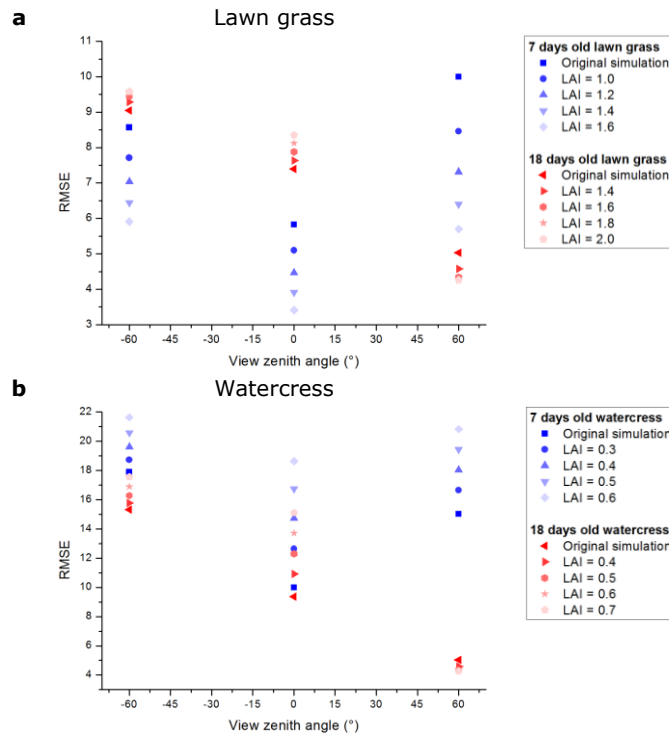
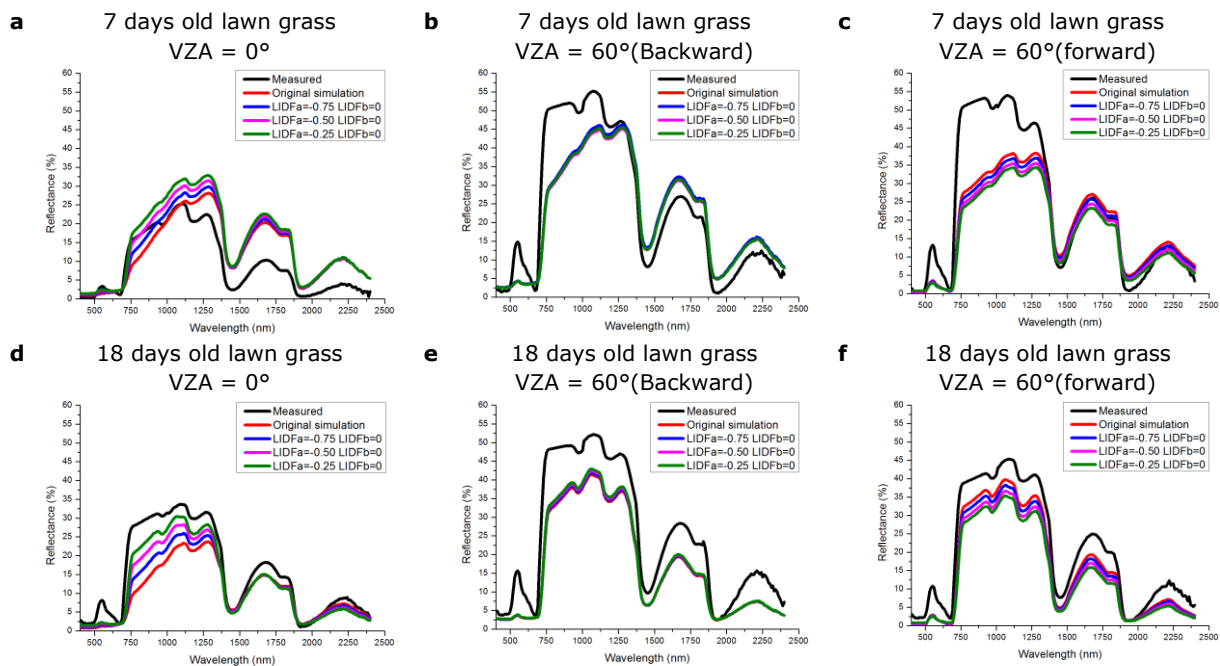


Figure 58. Changes in RMSE of lawn grass and watercress between measured and simulated reflectance after increasing the LAI parameter for **a)** 7 and 18 days old lawn grass and; **b)** 7 and 18 days old watercress.

### 4.1.2 LIDFa and LIDFb

In the original simulations, LIDFa = -1 and LIDFb = 0 were used to describe the erectophile canopy of the lawn grass and LIDFa = 1 and LIDFb = 0 to describe the planophile watercress canopy. However, these parameter settings are extreme: they describe a canopy, consisting of completely vertical leaves (erectophile) and completely horizontal leaves (planophile). The leaves of the vegetation targets actually were less extreme, see *Table 2*. The simulations were therefore repeated with less extreme parameter settings: LIDFa = -0.75 and LIDFb = 0, LIDFa = -0.50 and LIDFb = 0 and LIDFa = -0.25 and LIDFb = 0 to describe erectophile leaves and LIDFa = 0.75 and LIDFb = 0, LIDFa = 0.50 and LIDFb = 0 and LIDFa = 0.25 and LIDFb = 0 to describe planophile leaves.

Changing the LIDFa and LIDFb parameters did not result in an improvement of the simulations of the 7 days old lawn grass. At nadir position and in the forward scatter direction in the NIR, moderating the erectophile LAD seems to increase the difference between the laboratory measurements and the SLC simulations (*Figure 59a* and *Figure 59c*). For the 18 days old lawn grass, the difference between the measured and simulated reflectance decreases in the range from 800 to 1400 nm, see *Figure 59d*. However, in the forward scatter direction, from 700 to 2400 nm, with exception of the water absorption bands around 1400 nm and 1900 nm, the difference increases (*Figure 59d*).



*Figure 59. SLC simulations with different LIDFa and LIDFb values for lawn grass. For the 7 days old lawn grass: a) VZA = 0°; b) VZA = 60° (backward); c) VZA = 60° (forward) and for the 18 days old lawn grass: d) VZA = 0°; e) VZA = 60° (backward); f) VZA = 60° (forward).*

Changing values of the LIDFa and LIDFb parameters does not result in any major differences between measured and simulated reflectance, see *Figure 60*. Especially the reflectance in the backward scatter direction does not seem to be influenced by moderation of the LAD. *Figure 61* confirms the observed effects in *Figure 59* and *Figure 60*: the nadir simulation and the simulation at a VZA of -60° of the 18 days old lawn grass and the nadir simulation of the 18 days old watercress profit from moderating the LAD, resulting in a lower RMSE value. In the forward direction, both the 7 and 18

days old watercress are negatively influenced by changing the LIDFa and LIDFb parameters, resulting in higher RMSE values.

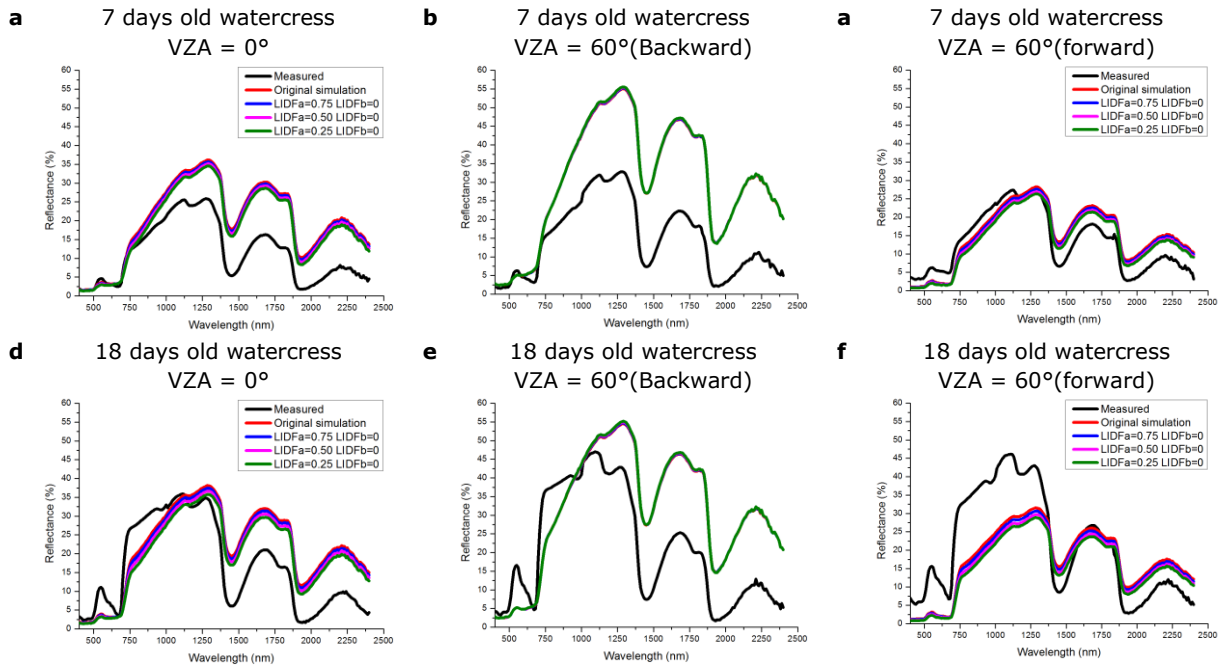


Figure 60. SLC simulations with different LIDFa and LIDFb values for watercressFor the 7 days old watercress: **a)** VZA = 0°; **b)** VZA = 60° (backward); **c)** VZA = 60° (forward) and for the 18 days old watercress: **d)** VZA = 0°; **e)** VZA = 60° (backward); **f)** VZA = 60° (forward).

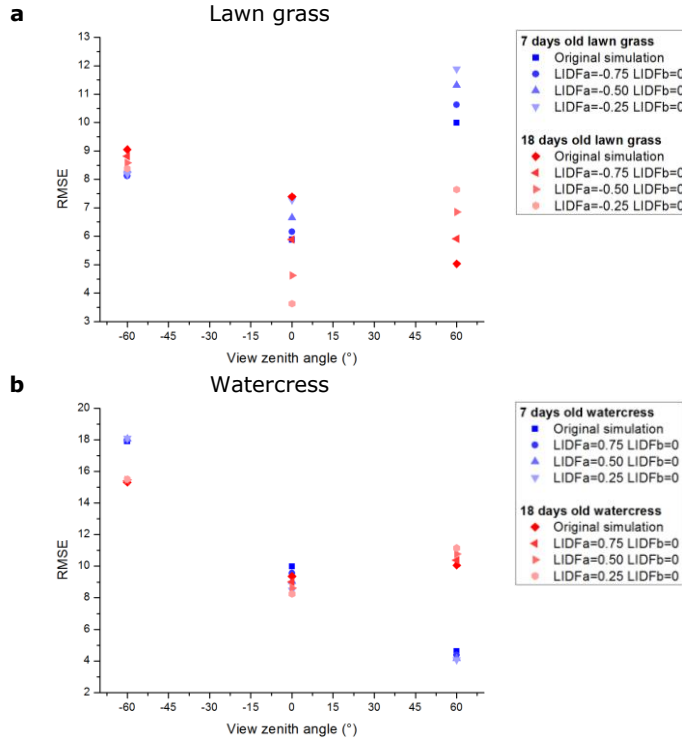


Figure 61. Changes in RMSE of lawn grass and watercress between measured and simulated reflectance after changing the LIDFa and LIDFb parameters for **a)** 7 and 18 days old lawn grass and; **b)** 7 and 18 days old watercress.

### 4.1.3 Water content

Because the vegetation samples were accidentally destroyed before the water content and dry matter content could be determined, a water content and dry matter content of 75% and 25%, respectively, were used for all vegetation targets, based upon a study of Al-Qahtani (2009). However, a higher water content is more likely to be present based on the overestimations of the 1400 nm – 2400 nm region for the lawn grass, but for the watercress in particular. Therefore additional simulations with increasing ratios water content to dry matter content have been conducted, see *Table 13*.

*Table 13. The water content in  $g/cm^2$  for increasing Cw – Cdm ratios.*

	1		2		3		4	
	Cw	Cdm	Cw	Cdm	Cw	Cdm	Cw	Cdm
	80%	20%	85%	15%	90%	10%	95%	5%
7 days old lawn grass	0.0142	0.0035	0.0150	0.0027	0.0159	0.0018	0.0168	0.0009
18 days old lawn grass	0.0323	0.0081	0.0343	0.0061	0.0364	0.0040	0.0384	0.0020
7 days old watercress	_*	_*	0.0008	0.0001	_*	_*	0.0009	0.0000
18 days old watercress	0.0016	0.0004	0.0017	0.0003	0.0018	0.0002	0.0019	0.0001

*\*Due to the low weight of the 7 days old watercress leaves, changing Cw – Cdm ratio did not result in different Cw and Cdm values.*

Increasing the water content ratio did not result in any major visual improvements for both the 7 and 18 days old lawn grass (*Figure 62*) and the 7 and 18 days old watercress (*Figure 63*), respectively. Especially in the case of the watercress, there are no observable differences with the original simulations. This is probably due to the low amount of vegetation in the watercress canopies: the combined weight of the dry matter and water content (*Table 5*) is a total weight of  $0.0009 \text{ gr/cm}^2$  and  $0.0020 \text{ gr/cm}^2$  for the 7 and 18 days old watercress, respectively. Changing the dry matter to water content ratio had no visual impact.

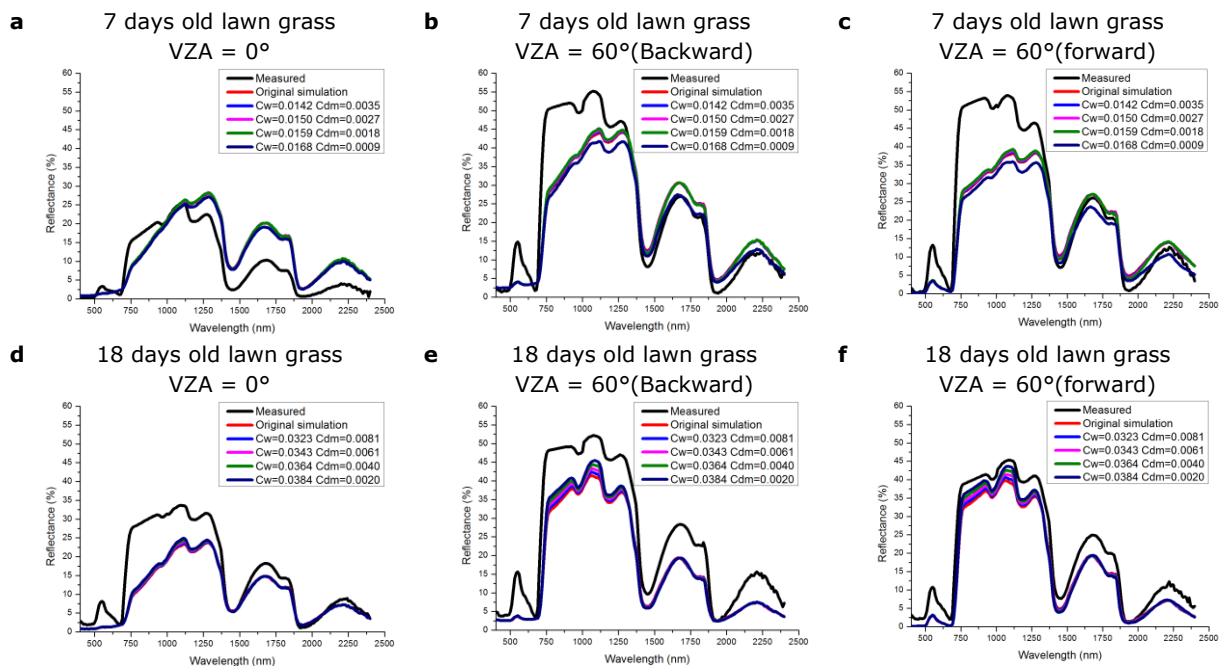


*Figure 62. SLC simulations with different Cw and Cdm values for lawn grass. For the 7 days old lawn grass: a) VZA = 0°; b) VZA = 60° (backward); c) VZA = 60° (forward) and for the 18 days old lawn grass: d) VZA = 0°; e) VZA = 60° (backward); f) VZA = 60° (forward).*

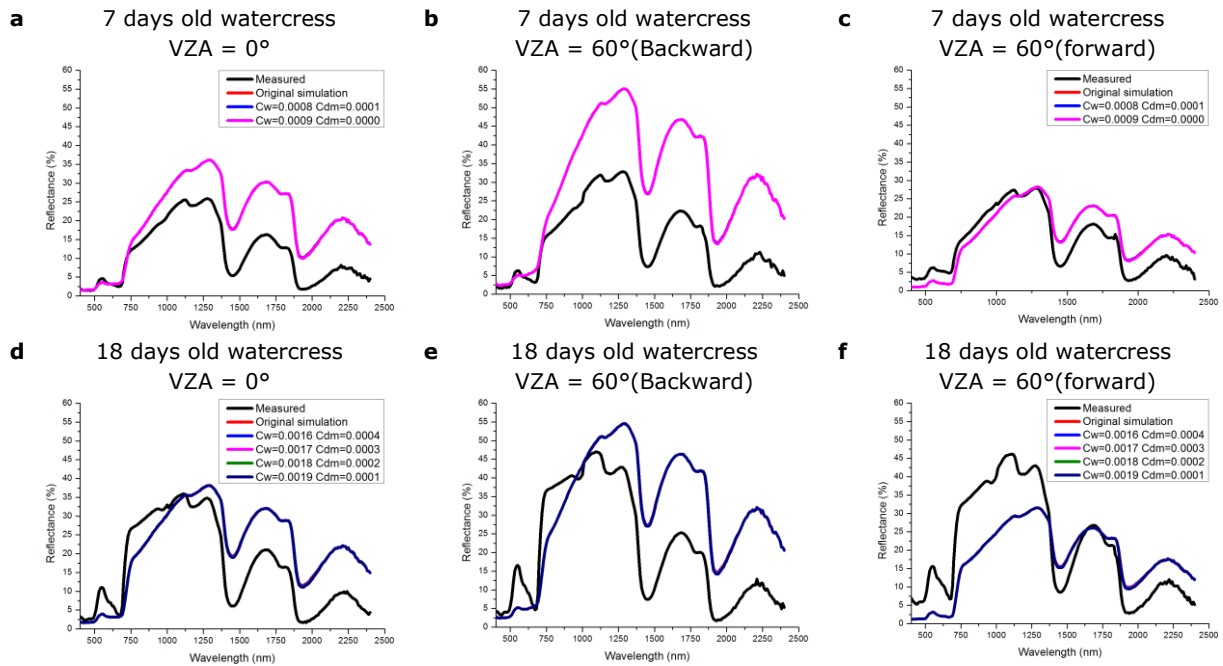


Figure 63. SLC simulations with different Cw and Cdm values for watercress. For the 7 days old watercress: **a)** VZA = 0°; **b)** VZA = 60° (backward); **c)** VZA = 60° (forward) and for the 18 days old watercress: **d)** VZA = 0°; **e)** VZA = 60° (backward); **f)** VZA = 60° (forward).

Figure 64a shows the changes in RMSE of the measurements and the simulations with different Cw to Cdm ratios. In general, for both the 7 and 18 days old lawn grass, increasing the water content resulted in a small decrease in RMSE for all simulated positions. The changes in the RMSE values for the watercress simulation are so small that they are not visible in Figure 64b.

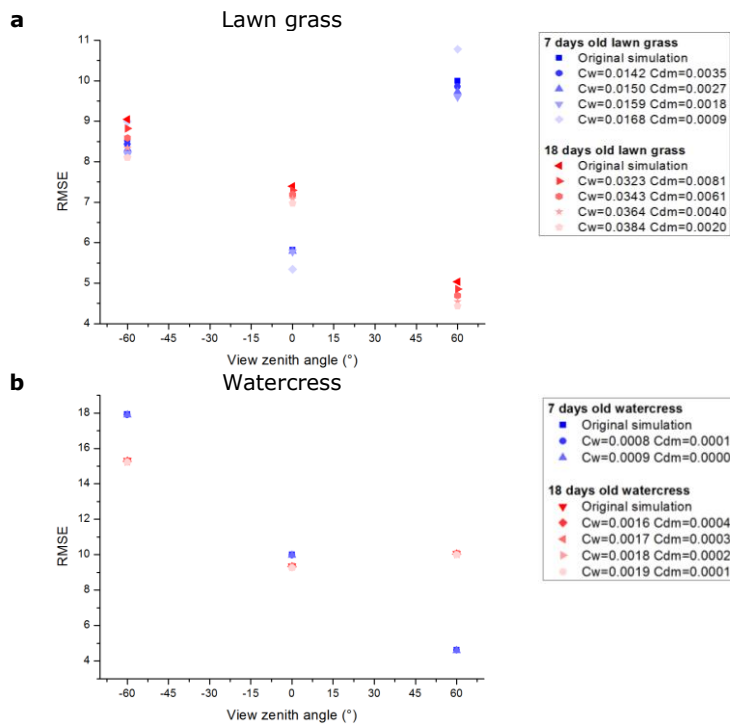


Figure 64. Changes in RMSE of lawn grass and watercress between measured and simulated reflectance after changing the dry matter to water content ratio for **a)** 7 and 18 days old lawn grass and; **b)** 7 and 18 days old watercress.

## 4.2 SLC simulations

For the simulations, it is assumed that the SLC-model is able to reproduce the spectral signatures that were measured in the laboratory, when the correct parameter settings are applied. Therefore, the parameters of the SLC-model that were used for the simulations were determined and measured as accurately as possible. However, the spectral signatures that were produced by the SLC simulations, using these parameters, differ strongly from the laboratory measurements. There are three possible explanations for this:

- 1) The parameter settings, which were applied for the simulations were incorrect. The simulations of the soil target indicate that the used parameter settings were not suitable to reproduce the soil spectra that were measured in the laboratory at off-nadir viewing angles (see the off-nadir RMSE values in *Figure 45*). This is not surprising, since the soil parameters were left at their default settings, which were derived from a ploughed soil (Pinty et al. 1989). Due to the low LAI values, it is possible that the SLC simulations of the vegetation targets were influenced by the incorrect soil parameter settings. However, the nadir simulations of the vegetation targets produced high RMSE values when compared to the laboratory measurements (*Figure 45*), which indicates an incorrect setting of the vegetation parameters. The changes in RMSE after repeating the simulations with changes of individual parameters, as displayed in *Figure 58*, *Figure 61* and *Figure 64*, indicate that changing one of the parameters and repeating the simulations does not always improve the simulated spectra. This indicates that the difference between measured and simulated reflectance was not caused by just a single incorrect parameter. However, it is possible that difference between the measured and the simulated spectra is caused by a combination of incorrect parameter settings.
- 2) In the laboratory BCRFs were measured while the SLC-model simulated BRFs. The BCRF integrates reflectance over a range of angles, resulting in a different quantity compared to a BRF. BRF measurements require a sensor with an infinitesimally IFOV and illumination from a single direction (Sandmeier 2000). Due to the absence of a collimator and the IFOV of 8° of the spectrometer, the BRF is clearly not approximated by the laboratory measurements. This could contribute to the differences in laboratory measurements and simulations.
- 3) Another explanation could be that the SLC-model is not capable of simulating laboratory measurements. This could indicate that the SLC-model or (some of) the model parameters do not have a sufficient physical basis.

Although the SLC-model was not able to exactly reproduce the spectral signatures of the multi-angular measurements of the lawn grass and watercress vegetation targets, it was able to simulate some of the anisotropic reflectance effects that were observed during the measurements. This indicates that there is some potential for the model to be used in combination with laboratory goniometer measurements. It is possible that changing multiple parameters of the SLC-model and/or adapting the set-up of the goniometer facility, in order to closer approximate BRF measurements, would result in a better match between measured and modelled reflectance factors.

### 4.3 Laboratory measurements

Most of the observed anisotropic reflectance effects during the laboratory measurements are in agreement with the physical mechanisms, as described by Kimes (1983), which are mainly responsible for the anisotropic reflectance behaviour of bare soil and vegetated surfaces. All vegetation targets show an increased reflectance in the backward scatter direction and a minimal reflectance around the nadir position or slightly in the forward direction in the principal plane as a result of the gap and backshadow effect. The obtained results are similar to the BRF measurements of lawn grass and watercress of Sandmeier et al. (1998a). However, a major difference in the results of this thesis, is that Sandmeier et al. (1998a) observed a clear hot-spot for both the lawn grass and watercress targets. It is possible that this is the result of the differences in IFOV and the sensor – target distance. The IFOV of the spectrometer that was used to perform the laboratory measurements for this thesis was set at 8° at a sensor – target distance of 40 cm, while the measurements of Sandmeier et al. (1998a) were performed with a sensor IFOV of 3° at a sensor – target distance of 200 cm. The measurements of Sandmeier et al. (1998a) are therefore a closer approximation of a BRF, compared to the measurements of the goniometer facility that were performed for this thesis. The 8° IFOV integrates the reflectance over a greater range of angles, which results in a blurred effect of the hot-spot. Increasing the sensor – target distance allows for measurements closer to the hot-spot position and decreasing the IFOV of the spectrometer would result in a better approximation of BRF measurements (Martonchik et al. 2000). Besides the sensor – target distance and the IFOV of the spectrometer, there are also some comments about the light source. The light beam of the QTH lamp that was used for the laboratory measurements was not collimated, which results in a more diffuse illumination instead of direct illumination. In order to measure BRFs, direct illumination is required. When using a collimator and applying the abovementioned settings, it is possible that a more pronounced hot-spot will be observed. Besides this, using a collimator would also result in a more homogeneous illumination of the measured target.

Another difference is the canopy cover: Sandmeier et al. (1998a) performed their measurements on fully grown canopies, which completely covered the underlying soil. The measurements for this thesis were performed on sparse canopies. Therefore, the measured BCRFs were influenced by the underlying soil, sometimes resulting in extreme ANIFs (e.g. for the 7 days old lawn grass *Figure 23a*). At nadir position a great part of the underlying soil is observed by the spectrometer, due to the low vegetation coverage of 28.52% (*Table 2*). At off-nadir viewing angles the proportion of observed vegetation, which is brighter compared to the dark soil, strongly increases. This results in a high ANIF. The inhomogeneous vegetation cover (*Figure 11*), especially of the watercress targets, results in different proportions of observed soil and vegetation at different observation angles. Theoretically, anisotropic reflectance effects are azimuthally symmetric about the principal plane (Martonchik et al. 2000); however, this is not the case in practice, as can be seen in almost all of the polar plots that are presented in this thesis. This makes it complicated to determine whether observed anisotropic reflectance effects were caused by viewing and illumination geometry, or by different proportions of soil and vegetation within the IFOV of the spectrometer at different measurement positions. Therefore, we actually cannot speak of the anisotropic reflectance behaviour of lawn grass and watercress, because most of the observed reflectance anisotropy is an effect of the vegetation targets in combination with the underlying soil.



## **5 CONCLUSIONS AND RECOMMENDATIONS**

In this chapter, first the research questions will be answered, followed by a summary with some concluding remarks. In the final section, some recommendations for further research using the goniometer facility and the SLC-model will be given.

## 5.1 Answering the research questions

*What is the effect of LAD on the anisotropic reflectance behaviour of vegetation targets as measured under controlled laboratory conditions and is the SLC-model able to simulate these effects?*

The LAD affects which part of the canopy is visible at different VZAs. Canopies with an erectophile LAD allow for the observation of the lower and less-illuminated parts of a canopy at VZAs close to nadir (the gap effect). In the forward scatter direction, the shaded backside of the canopy is observed (the backshadow effect). These two mechanisms result in a minimum reflectance observed for erectophile canopies close to nadir, slightly in the forward direction. The effects of these mechanisms are most pronounced at wavelengths with relatively high absorption (in the blue and the red). In the green, but especially in the NIR these effects diminished due to multiple scattering, which results in a decreased contrast between shadowed and illuminated parts of the canopy and therefore in less pronounced anisotropic reflectance effects. The results of the laboratory measurements of the lawn grass targets were in agreement with these effects. Some minor inconsistencies, which were most likely caused by inhomogeneity of the vegetation cover, were observed, like for example the minimum observed reflectance factor in the backward scatter direction of the 7 days old lawn grass. Although the SLC-model was not able to reproduce the measured spectral signatures, it was able to simulate some of the observed anisotropic reflectance effects. For example, the proportion of forward and backward scattering in terms of ANIF was closely simulated for the 7 days old lawn grass.

The difference between nadir and off-nadir observations is less pronounced for canopies with a planophile LAD. Planophile canopies display less pronounced anisotropic reflectance behaviour. Due to the specular reflectance component, which is caused by the horizontal orientation of planophile leaves, planophile canopies usually display a certain proportion of forward scattering. The smaller contrast between sunlit and shadowed parts of a planophile leaf results in a less-pronounced hot-spot for planophile canopies. However, due to the low vegetation cover of the planophile watercress canopies, there was a strong contribution of the underlying soil, which resulted in the observation of a hot-spot effect. A forward scattering component was observed at the measurements of the watercress targets in the laboratory; however, the forward scattering component was not simulated by the SLC model. This was probably due to the large contribution of the underlying soil to the simulations. The simulated soil did not have a forward scattering component, resulting in a decrease in ANIF in the forward scatter direction. The watercress simulations also showed a decrease in ANIF in the forward scatter direction, indicating that the reflectance anisotropy of the watercress was dominated by the reflectance anisotropy of the underlying simulated soil.

*What is the effect of the soil background on the anisotropic reflectance behaviour of vegetated surfaces as measured under controlled laboratory conditions and is the SLC-model able to simulate these effects?*

It has to be noted that the effect of LAD (research question 1) and the effect of soil background (research question 2), combined with the proportion of vegetation cover, are closely linked to each other. LAD affects not only the distribution of shadows, but it also determines the proportion of visible underlying soil at different view zenith angles and the proportion of visible soil is also related to the canopy cover.

The largest proportion of the soil is visible at nadir position and this proportion decreased at increasing off-nadir viewing angles. This was especially the case for the erectophile vegetation. Due to the bright colour of the vegetation and the dark colour of the soil background, lower reflectance factors were measured at nadir position and greater reflectance factors were measured at greater off-nadir viewing angles. For planophile vegetation, the differences between nadir and off-nadir observed proportion of the underlying soil is less pronounced. The measured reflectance factors of the planophile watercress targets were therefore smaller.

It is likely that the simulations were also affected by the underlying soil, especially the watercress targets, since these had a very low vegetation cover and LAI. The simulated anisotropic reflectance behaviour of bare soil was quite similar to the simulated reflectance anisotropy of watercress. Based on the comparison of the measurements and the simulations, it can be concluded that the used parameter settings of the soil were not able to simulate its anisotropic reflectance behaviour. This could also have contributed to the differences between measured and modelled reflectance. However, it is not possible to determine what exactly the contribution of the simulated soil was to the reflectance anisotropy of the simulated vegetation targets.

*What is the effect of changing the illumination angle on the anisotropic reflectance behaviour of vegetated surfaces as measured under controlled laboratory conditions and is the SLC-model able to simulate these effects*

Theoretically, increasing the illumination zenith angle results in a greater variation of minimum and maximum reflectance factors, especially in the visible part of the spectrum, due to a stronger difference between illuminated and shadowed parts of the observed target. In terms of ANIX, the laboratory measurements of the bare soil target and the 7 days old watercress are in agreement with this. However, the other measured targets are not. This is probably caused by the inhomogeneity of the vegetation cover of the targets, where at different observation positions different proportions of soil and vegetation were measured, resulting in inconsistent behaviour of the ANIX. In contrast to the laboratory measurements, the SLC-model simulated larger anisotropy indices at greater illumination zenith angles for all of the simulated targets, indicating the ability to simulate change in anisotropic reflectance behaviour due to changes in illumination angle.

## 5.2 Summary and conclusions

In this thesis, multi-angular reflectance measurements of several soil, lawn grass and watercress targets, performed by the laboratory goniometer facility of Wageningen University under different illumination angles, were compared to simulations by the SLC radiative transfer model. The main goal of this thesis was to investigate if the SLC-model was able to reproduce the laboratory measurements. The SLC-model simulations were performed using parameter settings, which were non-spectrally derived from the vegetation targets. Comparable results between the laboratory measurements and SLC simulations would indicate that the goniometer facility and the SLC-model form a solid base for the investigation of the effect of biophysical and biochemical vegetation parameters on anisotropic reflectance behaviour.

Since it was the first time that the goniometer facility was used to perform multi-angular reflectance measurements, it was assessed if the measurements were in agreement with (i) the physical mechanisms that are responsible for reflectance anisotropy and (ii) results of similar published measurements. The vegetation targets, which were measured by the goniometer exhibit anisotropic reflectance behaviour according to the physical mechanisms as described in previously published literature, resulting in the observation of the lowest reflectance around nadir position or slightly in the forward scatter direction and increased reflectance at increasing off-nadir viewing angles, especially in the backward scatter direction and around the hot-spot position. However, some inconsistencies with the mechanisms were found when changing the illumination zenith angle. Larger off-nadir illumination angles theoretically result in a larger variation in reflectance anisotropy. This was not found for all vegetation targets. However, this can be explained by the inhomogeneity of the canopy cover of the vegetation targets or the illumination of the un-collimated light beam. Inhomogeneity of the vegetation cover results in different proportions of vegetation and soil at that are observed by the spectrometer at different measurement positions and thus in reflectance anisotropy, which is not purely caused by the vegetation itself. Due to the absence of a collimator, the inhomogeneity of the illumination results in areas that are stronger or weaker illuminated. Both the inhomogeneity of the vegetation cover and the illumination result in unexpected anisotropic reflectance behaviour, which is not caused by the actual anisotropic reflectance behaviour of the observed target.

After normalization of the measured and simulated data, the SLC-model was in some cases able to simulate the reflectance anisotropy that was measured in the laboratory. However, the model was not able to accurately reproduce the measured spectral signatures of the different vegetation targets. A possible explanation for this is that the parameters, which were used for the simulations, were incorrect. It is shown that the difference between measured and simulated reflectance is probably not caused by individual incorrect parameters, but that it is more likely that it is caused by a combination of incorrect parameters. It could, however, also be possible the SLC-model and/or the model parameters do not have a sufficient physical basis. Another explanation for the large differences between the measured and the simulated reflectance is the difference between the measured and simulated quantities: in the laboratory, biconical reflectance factors were measured, while the SLC-model simulates bidirectional reflectance factors. The difference in measured and simulated quantity could also contribute to the difference between measured and simulated reflectance.

Based on the results of this research, it can be concluded that the laboratory goniometer facility can be used to measure reflectance anisotropy. The SLC-model is able to simulate some of the measured anisotropic reflectance effects; however, the model is not able to simulate the spectral signatures as measured in the laboratory. Therefore the SLC-model is not suitable for the investigation of anisotropic reflectance effects in combination with the set-up of the goniometer facility, as was used to perform the measurements.

### **5.3 Recommendations**

If we assume that the SLC-model has a sufficient physical basis and is able to accurately simulate reflectance anisotropy, then the differences between the laboratory measurements and the SLC-model simulations are caused by either incorrect parameter settings, the used measurement set-up or a combination of both. Recommendations for experiments for future research using the goniometer facility and the SLC-model are as follows:

The parameters that were used for the simulation of the bare soil were derived from a ploughed soil. This contributed to a proportion of the difference between measured and modelled reflectance anisotropy. Acquiring expert knowledge, possibly by the developers of the SLC-model, about the soil parameters could increase the performance of the simulations. By means of model inversion against the laboratory measurements it is also possible to retrieve more accurate soil parameters. Expert knowledge about the vegetation parameter settings might also improve the simulations.

The fact that the goniometer measures biconical reflectance factors and the SLC-model simulates bidirectional reflectance factors also results in a difference between measured and modelled reflectance. Changing the goniometer set-up might result in a better match. By increasing the measured sensor – target distance and decreasing the sensor's instantaneous field of view, a better approximation of a BRDF measurement will be obtained. Adding a collimator to the light source ensures a more direct illumination and more homogeneous illumination of the target surface. There is a high possibility that applying these settings will result in a better match between measured and modelled reflectance.

Apart from the measurement set-up, the vegetation targets also need to be selected with care. For future multi-angular measurements with the goniometer facility, where the anisotropic behaviour of vegetation needs to be measured, it is important to select targets that completely cover the surface in order to make sure that the measurements will not be influenced by the underlying soil.

Before the goniometer measurements and SLC-model simulations can be used for investigating anisotropic reflectance effects at air-borne or space-borne scales, it is important to study the effects of up-scaling the observed reflectance anisotropy. Therefore, first the effect of diffuse illumination needs to be studied, possibly in combination with measurements performed in the laboratory. This would be a great continuation of this thesis.



## REFERENCES

- Al-Qahtani, M.R.A. (2009). Effect of addition of sand and soil amendments to loam and brick grit media on the growth of two turf grass species (*Lolium perenne* and *Festuca rubra*). *Journal of Applied Sciences*, *9*, 2485-2489
- Allen, W.A., Gausman, H.W., Richardson, A.J., & Thomas, J.R. (1969). Interaction of isotropic light with a compact plant leaf. *J Opt Soc Amer*, *59*, 1376-1379
- Barducci, A., Guzzi, D., Marcoionni, P., & Pippi, I. (2009). Investigating the angular and spectral properties of natural targets using CHRIS-PROBA images of San Rossore test site. *International Journal of Remote Sensing*, *30*, 533-553
- Barnsley, M.J., Strahler, A.H., Morris, K.P., & Muller, J.P. (1994). Sampling the surface bidirectional reflectance distribution function (BRDF): 1. evaluation of current and future satellite sensors. *Remote Sensing Reviews*, *8*, 271-311
- Beisl, U. (2001). Correction of bidirectional effects in imaging spectrometer data. *University of Zürich (CH), Faculty of Sciences, Remote Sensing Series*, *37*
- Botha, E.J., Leblon, B., Zebarth, B.J., & Watmough, J. (2010). Non-destructive estimation of wheat leaf chlorophyll content from hyperspectral measurements through analytical model inversion. *International Journal of Remote Sensing*, *31*, 1679-1697
- Brown De Colstoun, E.C., & Walthall, C.L. (2006). Improving global scale land cover classifications with multi-directional POLDER data and a decision tree classifier. *Remote Sensing of Environment*, *100*, 474-485
- Bruegge, C., Chrien, N., & Haner, D. (2001). A spectralon BRF data base for MISR calibration applications. *Remote Sensing of Environment*, *77*, 354-366
- Bruinsma, J. (1963). The quantitative analysis of chlorophylls a and b in plant extracts. *Photochemistry and Photobiology*, *2*, 241-249
- Cierniewski, J., & Verbrugghe, M. (1997). Influence of soil surface roughness on soil bidirectional reflectance. *International Journal of Remote Sensing*, *18*, 1277-1288
- Combes, D., Bousquet, L., Jacquemoud, S., Sinoquet, H., Varlet-Grancher, C., & Moya, I. (2007). A new spectrogoniophotometer to measure leaf spectral and directional optical properties. *Remote Sensing of Environment*, *109*, 107-117
- Curran, P.J. (1989). Remote sensing of foliar chemistry. *Remote Sensing of Environment*, *30*, 271-278
- Dangel, S., Kneubühler, M., Kohler, R., Schaepman, M.E., Schopfer, J., Strub, G., & Itten, K.I. (2003). Combined Field and Laboratory Goniometer System - FIGOS and LAGOS. In, *Proceedings IGARSS 2003*. Toulouse: IEEE
- Dangel, S., Verstraete, M.M., Schopfer, J., Kneubühler, M., Schaepman, M., & Itten, K.I. (2005). Toward a direct comparison of field and laboratory goniometer measurements. *IEEE Transactions on Geoscience and Remote Sensing*, *43*, 2666-2675
- De Kok, L., van Hasselt, P.R., & Kuiper, J.C. (1978). Photo-oxidative Degradation of Chlorophyll-a and Unsaturated Lipids in Liposomal Dispersions at Low-Temperature. *Physiologica Plantarum*, *43*, 7-12
- Diner, D.J., Beckert, J.C., Reilly, T.H., Bruegge, C.J., Conel, J.E., Kahn, R.A., Martonchik, J.V., Ackerman, T.P., Davies, R., Gerstl, S.A.W., Gordon, H.R., Muller, J.P., Myneni, R.B., Sellers, P.J., Pinty, B., & Verstraete, M.M. (1998). Multi-angle imaging spectroradiometer (MISR) instrument description and experiment overview. *IEEE Transactions on Geoscience and Remote Sensing*, *36*, 1072-1087

- Grant, L. (1987). Diffuse and specular characteristics of leaf reflectance. *Remote Sensing of Environment*, 22, 309-322
- Hapke, B. (1981). Bidirectional Reflectance Spectroscopy 1. Theory. *J. Geophys. Res.*, 86, 3039-3054
- Hatchell, D.C. (1999). Analytical Spectral Devices, Inc. (ASD) - Technical guide third edition. In
- Heiskanen, J. (2006). Tree cover and height estimation in the Fennoscandian tundra-taiga transition zone using multiangular MISR data. *Remote Sensing of Environment*, 103, 97-114
- Huang, W., Wang, Z., Huang, L., Lamb, D.W., Ma, Z., Zhang, J., Wang, J., & Zhao, C. (2011). Estimation of vertical distribution of chlorophyll concentration by bi-directional canopy reflectance spectra in winter wheat. *Precision Agriculture*, 12, 165-178
- Jackson, R.D., Teillet, P.M., Slater, P.N., Fedosejevs, G., Jasinski, M.F., Aase, J.K., & Moran, M.S. (1990). Bidirectional measurements of surface reflectance for view angle corrections of oblique imagery. *Remote Sensing of Environment*, 32, 189-202
- Jacquemoud, S., & Baret, F. (1990). PROSPECT: A model of leaf optical properties spectra. *Remote Sensing of Environment*, 34, 75-91
- Kawa-Miszczak, L., Węgrzynowicz-Lesiak, E., Gabryszewska, E., & Saniewski, M. (2009). Effect of different sucrose and nitrogen levels in the medium on chlorophyll and anthocyanin content in *Clematis pitcheri* shoots cultured in vitro at different temperatures. *Journal of Fruit and Ornamental Plant Research*, 17, 113-121
- Kimes, D.S. (1983). Dynamics of directional reflectance factor distributions for vegetation canopies. *Applied Optics*, 22, 1364-1372
- Kneubühler, M., Koetz, B., Huber, S., Schaepman, M.E., & Zimmermann, N.E. (2008). Space-based spectrodirectional measurements for the improved estimation of ecosystem variables. *Canadian Journal of Remote Sensing*, 34, 192-205
- Kuusik, A. (1985). The hot spot effect of a uniform vegetative cover. *Soviet Journal of Remote Sensing*, 3, 645-658
- Labsphere (2012). A guide to reflectance materials and coatings. In, *Technical Guide*
- Lance, C.J., & Guy, C.L. (1992). Changes in pigment levels, Rubisco and respiratory enzyme activity of *Ficus benjamina* during acclimation to low irradiance. *Physiologia Plantarum*, 86, 630-638
- Laurent, V.C.E., Verhoef, W., Clevers, J.G.P.W., & Schaepman, M.E. (2011a). Estimating forest variables from top-of-atmosphere radiance satellite measurements using coupled radiative transfer models. *Remote Sensing of Environment*, 115, 1043-1052
- Laurent, V.C.E., Verhoef, W., Clevers, J.G.P.W., & Schaepman, M.E. (2011b). Inversion of a coupled canopy-atmosphere model using multi-angular top-of-atmosphere radiance data: A forest case study. *Remote Sensing of Environment*, 115, 2603-2612
- Lichtenthaler, H.K. (1987). [34] Chlorophylls and carotenoids: Pigments of photosynthetic biomembranes. In, *Methods in Enzymology* (pp. 350-382)
- Lillesand, T.M., Kiefer, R.W., & Chipman, J.W. (2008). *Remote sensing and image interpretation*: John Wiley & Sons
- Martonchik, J.V., Bruegge, C.J., & Strahler, A.H. (2000). A review of reflectance nomenclature used in remote sensing. *Remote Sensing Reviews*, 19, 9-20
- Mulders, M.A. (1987). *Remote sensing in soil science / M.A. Mulders*. Amsterdam ; New York : New York :: Elsevier ; Distributed in the U.S. and Canada, Elsevier Science Pub. Co
- Nicodemus, F.E., Richmond, J.C., Hsia, J.J., Ginsberg, I.W., & Limperis, T. (1977). Geometrical Considerations and Nomenclature For Reflectance. *Natl Bur Stand (US) Monogr*, 1-52

- OriginLab (2007). *Origin 8 user guide*. Northampton
- Painter, T.H., Paden, B., & Dozier, J. (2003). Automated spectro-goniometer: A spherical robot for the field measurement of the directional reflectance of snow. *Review of Scientific Instruments*, 74, 5179-5188
- Pepper, G.E., Pearce, R.B., & Mock, J.J. (1977). Leaf Orientation and Yield of Maize. *Crop Sci.*, 17, 883-886
- Pinty, B., Verstraete, M.M., & Dickinson, R.E. (1989). A physical model for predicting bidirectional reflectances over bare soil. *Remote Sensing of Environment*, 27, 273-288
- Roberts, G. (2001). A review of the application of BRDF models to infer land cover parameters at regional and global scales. *Progress in Physical Geography*, 25, 483-511
- Roosjen, P., Clevers, J., Bartholomeus, H., Schaepman, M., Schaepman-Strub, G., Jalink, H., van der Schoor, R., & de Jong, A. (2012). A Laboratory Goniometer System for Measuring Reflectance and Emittance Anisotropy. *Sensors*, 12, 17358-17371
- Roujean, J.-L., Leroy, M., & Deschamps, P.-Y. (1992). A Bidirectional Reflectance Model of the Earth's Surface for the Correction of Remote Sensing Data. *J. Geophys. Res.*, 97, 20455-20468
- Sandmeier, S., Müller, C., Hosgood, B., & Andreoli, G. (1998a). Physical mechanisms in hyperspectral BRDF data of grass and watercress. *Remote Sensing of Environment*, 66, 222-233
- Sandmeier, S., Müller, C., Hosgood, B., & Andreoli, G. (1998b). Sensitivity analysis and quality assessment of laboratory BRDF data. *Remote Sensing of Environment*, 64, 176-191
- Sandmeier, S.R. (2000). Acquisition of bidirectional reflectance factor data with field goniometers. *Remote Sensing of Environment*, 73, 257-269
- Sandmeier, S.R., & Itten, K.I. (1999). A field goniometer system (FIGOS) for acquisition of hyperspectral BRDF data. *Geoscience and Remote Sensing, IEEE Transactions on*, 37, 978-986
- Sandmeier, S.R., & Strahler, A.H. (2000). BRDF laboratory measurements. *Remote Sensing Reviews*, 18, 481-502
- Schaepman-Strub, G., Schaepman, M.E., Painter, T.H., Dangel, S., & Martonchik, J.V. (2006). Reflectance quantities in optical remote sensing-definitions and case studies. *Remote Sensing of Environment*, 103, 27-42
- Schaepman, M.E., Koetz, B., Schaepman-Strub, G., & Itten, K.I. (2005). Spectrodirectional remote sensing for the improved estimation of biophysical and -chemical variables: Two case studies. *International Journal of Applied Earth Observation and Geoinformation*, 6, 271-282
- Schopfer, J., Dangel, S., Kneubühler, M., & Itten, K.I. (2008). The improved dual-view field goniometer system FIGOS. *Sensors*, 8, 5120-5140
- Schopfer, J., Huber, S., Odermatt, D., Schneider, T., Dorigo, W., Oppelt, N., Koetz, B., Kneubuehler, M., & Itten, K.I. (2007). Towards a comparison of spaceborne and ground-based spectrodirectional reflectance data. In, *European Space Agency, (Special Publication) ESA SP*
- Seelig, H.D., Hoehn, A., Stodieck, L.S., Klaus, D.M., Adams Iii, W.W., & Emery, W.J. (2008). Relations of remote sensing leaf water indices to leaf water thickness in cowpea, bean, and sugarbeet plants. *Remote Sensing of Environment*, 112, 445-455
- Strub, G., Beisl, U., Schaepman, M., Schlaepfer, D., Dickerhof, C., & Itten, K. (2002). Evaluation of diurnal hyperspectral HDRF data acquired with the RSL field goniometer during the DAISEX'99 campaign. *ISPRS Journal of Photogrammetry and Remote Sensing*, 57, 184-193

- Verhoef, W. (1984). Light scattering by leaf layers with application to canopy reflectance modeling: The SAIL model. *Remote Sensing of Environment*, *16*, 125-141
- Verhoef, W. (1985). Earth observation modeling based on layer scattering matrices. *Remote Sensing of Environment*, *17*, 165-178
- Verhoef, W. (1998). Theory of radiative transfer models applied in optical remote sensing of vegetation canopies. In. [S.l.: s.n.]
- Verhoef, W., & Bach, H. (2003). Simulation of hyperspectral and directional radiance images using coupled biophysical and atmospheric radiative transfer models. *Remote Sensing of Environment*, *87*, 23-41
- Verhoef, W., & Bach, H. (2007). Coupled soil-leaf-canopy and atmosphere radiative transfer modeling to simulate hyperspectral multi-angular surface reflectance and TOA radiance data. *Remote Sensing of Environment*, *109*, 166-182
- Verhoef, W., & Bach, H. (2012). Simulation of Sentinel-3 images by four-stream surface-atmosphere radiative transfer modeling in the optical and thermal domains. *Remote Sensing of Environment*, *120*, 197-207
- Verrelst, J., Schaepman, M.E., Koetz, B., & Kneubühler, M. (2008). Angular sensitivity analysis of vegetation indices derived from CHRIS/PROBA data. *Remote Sensing of Environment*, *112*, 2341-2353
- Vuolo, F., Dini, L., & D'Urso, G. (2008). Retrieval of leaf area index from CHRIS/PROBA data: An analysis of the directional and spectral information content. *International Journal of Remote Sensing*, *29*, 5063-5072
- Wang, Z., Coburn, C.A., Ren, X., & Teillet, P.M. (2012). Effect of soil surface roughness and scene components on soil surface bidirectional reflectance factor. *Canadian Journal of Soil Science*, *92*, 297-313
- Watson, D.J. (1947). Comparative physiological studies on the growth of field crops: I. Variation in net assimilation rate and leaf area between species and varieties, and within and between years. *Annals of Botany*, *11*, 41-76
- Yin, Y., & Ashihara, H. (2009). Phosphate levels and expression of phosphoribosylpyrophosphate synthetase isozymes in suspension-cultured *Arabidopsis thaliana* cells. *Phytochemistry Letters*, *2*, 126-129

---

